FRACTIONALIZATION AND CONFINEMENT IN FRUSTRATED MAGNETS

by

Yuan Wan

A dissertation submitted to The Johns Hopkins University in conformity with the requirements for the degree of Doctor of Philosophy.

Baltimore, Maryland

August, 2014

Abstract

We study the fractionalization and confinement of excitations in two frustrated magnets: $S = 1/2$ kagome Heisenberg antiferromagnet and quantum spin ice. In kagome Heisenberg antiferromagnet, the ground state is a spin liquid that hosts fractional spin excitations known as spinons. We construct a phenomenological theory for the spin liquid state. Our theory explains many characteristic features observed in numerical studies, whereby providing a missing link between theory and numerics. In quantum spin ice, when spinons are confined by an external magnetic field, elementary excitations are strings connecting pairs of spinons. We show that these strings possess quantum dynamics that can be described by an emergent quantum string theory. The vibrational modes of strings are manifested as multiple resonances in dynamical structure factor, which could be observed in experiments.

Primary Reader: Professor Oleg Tchernyshyov, the Johns Hopkins University

Secondary Reader: Professor Predrag Nikolić, George Mason University

Acknowledgments

First of all, I would like to express my deepest gratitude to my advisor Professor Oleg Tchernyshyov. His devotion to students, his striving for the beauty and wonder of physics, and his elegant research style never cease to inspire me.

Second, I would like to thank my parents for their constant support and boundless love, without which it is unthinkable to finish my PhD study. Their understanding and encouragement gave me strength to pursue my academic career.

Third, I would like to thank Professor Predrag Nikolić for the careful reading my thesis and many helpful comments. I would also like to thank Professor Collin Broholm, Professor Gabor Domokos, Professor Kirill Melnikov, and the late Professor Zlato Tešanović for teaching me physics.

Finally, I would like to thank fellow students Mr. Anirban Ghosh, Mr. Arpit Gupta, Dr. Sekwon Kim, Dr. James Murray, and Dr. Olga Petrova for numerous delightful discussions. I also thank Ms. Carmelita King and Ms. Kelley Key for assisting me with their administrative and organizational skills.

Contents

List of Figures

Chapter 1

Introduction

1.1 Frustrated magnets

The study of magnetism is a science both old and young. Ancient peoples were aware of lodestone (Fe_3O_4) and its fascinating properties. The earliest known speculative theory of magnetism was recorded by Lucretius in the 1st century BC [1], yet the origin of magnetism was not explained until the birth of quantum mechanics in the early 20th century. Today, it is understood that magnetism comes from the magnetic moments of electrons. In a ferromagnet, the exchange interaction between nearby electrons forces their magnetic moments to align and result in macroscopic magnetization.

A family of magnetic materials known as frustrated magnets present new challenge and opportunity for solid state physics [2–4]. Frustrated magnets do not possess

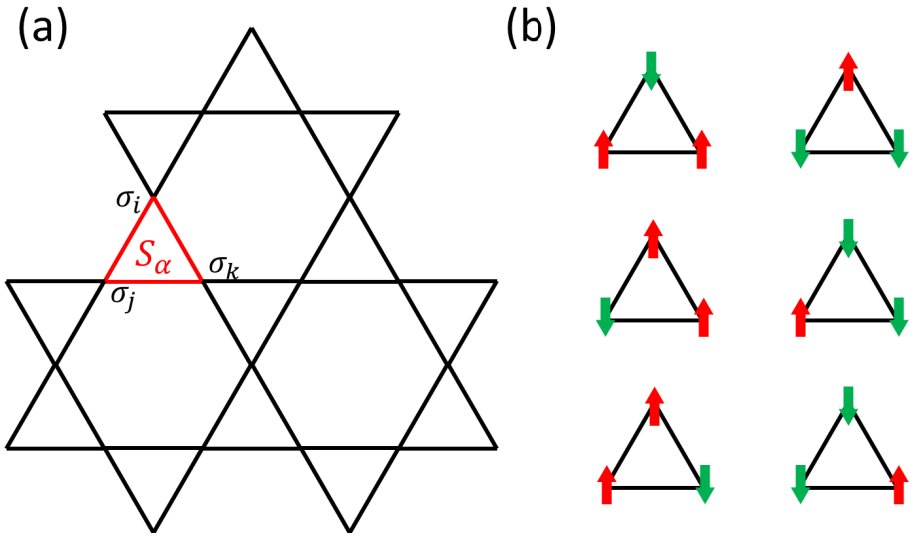

Figure 1.1: (a) Kagome is a corner-sharing network of triangles. (b) Degenerate states that minimize the local interaction energy.

macroscopic magnetization due to conflicting exchange interactions among spins, and they can show striking properties that defy analysis based on the conventional theory.

The common features of frustrated magnets can be illustrated by a concrete model, the kagome Ising antiferromagnet, introduced by Itiro Syozi in 1951 [5]. The electron magnetic moments are modeled as spins. Spins form a network of corner-sharing triangles, and each spin can point up or down (Fig. 1.1a). Neighboring spins are coupled by antiferromagnetic exchange interaction. The Hamiltonian is given by

$$H = J \sum_{\langle ij \rangle} \sigma_i \sigma_j, \tag{1.1}$$

where $\sigma_i = 1(-1)$ stands for the up (down) state, and the summation is over all links ij in the lattice. $J > 0$ is the exchange coupling constant. The Hamiltonian is quadratic in spin variables, and we can rewrite the Hamiltonian by completing the

square,

$$H = \frac{J}{2} \sum_{\alpha} S_{\alpha}^2 + \text{const.} \tag{1.2}$$

Here the summation is over the triangles α in the lattice, and S_α is the net spin of the triangle. Specifically, $S_\alpha = \sigma_i + \sigma_j + \sigma_k$, and i, j, and k are the three spins belong to α, as shown in Fig. 1.1a. S_α takes four possible values, ± 1 and ± 3.

From Eq. 1.2, we see that the ground states are attained by minimizing $|S_\alpha|$. In the ground states,

$$S_\alpha = \pm 1, \quad \forall \alpha. \tag{1.3}$$

Constraint Eq. 1.3 does not fix a unique ground state. To count the degeneracy, we note that the constraint selects 6 spin states out of 8 per each triangle, as shown in Fig. 1.1b. The total number of spin states is 2^N, where N is the number of spins. Thus, the number of ground states is approximately

$$\Omega \approx \left(\frac{6}{8}\right)^{N_\triangle} 2^N = \left(\frac{3}{4}\right)^{2N/3} 2^N = 1.651^N. \tag{1.4}$$

Here $N_\triangle = 2N/3$ is the number of triangles. The entropy at zero temperature is then given by

$$S = k_B \ln \Omega \approx 0.5013 k_B N. \tag{1.5}$$

The exact enumeration gives $S = 0.5018 k_B N$ [6]. The entropy at zero temperature grows linearly with the system size.

The existence of an enormously degenerate ground state manifold is a common trait of frustrated magnets, and it has important consequences for their properties [4]. There are two possible scenarios. On the one hand, the system could be stuck inside a small region of the manifold. On the other hand, the system could wander around this manifold due to thermal or quantum fluctuations and never settle on any state, thereby remaining paramagnetic down to zero temperature. Such magnets, preserving all the symmetries of the system and possessing non-local correlations, are known as spin liquids [3]. Kagome Ising antiferromagnet fits into the second scenario, and it is one of the earliest known examples of spin liquid.

1.2 Fractionalization and confinement

Excitations in frustrated magnets are distinct from those of conventional magnets. In a Heisenberg ferromagnet, the spins are aligned in the same direction in the ground state. The elementary excitations are magnons, which are quantized spin waves [7]. Magnons carry $S^z = -1$ spin angular momentum. In a frustrated magnet, a magnon could break up, or fractionalize, into a pair of excitations, each carrying a $S = 1/2$ spin. These fractional excitations are known as spinons, and they could show bosonic, fermionic, or even anyonic statistics [3].

In some frustrated magnets, spinons are not completely free. When a pair of spinons are separated, they leave behind a string of excitations, and the energy cost

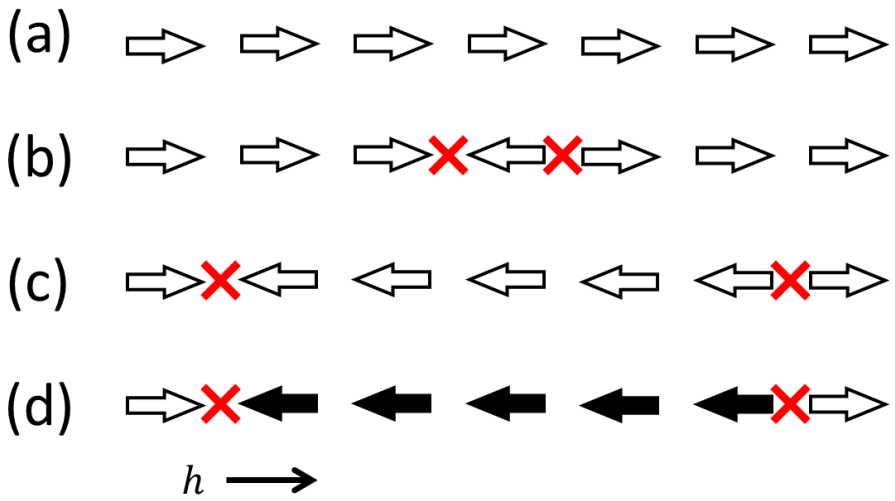

Figure 1.2: Ferromagnetic Ising chain. Flipping one spin from the ground state (a) creates a pair of domain walls (b), and the domain wall pair can be separated without additional energy cost (c). When magnetic field is present, separating domain walls costs Zeeman energy proportional to the domain wall distance (d).

grows linearly with the length of the string. The spinons are thus confined by a linear potential.

The phenomena of fractionalization and confinement can be demonstrated by a toy model: the ferromagnetic Ising chain. Strictly speaking, the ferromagnetic Ising chain is not frustrated, but it does show properties reminiscent of a frustrated magnet. In this model, the spins in the chain can point to the left or right, and there is ferromagnetic interaction between two neighboring spins. The Hamiltonian can be written as,

$$H = -J \sum_i \sigma_i \sigma_{i+1}. \tag{1.6}$$

Here σ_i is the spin at site i, and $\sigma_i = 1(-1)$ if the spin points to the right (left). $J > 0$ is the ferromagnetic exchange constant.

In the ground states, all the spins point to the same direction thanks to the ferromagnetic exchange interaction. The ground state is two-fold degenerate: $\sigma_i = 1\,\forall i$, or $\sigma_i = -1\,\forall i$. Without loss of generality, we consider the ground state in which all the spins point to the right (Fig. 1.2a). To create a magnon, we flip one spin from the right state to the left. As a result, we create two domain walls (Fig. 1.2b), and we can separate them arbitrarily far away from each other without any additional energy cost (Fig. 1.2c). Thus, the magnon is fractionalized into a pair of domain walls, which can propagate independently in the chain.

We can break the ground state degeneracy by turning on a weak magnetic field that points to the right. The Hamiltonian is given by,

$$H = -J \sum_i \sigma_i \sigma_{i+1} - h \sum_i \sigma_i. \tag{1.7}$$

The second term is the Zeeman coupling between spins and the field, and $h > 0$. The ground state in now unique, $\sigma_i = 1\,\forall i$. Again, we can create a pair of domain walls by flipping one spin. To separate the two domain walls, we must flip a string of successive spins, and each flipped spin now costs energy $2h$ (Fig. 1.2d). The domain walls are therefore confined by linear potential. It is now natural to regard the string of flipped spins as the elementary excitation, and the domain walls are the end points of the string.

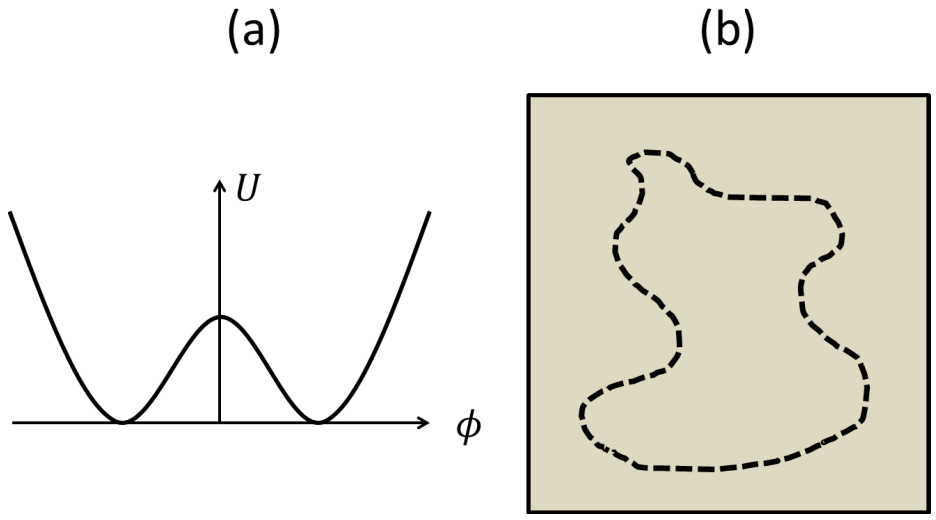

Figure 1.3: (a) Spontaneous symmetry breaking in a ferromagnet. The energy U is a symmetric function of magnetization ϕ, whereas the ground states break the time-reversal symmetry $\phi \to -\phi$. (b) In frustrated magnets, the local constraints carve a hyper-surface (shown as the dashed-curve) from the full Hilbert space (shown as the gray box).

1.3 Emergent gauge symmetries

Global symmetries play an important role in the study of conventional magnets. Magnetic ordering in conventional magnets falls into the category of spontaneous symmetry breaking. In a ferromagnet, magnetization ϕ transforms as $\phi \to -\phi$ under time-reversal operation. The Hamiltonian is invariant under time-reversal, and therefore the energy U as a function of magnetization is also symmetric, $U(\phi) = U(-\phi)$. However, $U(\phi)$ has two degenerate minima at $\pm\phi_0$. The magnet must enter one of two minima at zero temperature, thereby breaking the time-reversal symmetry.

We argue that gauge symmetries, rather than global symmetries, are essential for understanding frustrated magnets. In Section 1.1, we have seen that the enormously

degenerate manifold is crucial for the physics of frustrated magnet. The exchange interaction constrains the local spin configurations, and these local constraints carve the manifold of low energy states from the Hilbert space (Fig. 1.3b). The low-energy, long-time dynamics of the frustrated magnets is restricted to this manifold, and therefore the effective Hamiltonian for frustrated magnets must respect the local constraints.

The above considerations fit naturally into the framework of gauge theory. In particular, the local constraints can be thought of as local conservation laws resulting from emergent gauge symmetries. The fluctuations in the low-energy manifold can be interpreted as fluctuations of the gauge field. Spinon excitations carry gauge charge, and they could be free or confined depending on the details of the gauge theory. In short, gauge symmetries emerge at low energy, and the low energy effective theory of frustrated magnets must be a gauge theory.

1.4 Scope and organization

The rest of the thesis is organized as follows. In Chapter 2, we give a self-contained exposition of lattice gauge theory. Equipped with the tools from gauge theory, we are ready to study two frustrated magnets: the kagome Heisenberg antiferromagnet in Chapter 3, and the quantum spin ice in Chapter 4. We will show that both systems exhibits fractionalization and confinement. We will also connect these theoretical results to numerical studies and experiments.

Chapter 2

Lattice gauge theory

In Chapter 1, we have argued that lattice gauge theory provides a natural framework for studying frustrated magnets. In this chapter, we give an exposition of lattice gauge theory by presenting two examples, compact quantum electrodynamics (compact QED) and Ising gauge theory (IGT) with the emphasis on the lattter. As we proceed, we review concepts and techniques that will be used in the successive chapters. We shall follow the standard references [8–10] in our exposition.

The current chapter is organized as follows. We briefly review classical electrodynamics in Section 2.1 and describe compact QED in Section 2.2. Then, in Section 2.3, we motivate IGT by drawing a close analogy to compact QED. We analyze the weak-coupling phase of IGT in Sections 2.4 and 2.5 and the strong-coupling phase in 2.6. Finally, we discuss duality transformation in Section 2.7.

2.1 Classical electrodynamics

We start off by giving a quick review of the Hamiltonian formulation of classical electrodynamics. For the sake of simplicity, we focus on 2-dimensional free space. The Lagrangian density of electrodynamic field is given by,

$$\mathcal{L}_{\mathrm{EM}} = -\frac{1}{4} F^{\mu\nu} F_{\mu\nu}. \tag{2.1}$$

Here we have adopted the natural units $\mu_0 = \epsilon_0 = c = 1$. μ, ν runs from 0 to 2, and the summation over repeated indices is implied. The signature of metric is $(1, -1, -1)$. $F^{\mu\nu} = \partial^\mu A^\nu - \partial^\nu A^\mu$ is the field tensor, and A^μ is the gauge potential.

To turn the above into Hamiltonian formulation, we first fix the gauge by setting the temporal component of the gauge potential to zero,

$$A^0 = 0. \tag{2.2}$$

The above gauge condition is known as the temporal gauge. The contra-variant components of the electric field are then given by

$$E_i = \partial_0 A^i, \quad i = 1, 2. \tag{2.3}$$

The Lagrangian density is then simplified in the temporal gauge,

$$\mathcal{L} = \frac{1}{2}[(\dot{A}^1)^2 + (\dot{A}^2)^2 - B^2]. \tag{2.4}$$

Here the dot stands for time derivative, and $B = \partial_1 A^2 - \partial_2 A^1$ is the magnetic field.

We recognize $A^{1,2}$ as canonical coordinates. The canonical momenta are then determined,

$$\pi_i = \frac{\partial \mathcal{L}}{\partial(\dot{A}^i)} = \dot{A}^i = E_i, \quad i = 1, 2 \tag{2.5}$$

Therefore, the electric field is the canonical momentum conjugate to the gauge potential,

$$\{A^i(x), E_j(y)\}_P = \delta^i_j \delta^2(x - y), \tag{2.6}$$

where $\{\cdots\}_P$ is the Poisson bracket. The Hamiltonian density for classical electrodynamics is then given by,

$$\mathcal{H}_{\text{EM}} = \frac{1}{2} \sum_{i=1,2} ((E_i)^2 + (B^i)^2). \tag{2.7}$$

Even though we have eliminated the temporal component of gauge potential in Eq. 2.2, there is still gauge redundancy,

$$A^i(x) \to A^i(x) + \partial_i \phi(x), \tag{2.8}$$

where ϕ is a time-independent scalar field.

The electric charge density is defined as

$$\rho(x) = \partial_i E^i(x), \tag{2.9}$$

which is simply the Gauss law. It can be shown that the charge density at any spatial point x is a conserved quantity,

$$\{\rho(x), \mathcal{H}_{\text{EM}}\}_P = 0. \tag{2.10}$$

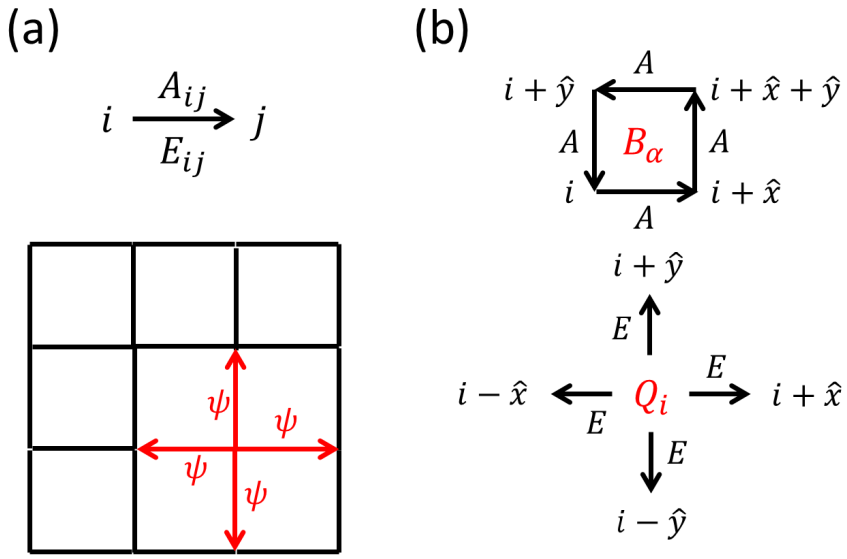

Figure 2.1: (a) The basic degrees of freedom in compact QED are the electric field E_{ij} and gauge potential A_{ij} defined on links. The elementary gauge transformation $G_i(\psi)$ on site i maps $A_{ij} \to A_{ij} + \psi$ on the four red links emanating from i. (b) Magnetic field B_α is defined as the contour sum of A_{ij} around the plaquette α, and charge Q_i is defined as the sum of E_{ij} on the four links pointing out from i.

The above is derived directly from Eq. 2.6. It is a manifestation of charge conservation. The Hamiltonian Eq. 2.7 describes only the propagation of electromagnetic wave, and the electric charges are static objects. As charge is conserved and it cannot move, the charge density $\rho(x)$ is constant in time.

2.2 Compact QED

After reviewing the essentials of classical electrodynamics, we are ready to discuss the compact quantum electrodynamics (compact QED). The compact QED is the quantization of the classical theory. It is defined on a discrete lattice instead of

continuous space. In what follows, we will consider the square lattice.

Similar to the classical theory, the basic degrees of freedom are electric field operators E_{ij} and gauge potential operator A_{ij} defined on the link ij (Fig. 2.1a). We adopt the temporal gauge to eliminate the temporal component of gauge potential. As the electric field and gauge potential are vector fields, we define $E_{ij} = -E_{ji}$ and $A_{ij} = -A_{ji}$.

The gauge potential and electric field operators form a canonical conjugate pair,

$$[A_{ij}, E_{kl}] = i(\delta_{ik}\delta_{jl} - \delta_{il}\delta_{jk}),\ [A_{ij}, A_{kl}] = [E_{ij}, E_{kl}] = 0. \tag{2.11}$$

Here the right hand side of the first commutation relation ensures that the commutator of A_{ij} and E_{ij} is i if ij and kl are the same link and have the same orientation.

In classical electrodynamics, the gauge potential takes value in $(-\infty, \infty)$. Here we reduce the range of A_{ij} by requiring that A_{ij} and $A_{ij} + 2\pi$ are the same state. In other words, $A_{ij} \in [0, 2\pi)$. Consequently, the eigenvalues of the electric field operator E_{ij} takes only integer values. This is reminiscent of the angular variable θ and the angular momentum L_θ for a planar rotor. Similar to the planar rotor, $\exp(\pm iA_{jk})$ are ladder operators that raise or lower the eigenvalue of E_{jk} by 1,

$$[e^{\pm iA_{jk}}, E_{jk}] = \mp e^{\pm iA_{jk}}. \tag{2.12}$$

The operator $\exp(iA_{ij})$ is known as link variable.

On square lattice, the magnetic field operator B_α associated with each basic pla-

quette α is,

$$B_\alpha = A_{i,i+\hat{x}} + A_{i+\hat{x},i+\hat{x}+\hat{y}} - A_{i+\hat{y},i+\hat{x}+\hat{y}} - A_{i,i+\hat{y}}. \tag{2.13a}$$

Here i, $i+\hat{x}$, $i+\hat{y}$, and $i+\hat{x}+\hat{y}$ are four corners of the plaquette α, as shown in Fig. 2.1b. The right hand side of the above definition is the lattice analog of curl. Similar to the gauge potential, B_α and $B_\alpha + 2\pi$ are identical. The magnetic flux operator F_α is related to the link variables by,

$$F_\alpha = e^{iB_\alpha} = e^{iA_{i,i+\hat{x}}} e^{iA_{i+\hat{x},i+\hat{x}+\hat{y}}} e^{-iA_{i+\hat{x},i+\hat{x}+\hat{y}}} e^{-iA_{i,i+\hat{y}}}, \tag{2.13b}$$

which is the contour product of link variables around the plaquette α.

The Hamiltonian of the classical electrodynamics Eq. 2.7 is a quadratic in terms of electric and magnetic fields. Likewise, the quantum Hamiltonian contains the electric energy,

$$\frac{1}{2}\sum_{\langle ij\rangle} E_{ij}^2, \tag{2.14a}$$

where the summation is over all links. However, we cannot use B_α^2 as the magnetic energy as we must respect the 2π periodicity of B_α. Instead, we choose,

$$\sum_\alpha [1 - \cos(B_\alpha)], \tag{2.14b}$$

whose leading term in the Taylor series at $B_\alpha = 0$ is quadratic. Here the summation is over all plaquettes. Putting all the pieces together, we obtain the Hamiltonian for compact QED on square lattice,

$$H = \frac{1}{2}\sum_{\langle ij\rangle} E_{ij}^2 + g\sum_\alpha (1 - \cos(B_\alpha)). \tag{2.14c}$$

Here g is a dimensionless constant. Hamiltonian Eq. 2.14c is the main result of this section.

The Hamiltonian Eq. 2.14c possesses gauge redundancy. The lattice analog of the gauge transformation Eq. 2.8 is given by

$$A_{ij} \to A_{ij} + \phi_i - \phi_j, \quad e^{iA_{ij}} \to e^{i\phi_i} e^{iA_{ij}} e^{-i\phi_j}. \tag{2.15}$$

Here $\phi_i \in [0,\, 2\pi)$ are arbitrary phases defined on lattice sites.

The physical meaning of the above gauge transformation is to redefine the local quantum phases on lattice sites. It can be performed successively, one site a time. In other words, the gauge transformation is composed of elementary gauge transformations, which refines the quantum phase on only one lattice site. The elementary gauge transformation on site i, denoted by $G_i(\psi)$, is defined by setting $\phi_i = \psi$, and $\phi = 0$ on other sites. Its action on gauge potential is given by

$$G_i(\psi) :\, A_{ij} \to A_{ij} + \psi, \tag{2.16}$$

where ij stand for the four links emanating from site i, as shown in Fig. 2.1b. The gauge potential on other links transform trivially under $G_i(\psi)$. It can be seen that $G_i(\psi)$ form a group with the composition rule $G_i(\psi_1)G_i(\psi_2) = G_i(\psi_1 + \psi_2)$. In addition, $G_i(\psi) = G_i(\psi + 2\pi)$. This group is known as the gauge group of compact QED, which is isomorphic to the group of unimodular complex numbers, $U(1)$.

The charge operator is defined by

$$Q_i = \sum_j E_{ij} = E_{i,i+\hat{x}} + E_{i,i+\hat{y}} + E_{i,i-\hat{x}} + E_{i,i-\hat{y}}, \tag{2.17}$$

which is the Gauss law on lattice (Fig. 2.1b). Note that charge are quantized to integer values as electric field E is quantized to integers. The elementary gauge transformation $G_i(\psi)$ is generated by charge operator,

$$e^{i\psi Q_i} A_{ij} e^{-i\psi Q_i} = A_{ij} + \psi, \tag{2.18}$$

and its action on other gauge potential operators are trivial. Therefore, $G_i(\psi) = \exp(i\psi Q_i)$. Since the Hamiltonian is invariant under $G_i(\psi)$, its generator must be good quantum number,

$$[Q_i, H] = 0 \quad \forall i. \tag{2.19}$$

The above is the analog of Eq. 2.10 and has the same physical meaning. It is simply the manifestation of charge conservation. It can also be derived directly from commutation relations Eq. 2.11.

2.3 Ising gauge theory

In this section, we present the Ising gauge theory (IGT) on sqaure lattice.

We start with the definition of electric field operators. In compact QED, $\mathcal{E}_{ij}$, the eigenvalues of electric field operator E_{ij}, take integer values. In IGT, we distinguish only the parity of $\mathcal{E}_{ij}$ and regard $|\mathcal{E}_{ij}\rangle$ and $|\mathcal{E}_{ij}+2\rangle$ as the same state. Therefore, it is sufficient to use Pauli matrix σ^x_{ij} as the electric field operator on link ij, and its eigenvalues 1 and -1 correspond to the parity $(-1)^{\mathcal{E}_{ij}}$. Since $(-)^{\mathcal{E}_{ij}} = (-1)^{-\mathcal{E}_{ij}}$, we define $\sigma^x_{ij} = \sigma^x_{ji}$, and there is no need to specify the orientation of links.

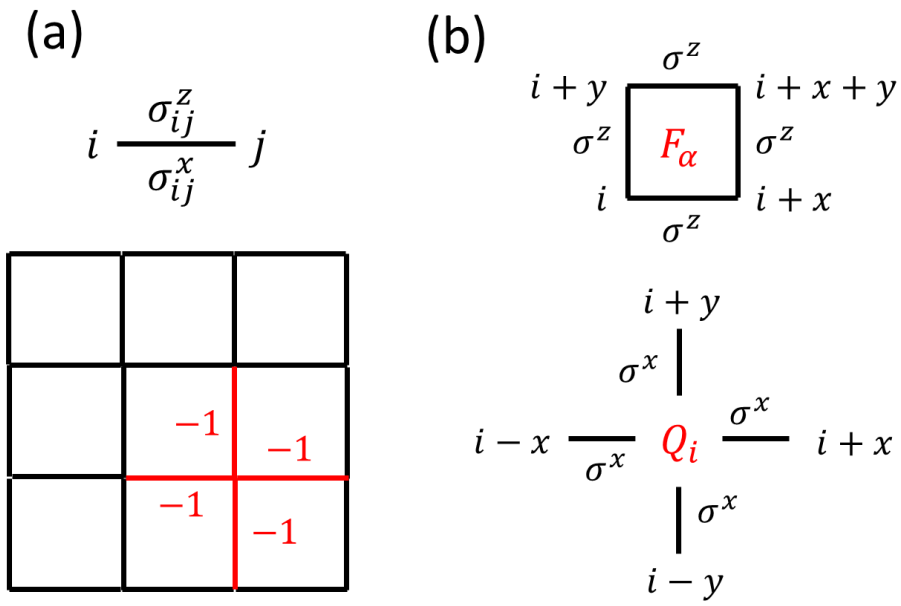

Figure 2.2: (a) In Ising gauge theory, the electric field operator σ^x_{ij} and link variable σ^z_{ij} are defined on the link ij. The elementary gauge transformation G_i maps σ^z to $-\sigma^z$ on the four red links attached to site i while keeps other link variables intact. (b) The flux F_α is defined as the product of four σ^zs around the plaquette α. The charge Q_i is defined as the product of the σ^xs on the four links attached to site i

In compact QED, the gauge potential A_{ij} is the canonical momentum conjugate to E_{ij}, and the link variable $\exp(\pm iA_{ij})$ are ladder operators of E_{ij}. In IGT, the link variable operator flips the two eigenvalues ± 1 of the electric field opreator σ^x_{ij}. Therefore, the natural choice for link variable operator is σ^z_{ij}. We define $\sigma^z_{ij} = \sigma^z_{ji}$ in accordance with the convention for σ^x_{ij}.

To recapitulate, the electric field operator and link variable operator on link ij are σ^x_{ij} and σ^z_{ij} in IGT, and they obey the standard Pauli matrices algebra,

$$(\sigma^x_{ij})^2 = (\sigma^z_{ij})^2 = 1, \quad \{\sigma^x_{ij}, \sigma^z_{ij}\} = 0. \tag{2.20}$$

Here $\{\cdots\}$ is the anti-commutator. Operators on different links commute.

In analogy to Eq. 2.13b, the magnetic flux operator F_α associated with a plaquette α is the contour product of link variables around the said plaquette,

$$F_\alpha = \sigma^z_{i,i+\hat{x}} \sigma^z_{i+\hat{x},i+\hat{x}+\hat{y}} \sigma^z_{i+\hat{y},i+\hat{x}+\hat{y}} \sigma^z_{i,i+\hat{y}}, \tag{2.21}$$

where i, $i+\hat{x}$, $i+\hat{y}$, and $i+\hat{x}+\hat{y}$ are the four corners of the plaquette (Fig. 2.2b). Note the eigenvalues of magnetic flux operator $\mathcal{F}_\alpha = \pm 1$ by definition, which corresponds to 0 and π magnetic field threading through the plaquette α.

The IGT Hamiltonian is then given by,

$$H = -\sum_\alpha F_\alpha - g \sum_{\langle i,j \rangle} \sigma^x_{ij}. \tag{2.22}$$

Here the first term is the magnetic energy, and the summation is over all plaquettes. The minus sign at the front ensures that 0 magnetic field (or flux +1) state has lower

energy. The second term is the electric energy, and the summation is over all links. g is a dimensionless coupling constant that controls the energy cost for promoting electric field from even (1) to odd (-1). Eq.2.22 is the main result of this section.

Similar to the compact QED, IGT possesses gauge invariance. The following gauge transformation,

$$\sigma^z_{ij} \to \eta_i \sigma^z_{ij} \eta_j, \tag{2.23}$$

leaves magnetic fluxes invariant. Here $\eta_i = \pm 1$ are c-numbers defined on lattice sites. All gauge transformation are generated by elementary gauge transformations. The elementary gauge transformation on site i, G_i, is defined by setting $\eta_i = -1$, and $\eta = 1$ on other sites (Fig. 2.2a). Its action on link variables is given by

$$G_i : \sigma^z_{ij} \to -\sigma^z_{ij}, \tag{2.24}$$

where ij are the four links emanating from i. The action of G_i on other links is trivial. G_i and the trivial transformation I form a group with composition rule $G_i^2 = I$, which is isomorphic to the cyclic group of order 2, Z_2. Thus, the gauge group is reduced from $U(1)$ to Z_2 comparing to the compact QED.

The elementary gauge transformation on site i is generated by the following operator,

$$G_i = \prod_{ij} \sigma^x_{ij} \equiv Q_i, \tag{2.25}$$

where ij are the four links emanating from i (Fig. 2.2b). In compact QED, gauge transformations are generated by charge operators. By analogy, we call the above

operator the charge operator on site i, and rename it Q_i to highlight this analogy. $Q_i^2 = 1$ from the definition. Incidentally, Q defined here can be thought of as the parity of the $U(1)$ charge.

Since the flux operators and the Hamiltonian are invariant under gauge transformation Eq. 2.23,

$$[Q_i, H] = [Q_i, F_\alpha] = 0, \quad \forall \alpha, i, \tag{2.26}$$

which can be derived from the definition and Eq. 2.20 as well.

2.4 Weak-coupling phase of IGT

Ising gauge theory (IGT) Hamiltonian Eq. 2.22 contains rich physics, which is controlled by the coupling constant g. In this section, we discuss the weak-coupling region, $|g| \ll 1$. Our strategy will be starting with the solvable limit $g = 0$ and treating finite g as perturbation.

When $g = 0$, Eq. 2.22 reduces to the following simple form,

$$H_0 = -\sum_\alpha F_\alpha. \tag{2.27}$$

It can be seen that $[F_\alpha, H_0] = [Q_i, H_0] = 0$ for all plaquettes α and sites i. Hence the charges and fluxes form a set of good quantum numbers. Now we show that the common eigenstates of all magnetic flux operators F_α span the IGT Hilbert space. In other words, their common eigenstates form a basis, dubbed "flux basis" in the

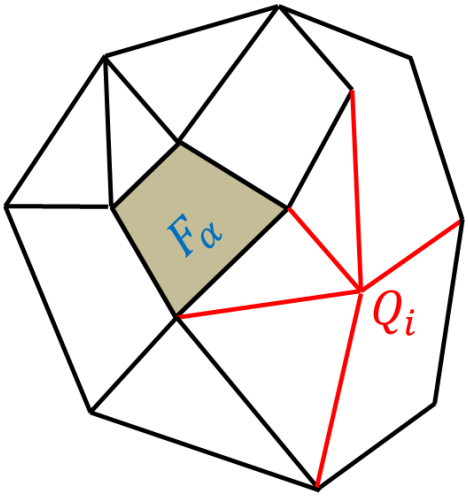

Figure 2.3: Ising gauge theory can be defined on a general graph. The flux operator is defined on the faces, whereas the charge operator is associated with vertices.

following discussion. Note that Hamiltonian Eq. 2.27 becomes diagonal in the flux basis.

For our purpose, it is more convenient to consider an arbitrary closed, connected graph instead of square lattice (Fig. 2.3). To simplify things, we assume that the graph is drawn on a spherical surface. The IGT Hamiltonian is generalized accordingly. The electric field operators σ^x_{ij} and the link variable operators σ^z_{ij} are defined on the edges of the graph. The electric charge operators Q_i are associated to the vertices whereas the magnetic flux operators F_α to the faces.

On the one hand, we can span the full Hilbert space by the common eigenstates of electric field operators σ^x_{ij}, i.e. the electric basis. The electric field operators are subject to the charge constraint, or Gauss's law constraint, $Q_i = q_i$. $q_i = \pm 1$ is the background charge on vertex i. However, not all of Gauss's law constraints are

independent,

$$\prod_i Q_i = 1. \tag{2.28}$$

The above identity is derived by noting the fact that each electric field operator is counted twice on the left hand side and $(\sigma_{ij}^x)^2 = 1$. Thus, the degrees of freedom is e, e being the number of edges in the graph, whereas the number of independent constraints is $v - 1$, v being the number of vertices. The Hilbert space dimension is therefore 2^{e-v+1}.

On the other hand, we compute the dimension of linear space spanned by the common eigenstates of F_α. Each each flux operator F_α takes two possible values. However, F_α are not independent,

$$\prod_\alpha F_\alpha = 1. \tag{2.29}$$

The above identity is derived in the same vein as Eq.2.28. The dimension of the linear space is 2^{f-1}, where f is the number of faces in the graph.

For graphs drawn on a sphere, Euler's formula gives $v - e + f = 2$, or equivalently $2^{v+f-2} = 2^e$ [11]. Therefore, the dimension of the linear space spanned by the common eigenstates of F_α is equal to the Hilbert space dimension. We see that the flux basis is complete.

Now we are ready to discuss the ground state and excitations. It is convenient to work in the flux basis. The basis vector are labeled as $|\{\mathcal{F}_\alpha\}\rangle$, where $\mathcal{F}_\alpha = \pm 1$ is the eigenvalue of F_α. In this basis, the Hamiltonian Eq.2.27 becomes diagonal, and the

energy eigenvalues are given by,

$$E = -\sum_{\alpha} \mathcal{F}_{\alpha}. \tag{2.30}$$

We first consider the ground state in vacuum. Since there is no charge, we set the Gauss's law constraint $Q_i = 1 \, \forall i$. We note the energy is minimized by setting $\mathcal{F}_{\alpha} = 1 \, \forall \alpha$. To create excitations from vacuum, we can flip the value of $\mathcal{F}_{\alpha}$. The energy cost for flipping $\mathcal{F}_{\alpha} = 1$ to -1 is 2. These flux excitations are known as visons in literature, and they are completely immobile when $g = 0$. Note that the visons must be created in pairs due to the constraint Eq. 2.29.

We can also consider the interaction between a pair of electric charges. To this end, we set $Q_x = -1$ and $Q_y = -1$, where x and y are two lattice sites, and $Q_i = 1$ for the rest. Again, the energy is minimized by setting $\mathcal{F}_{\alpha} = 1$ on all plaquettes α. It can be seen that the ground state energy doesn't depend on x or y, and thus there is no interaction between the electric charges when $g = 0$.

To recapitulate, we have shown that, on a planar lattice (graph), the spectrum of zero-coupling IGT Hamiltonian Eq. 2.27 is diagonal in the flux basis. The ground state in vacuum is unique, and there are vison excitations on top. The visons are gapped, and they are immobile when $g = 0$. There is no interaction between a pair of electric charges in this limit.

The above picture gets slightly modified when the coupling constant g is small but finite. Here we briefly comment on the consequences of finite $|g|$. Firstly, the energy cost for creating a vison is reduced when $|g|$ increases, and the visons can hop

from one plaquette to the neighboring plaquettes. Secondly, the interaction potential energy between a pair of charges is non-zero, and the potential decays exponentially as the distance between the charges increases. Finally, as the vison gap decreases as $|g|$ increases, the gap eventually closes when $|g|$ is sufficiently large, signaling a phase transition.

2.5 Topological degeneracy in IGT

In the previous section, we discussed the energy spectrum of IGT Hamiltonian by assuming that the underlying lattice or graph can be drawn on a sphere. In this section, we discuss IGT Hamiltonian defined on graphs with more complicated topology. We will show that, in the weak-coupling phase, every energy level is 4^n-fold degenerate in the thermodynamic limit, where n is the genus of the graph. Such degeneracy is protected by the topology of the underlying graph, and it is stable against any small perturbations.

To begin with, we consider again the zero-coupling Hamiltonian Eq. 2.27. In what follows, we show that there are a set of new, non-local operators that commute with Eq. 2.27. For the sake of concreteness, we focus on a finite $N \times N$ square lattice with periodic boundary condition imposed in both directions. This lattice can be drawn on a torus, and therefore the genus $n = 1$.

Consider an arbitrary, non-self-crossing, oriented loop γ in this lattice, the Wilson

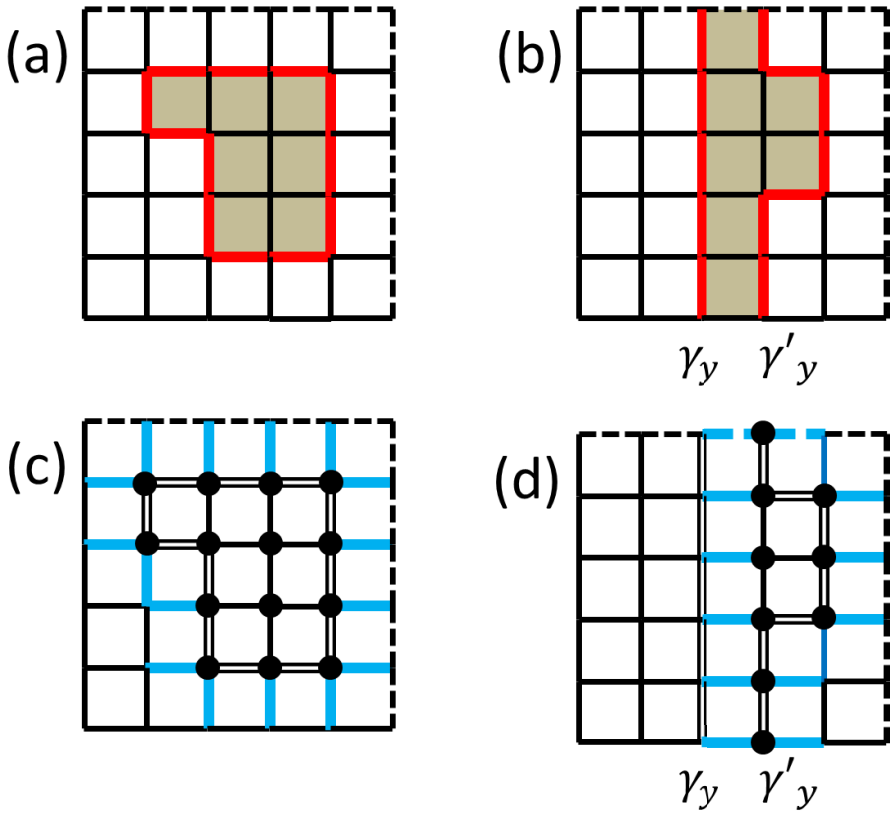

Figure 2.4: (a) A 5×5 square lattice. Periodic boundary condition is imposed on both horizontal and vertical directions. Links on opposite sides are regarded as identical. Wilson loop operator $W[\gamma]$ associated with a loop γ (red) is defined as the product of σ^z on all the links belong to γ. When γ is contractible, $W[\gamma]$ is equal to the product of flux F_α over all plaquettes α (shaded in gray) enclosed by γ. (b) Wilson loop operators associated with two homotopic paths (red) are related to each other through flux operators on plaquettes (shaded in gray) enclosed by the two paths. (c) Electric loop operator $X[\gamma]$ associated with a loop γ (double-line) is defined as the product of σ^x on the R-legs (blue) of γ. When γ is contractible, $X[\gamma]$ is equal to the product of charge enclosed by γ (black dots). (d) Electric loop operators associated with two homotopic paths (double-line) are related to each other through charge operators (black dots) enclosed by the two paths.

loop operator associated with this path is defined as

$$W(\gamma) = \prod_{ij \in \gamma_1} \sigma_{ij}^z. \tag{2.31}$$

Here the multiplication is over all the links ij that belong to path γ (Fig. 2.4a). $W(\gamma)_1^2 = 1$ by definition. $W(\gamma)$ is simply the magnetic flux that threads through γ, and it is gauge invariant. Therefore,

$$[W(\gamma), Q_i] = 0, \quad \forall i. \tag{2.32}$$

Wilson loop operators commute with the Hamiltonian,

$$[W(\gamma), H_0] = [W(\gamma), F_\alpha] = 0, \tag{2.33}$$

which trivially follows from the definition. The Wilson loop operators are good quantum numbers.

However, all $W(\gamma)$ are not independent. When γ is a loop is contractible, it is related to the magnetic fluxes operators F_α by

$$W(\gamma) = \prod_{\alpha \text{ enclosed by } \gamma} F_\alpha. \tag{2.34}$$

Here the multiplication is over all plaquettes enclosed by the loop γ, i.e. lies on the left hand side of the path (Fig. 2.4a). Thus, when γ is contractible, $W(\gamma)$ are not new conserved quantities; they are simply products of known conserved quantities. The reverse is also true: the product of magnetic flux operators F_α generate all Wilson loop operators associated with contractible loops.

We then consider non-contractible loop, the loops that wind around the torus. From our analysis above, they cannot be written as product of F_α. Yet, they are not all independent. Consider two vertical loops γ_y and γ'_y shown in Fig. 2.4b. the Wilson loop operators $W(\gamma_y)$ and $W(\gamma'_y)$ are related to each other by,

$$W(\gamma_y) = \prod_\alpha F_\alpha \cdot W(\gamma'_y), \tag{2.35}$$

where α are plaquettes in the area bounded by γ_y and γ'_y. Therefore, we see that the two non-contractible loops are related if they are homotopic, i.e. if they can be smoothly deformed into each other. In other words, there is only one independent Wilson loop operator per one homotopy-equivalence class.

There are two homotopy-inequivalent, non-contractible, non-self-crossing loops in the lattice we consider. They are the vertical path, γ_y, and horizontal path, γ_x, that wind around the torus. Hence, there are two independent good quantum numbers $W_x \equiv W(\gamma_x)$ and $W_y \equiv W(\gamma_y)$ in addition to charge and flux operators (Fig. 2.5a).

In addition to Wilson loop operators, we can also define the electric loop operator associated with a non-self-crossing, oriented loop γ,

$$X(\gamma) = \prod_{ij \in \text{R-legs}} \sigma^x_{ij}. \tag{2.36}$$

Here the multiplication is over all the links that share one site with γ and lie on its right hand side, which are coined as R-legs of γ (Fig. 2.4c). $X(\gamma)$ measures the total electric charge enclosed by γ, and $X(\gamma)^2 = 1$ by definition.

$$[X(\gamma), F_\alpha] = 0, \quad \forall \alpha, \tag{2.37}$$

which comes from the fact that F_α shares even number of links with γ, whereby flips the value of $X(\gamma)$ even times. It then follows that $[X(\gamma), H_0] = 0$. It is also easy to see that $[X(\gamma), Q_i] = 0$.

Similar to the Wilson loop operators, two electric loop operators $X(\gamma)$ and $X(\gamma')$ are related to each other if γ and γ' are homotopic. In particular, when γ is contractible, $X(\gamma)$ is simply the product of charge operators (Fig. 2.4c,d),

$$X(\gamma) = \prod_{i \text{ enclosed by } \gamma} Q_i. \tag{2.38}$$

Thus, there are only two independent electric loop operators $X_x \equiv X(\gamma_x)$ and $X_y \equiv X(\gamma_y)$, associated to the paths γ_x and γ_y that wind around the torus (Fig. 2.5a).

To sum up, we have identified four independent, non-local operators that commute with Eq. 2.27: W_x, W_y, X_x, and X_y. However, they do not commute among themselves. Specifically,

$$[W_x, X_x] = [W_y, X_y] = 0, \tag{2.39a}$$

$$\{W_x, X_y\} = \{W_y, X_x\} = 0. \tag{2.39b}$$

The first anti-commutation given above is derived by noting that W_x and X_y share one link ij, and $\{\sigma^x_{ij}, \sigma^z_{ij}\} = 0$ (Fig. 2.5a). The second one is derived in the same vein.

Now we examine the Hilbert space structure of the IGT. We note that the electric loop operators X_x and X_y are good quantum numbers, and they commute with the Hamiltonian. We can impose a generalized Gauss's law constraint $X_x = \pm 1$ and $X_y = \pm 1$, in addition to the local, vertex-wise Gauss's law constraints $Q_i = \pm 1$.

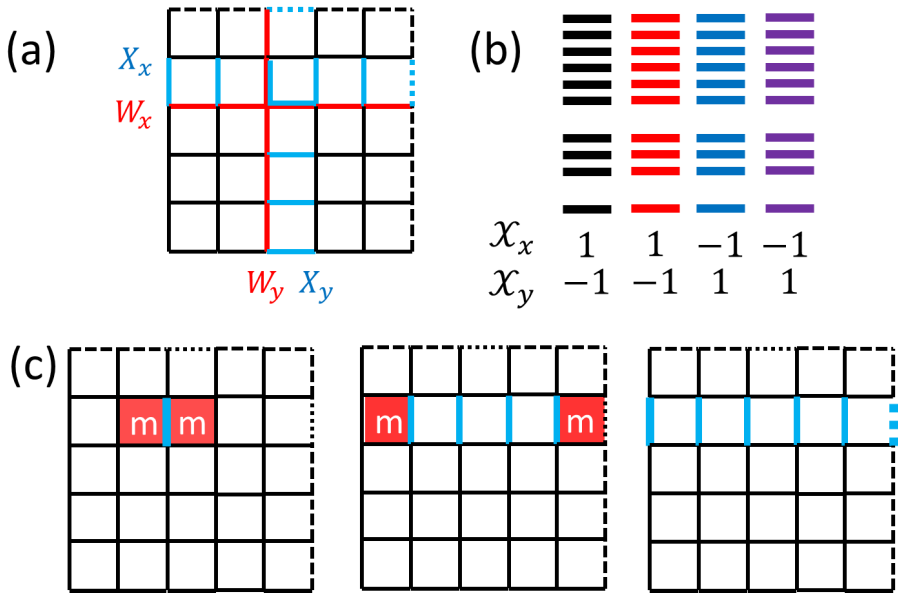

Figure 2.5: (a) The four independent loop operators. Note that W_x and X_y share one link, and so do W_y and X_x. (b) The spectrum of the Ising gauge theory Hamiltonian defined on a torus. The four sectors have exactly identical spectra in the thermal dynamical limit, and they cannot be mixed by local operators. (c) A pair of visons are created from vacuum. They can be separated apart and meet again when they circle around the torus. When they meet, they annihilate and the system goes back to vacuum.

Thus, the number of independent constraints is $v-1+2=v+1$. The Hilbert space dimension is 2^{e-v-1}.

To check if the common eigenstates of the flux operators F_α form a complete basis, we carry out dimension counting. There are $f-1$ indepdent flux operators (Eq.2.29). The dimension of the linear span of their common eigenstates is 2^{f-1}. According to the Euler's formula, $v+f-e=0$ for closed graphs drawn on torus [11]. Thus, the dimension of the linear span is equal to the Hilbert space dimension, $2^{f-1}=2^{e-v-1}$. The flux basis is indeed complete.

The Hamiltonian H_0 (Eq. 2.27) becomes diagonal in the flux basis,

$$E = -\sum_{\alpha} \mathcal{F}_{\alpha}. \tag{2.40}$$

We note that the energy does not depend on the constraint $X(\gamma_{x,y}) = \pm 1$. Consequently, if each energy level is four-fold degenerate at least if we do not distinguish the constraints imposed on $X_{x,y}$. This result can also be derived from the algebra Eq. 2.39. Let $|\mathcal{X}_x = 1, \mathcal{X}_y = 1\rangle$ be an eigenstate of H_0 with energy E. On the one hand,

$$\begin{aligned} X(\gamma_x)W(\gamma_x)|1,1\rangle = W(\gamma_x)X(\gamma_x)|1,1\rangle = W(\gamma_x)|1,1\rangle. \\ X(\gamma_y)W(\gamma_x)|1,1\rangle = -W(\gamma_x)X(\gamma_y)|1,1\rangle = -W(\gamma_x)|1,1\rangle. \end{aligned} \tag{2.41}$$

Therefore, $W(\gamma_x)|1,1\rangle = |1,-1\rangle$. On the other hand,

$$H_0 W(\gamma_x)|1,1\rangle = W(\gamma_x)H_0|1,1\rangle = EW(\gamma_x)|1,1\rangle. \tag{2.42}$$

We see that $|1,-1\rangle$ is degenerate with $|1,1\rangle$. By the same token, we can show that the quartet $|\mathcal{X}_x = \pm 1, \mathcal{X}_y = \pm 1\rangle$ are degenerate (Fig. 2.5b).

The quartet can not be mixed by any local perturbation. We note that, any local, physical operator O must be a function of flux operators F_α and electric field operators σ^x_{ij} as they are the only local, gauge-invariant objects. Thus, $[O, X(\gamma_x)] = [O, X(\gamma_y)] = 0$. Since O cannot change the eigenvalue of $W(\gamma_{x,y})$,

$$\langle \mathcal{X}_x, \mathcal{X}_y | O | \mathcal{X}'_x, \mathcal{X}'_y \rangle = 0. \tag{2.43}$$

In other words, the Hilbert space of IGT on torus are decomposed into four superselection sectors, known as topological sectors. States in different topological sectors are not mixed by local operators.

The quartet remain quasi-degenerate when $|g|$ is small but finite. When $g \neq 0$, the electric loop operators are still good quantum numbers, $[X(\gamma_{x,y}), H] = 0$. Therefore, we can label all states by their eigenvalues, $|\mathcal{X}_x, \mathcal{X}_y\rangle$. When $g = 0$, the four states are strictly degenerate on finite lattice of size $N \times N$. To find eigenstates for $g \neq 0$, we perform degenerate perturbation theory. In the leading order, the action of electric field operator σ^x_{ij} creates a pair of visons from the ground state (Fig. 2.5c). At higher orders, the visons are separated further apart. Eventually, at N-th order, the visons circle around the torus and annihilate, and we go back to the initial ground state. Therefore, we deduce that the energy correction is given by,

$$\Delta E \sim |g|^N \sim e^{-N/\xi}, \tag{2.44}$$

where ξ is some length scale. The correction is exponentially small, and the quartet remains quasi-degenerate. In the thermodynamical limit, $N \to \infty$, the 4-fold degeneracy is restored.

We close this section by pointing out that the above results can be readily generalized to graph with any genus n. As there are $2n$ homotopy-inequivalent close paths, there are $2n$ non-local good quantum numbers $X(\gamma_i)$. Therefore, even energy level becomes 4^n-fold degenerate. Generalization to lattice embedded in non-orientable surface is also possible. The intimate relationship between the energy spectrum and

the topology of underlying space is not unique to IGT; it is a common trait of a large family of quantum field theories known as topological quantum field theory [10]. IGT is the simplest topological quantum field theory.

2.6 Strong-coupling phase of IGT

In this section, we analyze the strong-coupling phase of Ising gauge theory (IGT). The strategy is similar to the analysis of the weak-coupling phase : we first consider the $g \to \infty$ limit and then treat $1/g$ as perturbation.

In the limit of $g \to \infty$, the IGT Hamiltonian Eq.2.22 reduces to the following,

$$H_\infty = -g \sum_{ij} \sigma^x_{ij}. \tag{2.45}$$

Thus, the Hamiltonian becomes diagonal in the electric basis. The energy levels are given by,

$$E = -g \sum_{ij} \mathcal{E}_{ij}, \tag{2.46}$$

where $\mathcal{E}_{ij}$ is the eigenvalue of σ^x_{ij}.

The energy is minimized by setting all $\mathcal{E}_{ij} = 1$, which determines the ground state. In particular, the charge $Q_i = 1$ for all sites i, which corresponds to the vacuum (charge-free). To create excited states, we flip $\mathcal{E}_{ij}$ from 1 to -1. However, we want to ensure the constraint $Q_i = 1$ in vacuum, and therefore we must flip $\mathcal{E}_{ij}$ around a loop (Fig. 2.6). Therefore, the excitations are simply closed electric field

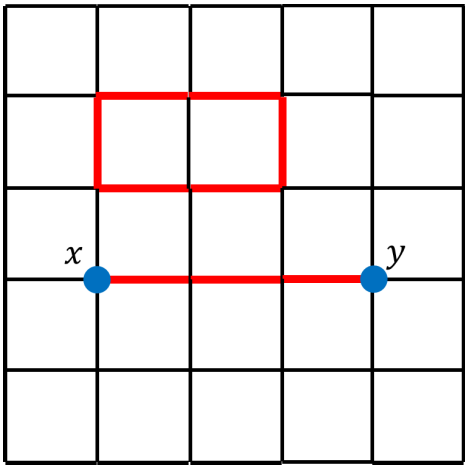

Figure 2.6: The excitations in vacuum are closed electric field lines, or electric strings, and the energy cost is proportional to the length of the string. $\mathcal{E} = -1$ on the red links and 1 on black links. Point charges (blue dots) are bound by an open string.

lines known as closed electric strings in literature. The energy cost for a string of length L is $2gL$. The string tension is $2g$.

We then consider the interaction between a pair of electric charges. To this end, we set $Q_x = -1$ and $Q_y = -1$, where x, y are two lattice sites, and $Q_i = 1$ for the rest. Again, the energy is minimized by setting $\mathcal{E}_{ij} = 1$. However, to comply with the charge constraint, we must set $\mathcal{E}_{ij} = -1$ along a path that connects x, y, i.e. to create an open electric string between x and y (Fig. 2.6). The ground state energy is then obtained by choosing the shortest path,

$$E_{\text{pair}} = E_{\text{vac}} + 2gD(x, y), \tag{2.47}$$

where $D(x, y)$ is the Manhattan distance between x and y, and E_{vac} is the ground state energy in vacuum (without charge). The charges are thus confined by a potential that linear increases with the spatial separation.

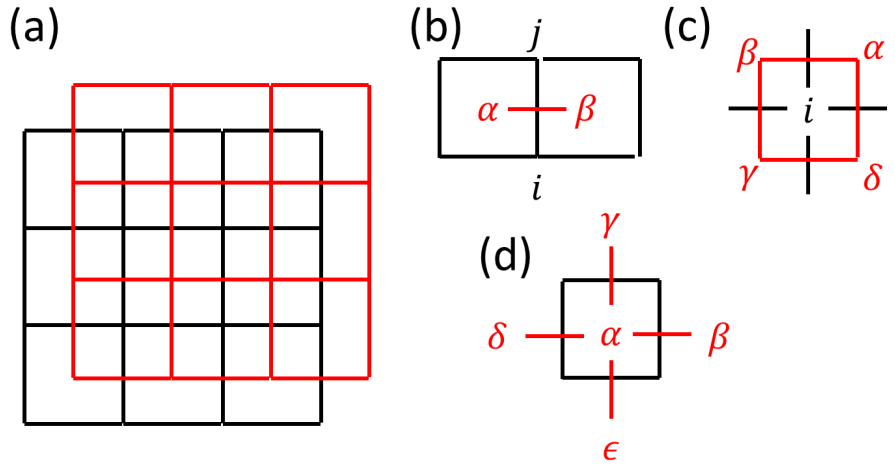

Figure 2.7: (a) The square lattice and its dual lattice. (b) The electric field σ^x_{ij} is dual to the product of dual Ising variables $\tau^z_{\alpha,\beta}$. (c) Charge operator Q_i is dual to the product of $\lambda_{\alpha\beta}$ enclosing i. (d) The flux operator F_α flips the eigenvalue of electric operators σ^x on the edges of α. The operator τ^x_α flips the value of τ^z_α, thereby flipping the value of the products $\tau^z_\alpha\tau^z_\beta$, $\tau^z_\alpha\tau^z_\gamma$, etc, which are dual to σ^x on the edges of plaquette α. Thus, F_α is dual to τ^x_α as they have the same action on electric field operators.

When g is finite, perturbation calculations show that the string tension is reduced, and it may become zero when g decreases, which signals a phase transition toward the weak-coupling phase.

2.7 Duality transformation

In Section 2.4 and Section 2.4, we have established that the Ising guage theory (IGT) shows distinct phases at weak and strong couplings. In the weak-coupling phase ($g \to 0$), the interaction potential between a pair of electric charge decays exponentially as the distance increases. This is in contrast to the strong coupling

phase ($g \to \infty$), where the interaction potential grows linearly with distance. We expect the two phases are separated by a phase transition at critical coupling g_c.

In this section, we seek to understand the phase transition from a different perspective. We employ a powerful non-perturbative technique known as the duality transformation, which maps the IGT to the ordinary transverse field Ising model (TFIM). In particular, the weak and strong coupling phases of IGT are respectively mapped to the paramagnetic and ferromagnetic phases of the TFIM, and the confinement transition in the former model is mapped to the magnetic phase transition in the latter. For the sake of concreteness, we will consider the IGT defined a $N \times N$ square lattice with periodic boundary condition.

The dual Ising variables τ^z_α are defined on the plaquettes α. These plaquettes, regarded as lattice sites, form another square lattice that is dual to the original (Fig.2.7a). The electric field operators σ^x_{ij} are related to the dual Ising variables by,

$$\sigma^x_{ij} = \lambda_{\alpha\beta}\tau^z_\alpha\tau^z_\beta. \tag{2.48}$$

where plaquettes α and β share the link ij (Fig.2.7b). $\lambda_{\alpha\beta} = \pm 1$ are phase factors defined on the links of the dual square lattice. The charge operators then become,

$$Q_i = \prod_{\alpha\beta} \lambda_{\alpha\beta}. \tag{2.49}$$

Here the multiplication is over the dual links $\alpha\beta$ that surround the site i (Fig. 2.7c). The charge operator Q is dual to a c-number, reflecting the fact that the charge is static in IGT. Remarkably, the charge constraint in IGT is dual to flux conditions of

the phase factors.

As shown in Section 2.5, there are two electric loop operators $X[\gamma_{x,y}]$ associated with the two non-contractible paths,

$$X[\gamma_{x,y}] = \prod_{\alpha\beta} \lambda_{\alpha\beta}, \tag{2.50}$$

where the multiplication is over the dual links $\alpha\beta$ that belong to the non-contractible paths $\gamma_{x,y}$ in the dual lattice. Hence, the electric fluxes are dual to the Z_2 flux of the phase factors.

The magnetic plaquette operators F_α flips the eigenstates of the electric operators σ^x_{ij} around the plaquette α. It can be seen that the dual operator τ^z_α has the same action on electric field operators (Fig.2.7d). Therefore, we identify,

$$F_\alpha = \tau^x_\alpha. \tag{2.51}$$

Substituting Eq. 2.48 and Eq. 2.51 into the IGT Hamiltonian Eq. 2.22, we find the dual Hamiltonian,

$$H_{\text{dual}} = -\sum_\alpha \tau^x_\alpha - g \sum_{\alpha\beta} \lambda_{\alpha\beta} \tau^z_\alpha \tau^z_\beta. \tag{2.52}$$

In the dual model, the magnetic term in IGT becomes the transverse field, and the electric term becomes the nearest-neighbor Ising interaction. The dual Ising variables are coupled to Z_2 phase factors $\lambda_{\alpha\beta}$, and their fluxes are determined by the charge Q_i in the original IGT (Eq. 2.49).

In what follows, we focus on the vacuum ($Q_i = 1, \forall i$), and the topological sector $X[\gamma_{x,y}] = 1$. In the dual theory, we set $\lambda_{\alpha\beta} = 1$ and obtain the following standard

transverse-field Ising model,

$$H_{\mathrm{TFIM}} = -\sum_{\alpha} \tau_{\alpha}^{x} - g \sum_{\alpha\beta} \tau_{\alpha}^{z} \tau_{\beta}^{z}. \tag{2.53}$$

When $g \gg 1$, the Ising coupling dominates, and the model is in the ferromagnetic phase. When $g \ll 1$, the transverse field dominates, and the system is in the paramagnetic phase. Therefore, the strong and weak coupling phases of IGT are mapped to the ferromagnetic and paramagnetic phases of the dual model. The confinement phase transition is then dual to the well-understood magnetic ordering transition in the transverse field Ising model.

We close this section by remarking that duality transformation is readily generalized to other lattices and it can be developed for other Abelien gauge theories as well [8, 9].

Chapter 3

Kagome Heisenberg antiferromagnet

In Chapter 1, we showed that a frustrated magnet could remain paramagnetic down to zero temperature, thereby becoming a spin liquid. In this chapter, we study a promising candidate for spin liquid, the $S = 1/2$ kagome Heisenberg antiferromagnet (KHAF).

The Hamiltonian of the $S = 1/2$ KHAF is given by

$$H = \sum_{\langle ij \rangle} \mathbf{S}_i \cdot \mathbf{S}_j, \tag{3.1}$$

where $\mathbf{S}_i$ are $S = 1/2$ spin operators defined on lattice sites of kagome, and the summation is over nearest-neighbors. Here we have set the exchange coupling constant to 1. Despite its simplicity, determining the ground state of Eq. 3.1 has been proven to be a formidable task. More than a dozen competing proposals for the nature of its

ground state have been made over the past two decades [12–19].

Recent numerical studies based on the density-matrix renormalization group (DMRG) method cast new light on this problem [20–22]. They provide compelling evidence for a spin liquid. In the ground state, spins have very short-ranged correlations, gapped $S = 1$ excitations, and no discernible sign of long-range magnetic order. These results are consistent with a particular type of spin liquid known as resonating-valence-bond (RVB) state [23].

The numerical studies have revealed a wealth of new features that remain to be understood, including a strong valence-bond resonance around diamond-shaped loops and peculiar valence-bond correlations near lattice defects [20, 21]. The ground state of Eq. 3.1 with cylindrical geometry shows a strong dependence on the circumference and the chirality of the cylinder. Localized $S = 1/2$ spins are found on the open edges of certain types of cylinders. These numerical findings call for a theoretical assessment.

We provide a phenomenology of the spin-liquid phase of the $S = 1/2$ KHAF, which bridges the theory and the numerics. We demonstrate that the kagome quantum dimer model is naturally described in the language of an IGT. We construct an IGT and show that the model indeed reproduces qualitatively various features of the ground state of the $S = 1/2$ KHAF revealed by the DMRG studies. Our results have been previously published in [24].

The current chapter is organized as follows. We review the physical properties of

the RVB state in Section 3.1. Then, in Section 3.2, we construct the phenomenological model. In Section 3.3 we describe techniques for solving the model. In Section 3.4, Section 3.5, and Section 3.6, we solve the model in various settings and compare the solutions with the numerical results. We discuss the methodological aspects of our work in Section 3.7.

3.1 Physics of RVB state

As we have mentioned earlier, the DMRG results suggest that the ground state of $S = 1/2$ KHAF is a RVB state. In this section, we review the basic physical properties of the RVB state.

The RVB state was first conceived by P. W. Anderson in 1973 [23]. The idea of the RVB state comes from the following elementary observation. When two $S = 1/2$ spins are coupled through antiferromagnetic exchange interaction, the ground state is a total $S = 0$ state or a singlet. In an antiferromagnet, adjacent $S = 1/2$ spins tend to pair up to form singlets (Fig. 3.1a, left panel). There are numerous ways to pair neighboring spins, and the antiferromagnet can easily tunnel from one pairing pattern to another. As a result, the ground state is a quantum superposition of different pairing patterns, and such a state is known as a resonating-valence-bond (RVB) state. Schematically,

$$|\mathrm{RVB}\rangle = \sum_D \psi(D)|D\rangle. \tag{3.2}$$

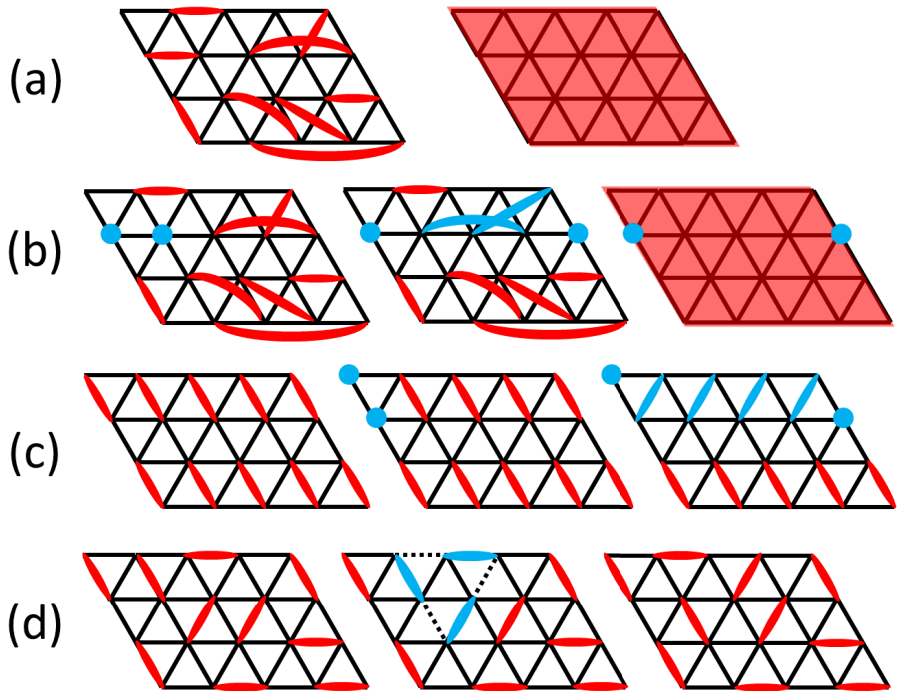

Figure 3.1: (a) In an antiferromagnet, spins tend to pair up to form $S = 0$ singlets (left panel, red ellipses). A RVB state is a quantum superposition of various quantum tunneling patterns, which preserves all the symmetries of the system (right panel). (b) $S = 1$ excitations in a RVB state are made of two unpaired spins (left panel, blue dots), and they can move in a RVB state by rearranging singlets (middle panel, blue ellipses). The disturbance left behind a moving spinon can be repaired by quantum tunneling, and the unpaired spins behave as individual $S = 1/2$ particles (right panel, blue dots). (c) In a valence-bond solid, the singlets form a static pattern that breaks the lattice symmetry (left panel). When spinons are created and separated, the trail left behind cannot be repaired (right panel). (d) In quantum dimer model, nerarest neighbor spins pair up into singlets, or dimers. The Hamiltonian acts on the space of dimer coverings (left panel). A tunneling process involves shifting dimers around a closed loop (middle panel, blue ellipses and dashed links), whereby a new dimer covering is obtained (right panel).

Here D stands for the pairing pattern of spins, and $|D\rangle$ the spin state corresponds to this pairing. For instance, if spins 1 and 2 are paired, and spins 3 and 4 are paired, then $|D\rangle = |0\rangle_{12}|0\rangle_{34}$, $|0\rangle_{ij}$ denoting the singlet made of spins i and j. $\psi(D)$ is the amplitude of pairing pattern D. The state Eq. 3.2 is invariant under spin rotation since the building blocks are singlets. If the amplitude $\psi(D)$ also respects lattice symmetries, then the state Eq. 3.2 is a quantum spin liquid (Fig. 3.1a, right panel).

The RVB state hosts fractional excitations. To create a $S = 1$ spin excitation, we break up a singlet into two unpaired spins (Fig. 3.1b, left panel). When the unpaired spins move, they leave behind a trail of disturbance (Fig. 3.1b, middle panel), which can be repaired by quantum tunneling. Consequently, the energy cost for separating these two spins is finite. The unpaired spins thus can be thought of as two independent $S = 1/2$ excitations (Fig. 3.1b, right panel). In short, the $S = 1$ excitation in the RVB state fractionalizes into two spinons.

However, if the quantum tunneling between various pairing pattern is absent, then the singlets freeze into a static pattern, known as valence bond crystal in literature [25–27]. The spinons are confined in valence bond solids. To see this, we consider a simple valence bond solid state shown in Fig. 3.1c, left panel. Similarly, we can create a pair of spinons by breaking a singlet into two spinons (Fig. 3.1c, middle panel). In this case, the trail behind a moving spinon cannot be repaired by tunneling, and there is energy cost that is proportional to the spatial separation of the spinons (Fig. 3.1c, right panel).

The above intuitive picture is captured by a concrete model known as the quantum dimer model [28], which is a quantum analog of the classical dimer model proposed earlier [29, 30]. In this model, neighboring spins on a lattice are paired up into singlets (Fig. 3.1d, left panel). Each singlet is represented as a dimer that covers two adjacent lattice sites. A pairing pattern of spins is then pictorially represented as a dimer covering of the lattice. Since a spin can only participate in one singlet, a lattice site can only be covered by one dimer.

The Hamiltonian of a quantum dimer model then acts on the space of dimer coverings. The kinetic terms in the Hamiltonian describes various local tunneling processes of dimer coverings (Fig. 3.1d, middle and right panels). Note that the tunneling process must respect the condition that each site is covered by one dimer. Since different dimer coverings could cost different energy, there could also be potential terms in the quantum dimer model Hamiltonian.

3.2 Construction of the model

In this section we construct a phenomenological model describing the spin-liquid phase of the $S = 1/2$ KHAF. Our starting point is a quantum dimer model on kagome that is thought to represent low-energy states of the Heisenberg model in the sector with zero total spin. We first show that the Hilbert space of kagome quantum dimer model is identical to that of an IGT on honeycomb, whose sites are centers

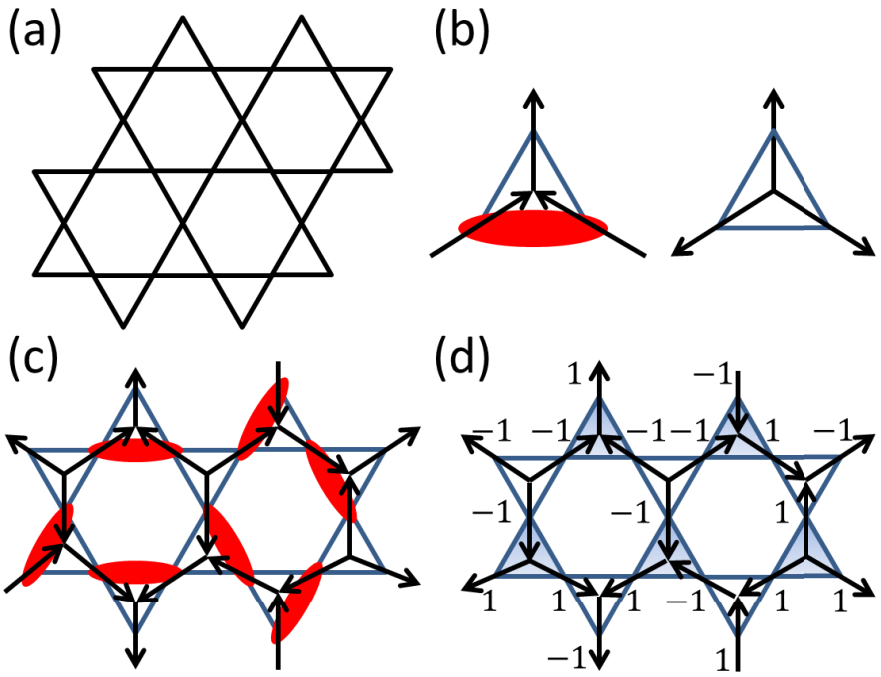

Figure 3.2: (a) The kagome Heisenberg antiferromagnet. $S = 1/2$ spins are located on the lattice sites, and the antiferromagnetic Heisenberg interactions are between nearest-neighboring spins. (b) The rules of the arrow representation of the dimer coverings. (c) An example of the arrow representation. (d) Mapping the arrow patterns to Ising variables. The centers of shaded (unshaded) triangles are A (B) sites of the honeycomb.

of kagome triangles. We recast the quantum dimer model Hamiltonian of Misguich, Serban, and Pasquier (MSP) [31], known to have a RVB ground state, as an IGT. We then perturb the MSP Hamiltonian by adding dimer interactions consistent with the lattice symmetry. We keep only the leading terms beyond the MSP model in our phenomenological model.

The starting point is a quantum dimer model on kagome first investigated by Zeng and Elser [32]. The basic assumption is that nearest-neighbor singlet coverings span the low-energy subspace of Eq. 3.1 with total spin $S = 0$.

Elser and Zeng mapped dimer coverings on kagome to patterns of arrows connecting centers of adjacent triangles [33]. The centers of triangles in kagome form a honeycomb, and thus the arrows reside on the links of honeycomb. On a triangle with a dimer, one arrow points out of the triangle and away from the dimer; the other two arrows point into the triangle. A triangle without a dimer has three arrows pointing out. The mapping is illustrated in Fig. 3.2b. It is easy to check that the arrows are subject to a constraint: each vertex of the honeycomb lattice has either one outgoing and two incoming arrows, or three outgoing arrows. An example of such a mapping is shown in Fig. 3.2c.

We introduce Ising variables $\sigma^x_{ij} \equiv \sigma^x_{ji} = \pm 1$, defined on the links of the honeycomb, to parametrize the states of the arrows. To this end, we partition the honeycomb sites into A and B sublattices. For a given honeycomb link $\langle ij \rangle$, $\sigma^x_{ij} = 1$ if the arrow points from the A site to the B site, and -1 otherwise (Fig. 3.2d). The constraint on arrows is thereby translated to a constraint on Ising variables:

$$Q_i \equiv \sigma^x_{i1}\sigma^x_{i2}\sigma^x_{i3} = \begin{cases} 1 & i \in A \\ -1 & i \in B \end{cases} . \tag{3.3}$$

Here i denotes a site on the honeycomb lattice, whereas $\langle i1 \rangle$,$\langle i2 \rangle$, and $\langle i3 \rangle$ are the three links emanating from the site i.

We interpret the variables σ^x_{ij} as the electric field operators of the IGT on honeycomb. The constraint Eq. 3.3 then becomes Gauss's law of the IGT, and Q_i is the charge on a honeycomb site i.

We have thus established that the Hilbert space of a kagome quantum dimer model is identical to that of an IGT on honeycomb with staggered, static background charges (3.3). As a result, any kagome quantum dimer model Hamiltonian can be written as an IGT Hamiltonian.

The MSP Hamiltonian describes the simplest, exactly solvable quantum dimer model on kagome [31]. Its ground state is an equal-amplitude superposition of all possible dimer coverings, which is a Rokhsar-Kivelson state on kagome [28]. Here we will motivate the MSP Hamiltonian from the gauge theory perspective.

We have associated the dimer covering to the electric field. Now we consider the magnetic fluxes in IGT. The magnetic flux operator associated with a hexagonal plaquette of the honeycomb is defined as,

$$F_\alpha = \prod_{ij\in\alpha} \sigma^z_{ij}. \tag{3.4}$$

Here σ^z_{ij} are the link variables in IGT, and the product is over the edges of the plaquette α. We consider the IGT Hamiltonian containing only the magnetic term:

$$H_{\rm MSP} = -\sum_\alpha F_\alpha, \tag{3.5}$$

The summation is over all hexagonal plaquettes. F_α reverses all arrows around hexagon α regardless of the initial orientation. In terms of dimers on kagome, F_α shifts dimers along a closed path within a David star with amplitude -1, which is identical to the operator "$\sigma^x(h)$" defined by Misguich *et al* [31]. Thus, the Hamiltonian Eq. 3.5 is nothing but the MSP Hamiltonian formulated in the language of

IGT.

As shown in Section 2.4, the MSP Hamiltonian Eq. 3.5 is diagonal in charge-flux basis. The ground state obeys $\mathcal{F}_\alpha = 1, \forall\alpha$. In electric basis, the (unnormalized) ground state is given by,

$$|G\rangle = \sum_{\{\mathcal{E}_{ij}=\pm 1\}} |\{\mathcal{E}_{ij}\}\rangle. \tag{3.6}$$

Here the summation is over all possible electric basis states obeying charge constraint Eq.3.3. The ground state is the equal amplitude superposition of all possible electric field configurations. Since the electric fields are tied to the dimer coverings, the ground state is the equal amplitude superposition of dimer coverings on kagome. Such a state apparently preserves all the symmetries of the Hamiltonian, just as expected for a RVB state. It also has been shown to exhibit short-range correlations [31]. From our discussion in Chapter 2, the excited states of Eq. 3.5 are visons, and the energy cost for each vison is 2. Visons are completely localized and dispersionless in the MSP Hamiltonian.

The MSP Hamiltonian Eq.3.5 is unfortunately too simple to account for the rich features observed in DMRG numerics. For instance, the response to the insertion of a lattice defect is confined to its immediate neighborhood as opposed to the ripple-like features observed in DMRG calculations [34]. Yet, the MSP Hamiltonian provides a natural starting point for the construction of a phenomenological IGT. In what follows, we perturb the MSP model by adding the electric term to the Hamiltonian. From the viewpoint of lattice gauge theory, this is natural as an IGT Hamiltonian

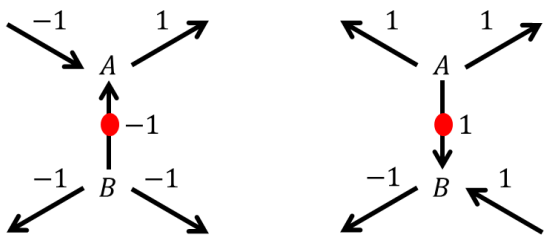

Figure 3.3: Transformation of σ^x operators: under a π rotation with respect to the midpoint of the bond ij (red dot), the orientation of the arrow on that bond is reversed. Note that the A and B labels of the sublattices do not change as we do not rotate the lattice itself. The value of the variable σ^x_{ij} therefore flips sign according to our mapping.

usually contains both electric and magnetic terms. From the quantum dimer model perspective, this amounts to including interacting potential between dimers.

We consider generic interactions up to the second order in the electric field operators σ_x:

$$V = -\sum_{\langle ij\rangle} A^{(1)}_{ij}\sigma^x_{ij} - \sum_{\langle ij\rangle,\langle kl\rangle} A^{(2)}_{ij;kl}\sigma^x_{ij}\sigma^x_{kl}, \tag{3.7}$$

The coupling constants $A^{(1)}_{ij}$, $A^{(2)}_{ij;kl}$ must be compatible with the symmetries of kagome and honeycomb.

We first show that the linear terms are not allowed because they violate some lattice symmetries. A π rotation about a kagome vertex shared by triangles i and j reverses the arrow on honeycomb link $\langle ij\rangle$. This alters the sign of the electric field, $\sigma^x_{ij} \to -\sigma^x_{ij}$, hence $A^{(1)}_{ij} = 0$ (Fig.3.3). Physically, a linear term expresses a preference for some dimer configuration, any of which violates the full symmetry of kagome.

We next establish that second-order interactions vanish for honeycomb links that share a site, e.g., $\langle 12\rangle$ and $\langle 24\rangle$ (nearest neighbors, distance 1/2 lattice spacing) shown

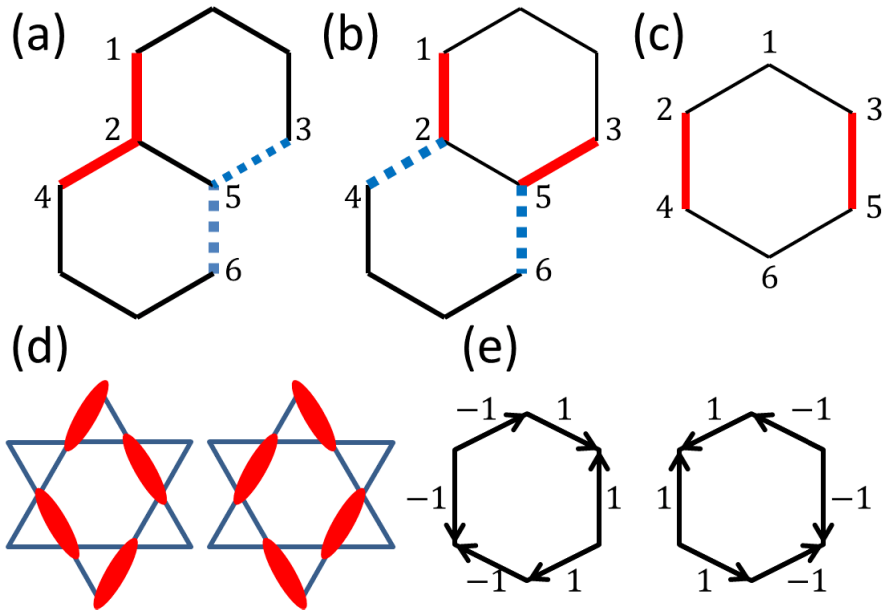

Figure 3.4: (a) The links highlighted in red (thick solid) are a pair of nearest neighbors, and the links highlighted in blue (thick dashed) are another pair. (b) Similar to (a), the links highlighted in the same format are second neighbors. (c) A pair of third neighbor links are highlighted in red (thick solid). (d) The two quasi-degenerate dimer coverings in the "diamond" resonance observed by DMRG calculations. (e) The arrow representation for the diamond resonance.

in Fig. 3.4a. A second-order term $\sigma^x_{12}\sigma^x_{24}$ can be transformed into a first-order one, $\pm\sigma^x_{25}$, by using Gauss's law (3.3). Because linear terms are forbidden, we conclude that $A^{(2)}_{12;24} = 0$.

By combining Gauss's law with lattice symmetries, we can rule out interactions between second neighbors (distance $\sqrt{3}/2$). In Fig. 3.4b, sites 2 and 5 carry opposite charges, hence $\sigma^x_{21}\sigma^x_{24}\sigma^x_{25} = -\sigma^x_{53}\sigma^x_{56}\sigma^x_{52}$, or $\sigma^x_{21}\sigma^x_{24} = -\sigma^x_{53}\sigma^x_{56}$. Since $\sigma^x = \pm 1$, we obtain $\sigma^x_{21}\sigma^x_{53} = -\sigma^x_{24}\sigma^x_{56}$. By lattice symmetry, $A^{(2)}_{21;53} = A^{(2)}_{24;56}$. The two second-neighbor terms cancel out:

$$A^{(2)}_{21;53}\sigma^x_{21}\sigma^x_{53} + A^{(2)}_{24;56}\sigma^x_{24}\sigma^x_{56} = A^{(2)}_{21;53}(\sigma^x_{21}\sigma^x_{53} + \sigma^x_{24}\sigma^x_{56}) = 0.$$

Thus there are no interactions between second-neighbor links and we may set $A^{(2)}_{21;53} = A^{(2)}_{24;56} = 0$.

The same line of argument shows that $A^{(2)}_{21;56} = A^{(2)}_{24;53} = 0$. This rules out a $\sigma^x\sigma^x$ term for links that are third neighbors (distance 1) residing on different hexagons of the honeycomb.

The closest non-vanishing interactions are between third neighbors (distance 1) residing on the same hexagon, e.g., links 24 and 35 in Fig. 3.4c. Adding these interactions takes us one step beyond the MSP model.

To determine the sign of the coupling constant between these third neighbors, we use input from numerical studies. The DMRG calculations have identified a strong valence-bond resonance in the diamond-shaped loop [20,21], which corresponds to the tunneling between two quasi-degenerate dimer coverings (Fig. 3.4d). Translating the two configurations into electric field (Fig. 3.4e), we see that electric fields on opposite sides of a hexagon tend to be opposite, which indicates a negative coupling between the electric field operators.

We have thus obtained a phenomenological IGT Hamiltonian describing the spin-liquid state of KHAF:

$$H = -\sum_{\alpha} F_\alpha + K \sum_{\text{3.n.}} \sigma^x_{ij}\sigma^x_{kl}. \tag{3.8}$$

Pairwise interactions of electric fields σ^x are limited to honeycomb links facing each other across a hexagon (Fig. 3.4c). Physical states satisfy Gauss-law constraints (3.3). $K > 0$.

3.3 Solving the model

In this section, we present the techniques needed for studying the new model. We first map the IGT (3.8) to a quantum Ising model through the standard duality transformation in Section 3.3.1. In Section 3.3.2 we construct an analytically solvable soft-spin version of the dual Ising model. In Section 3.3.3 we translate electric field in the honeycomb lattice to the density of dimers on kagome. The latter is directly related to the nearest-neighbor spin correlations in the $S = 1/2$ KHAF, connecting our phenomenological model to the DMRG results.

The dual Ising model is defined on a triangular lattice, whose sites are centers of honeycomb plaquettes, Fig. 3.5a. We label the sites of the triangular lattice by Greek indices $\alpha, \beta, \gamma \ldots$ As discussed in Section 2.7, the magnetic flux operators F_α are represented by Ising variables τ^x_α in the dual language. The product of electric field operators then becomes Ising coupling $\tau^z_\alpha \tau^z_\beta$ between third neighbors on the triangular lattice. The system thus consists of four entirely decoupled sublattices (A, B, C, and D in Fig. 3.5c) and behaves as four decoupled Ising models.

3.3.1 Duality transformation

Following the prescription laid down in Section 2.7, the electric field operator σ^x_{ij} is expressed in terms of dual Ising variables τ^z_α defined on hexagonal plaquettes:

$$\sigma^x_{ik} = \lambda_{\alpha\beta} \tau^z_\alpha \tau^z_\beta, \tag{3.9}$$

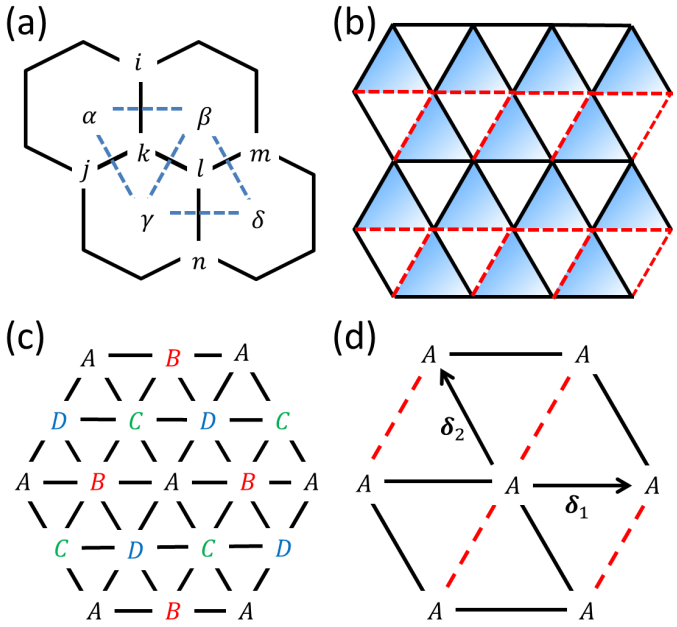

Figure 3.5: (a) The dual Ising variables are defined on the hexagonal plaquettes, and they form a triangular lattice (blue dashed lines). Latin (Greek) letters are labels of the sites in the honeycomb (triangular) lattice. (b) The constraints on the phase factors $\lambda_{\alpha\beta}$. The product of the $\lambda_{\alpha\beta}$ around the shaded (unshaded) triangles is -1 (1). A possible arrangements for $\lambda_{\alpha\beta}$ is that $\lambda_{\alpha\beta} = 1$ on black solid links and -1 on red dashed links. (c) The four sublattices of the triangular lattice. A, B, C, and D are labels of the sublattices. Sites in the same sublattice are connected by the third-neighbor interaction. (d) The exchange interaction between the spins in A sublattice. The interaction is K on black solid links and $-K$ on red dashed links. The primitive vectors $\delta_{1,2}$ are also shown.

where α and β are adjacent hexagonal plaquettes sharing honeycomb link $\langle ik \rangle$ (Fig. 3.5a). $\lambda_{\alpha\beta} = \pm 1$ is a phase factor to be defined below. The magnetic flux operator then is expressed as,

$$F_\alpha = \tau^x_\alpha. \tag{3.10}$$

To determine λ, we substitute Eq. 3.9 into Gauss's law (3.3) and find the following

condition on the fluxes of λ factors,

$$\lambda_{\alpha\beta}\lambda_{\beta\gamma}\lambda_{\gamma\alpha} = \begin{cases} +1 & \text{down triangle,} \\ -1 & \text{up triangle.} \end{cases}, \tag{3.11}$$

Fig.3.5b shows a solution of $\lambda_{\alpha\beta}$ satisfying Eq. 3.11.

Substituting Eq. 3.9 and Eq. 3.10 into Eq. 3.8, we obtain the dual Hamiltonian,

$$H = -\sum_{\alpha} \tau_{\alpha}^{x} + K \sum_{\langle\alpha,\beta\rangle\in 3.\text{n.}} \lambda_{\alpha\gamma}\lambda_{\gamma\beta}\tau_{\alpha}^{z}\tau_{\beta}^{z}. \tag{3.12}$$

The second summation is over third-neighbor dual spin pairs. γ is a triangular-lattice site located between third neighbors α and β. Since the interaction is only among third neighbors, the dual triangular lattice splits into four non-interacting sublattices A, B, C, and D (Fig. 3.5c). The Hamiltonian is further simplified,

$$H = H_A + H_B + H_C + H_D. \tag{3.13}$$

The Hamiltonian for the A-sublattice is given by

$$H_A = -h\sum_{\mathbf{r}\in A} \tau_{\mathbf{r}}^{x} + K\sum_{\mathbf{r}\in A} \tau_{\mathbf{r}}^{z}\tau_{\mathbf{r}+\delta_1}^{z} + K\sum_{\mathbf{r}\in A} \tau_{\mathbf{r}}^{z}\tau_{\mathbf{r}+\delta_2}^{z} - K\sum_{\mathbf{r}\in A} \tau_{\mathbf{r}}^{z}\tau_{\mathbf{r}+\delta_1+\delta_2}^{z}, \tag{3.14}$$

where $\delta_{1,2}$ are primitive vectors generating the A-sublattice (Fig. 3.5d). $H_{B,C,D}$ have the same form as H_A. Note H_A is unfrustrated because each triangle contains two antiferromagnetic links and one ferromagnetic link so that the interaction energy can be minimized simultaneously.

The decomposition of the system into four independent subsystems is a feature of the bilinear coupling of dual ising variables. A more detailed analysis shows that

the four subsystems cannot be coupled by quadratic coupling $\tau^z_{\mathbf{r}}\tau^z_{\mathbf{s}}$ without violating kagome lattice symmetry. However, they can be coupled by four-spin-interactions $\tau^z_{\mathbf{r}}\tau^z_{\mathbf{s}}\tau^z_{\mathbf{t}}\tau^z_{\mathbf{u}}$.

The dual Ising model possesses two phases at zero temperature. When $K \ll 1$, the dual Ising model Eq. 3.14 is in the paramagnetic phase, which corresponds to the spin liquid phase of the quantum dimer model on kagome. When $K \gg 1$, it is in the magnetic phase, which corresponds to the valence bond crystal phase of the quantum dimer model. We focus on the paramagnetic phase of the dual Ising model throughout this chapter.

3.3.2 Soft spin model

The dual Ising model Eq. 3.13 and Eq. 3.14 cannot be easily solved. We construct an analytically solvable soft spin model that is expected to work well deeply in the disordered phase of the dual Ising model [35]. The soft spin model can be regarded as a low energy description of the original dual Ising model. To begin with, we replace the dual Ising operator $\tau^z_{\mathbf{r}} = \pm 1$ by a real-valued operator $\phi_{\mathbf{r}}$, which is the coarse graining of the dual Ising operator. The interaction between dual Ising spins therefore becomes

$$K\sum_{\mathbf{r}\in A}(\phi_{\mathbf{r}}\phi_{\mathbf{r}+\delta_1} + \phi_{\mathbf{r}}\phi_{\mathbf{r}+\delta_2} - \phi_{\mathbf{r}}\phi_{\mathbf{r}+\delta_1+\delta_2}). \tag{3.15a}$$

The transverse field term $-\tau^x_{\mathbf{r}}$ brings quantum fluctuations to the dual Ising spin, so we add

$$\frac{1}{2}\sum_{\mathbf{r}\in A}\pi^2_{\mathbf{r}} + \frac{\Delta}{2}\sum_{\mathbf{r}\in A}\phi^2_{\mathbf{r}} \tag{3.15b}$$

to the Hamiltonian. $\pi_{\mathbf{r}}$ is the canonical momentum operator conjugate to $\phi_{\mathbf{r}}$. Here a mass term with $\Delta > 0$ is introduced to ensure the fluctuations of $\phi_{\mathbf{r}}$ are gapped.

Combining all the terms listed above, we obtain the soft spin Hamiltonian for the A-sublattice,

$$\begin{aligned} H^{\text{soft}}_A = &\frac{1}{2}\sum_{\mathbf{r}\in A}\pi^2_{\mathbf{r}} + \frac{\Delta}{2}\sum_{\mathbf{r}\in A}\phi^2_{\mathbf{r}} + K\sum_{\mathbf{r}\in A}\phi_{\mathbf{r}}\phi_{\mathbf{r}+\delta_\mathbf{1}} \\ &+ K\sum_{\mathbf{r}\in A}\phi_{\mathbf{r}}\phi_{\mathbf{r}+\delta_\mathbf{2}} - K\sum_{\mathbf{r}\in A}\phi_{\mathbf{r}}\phi_{\mathbf{r}+\delta_\mathbf{1}+\delta_\mathbf{2}} \end{aligned} \tag{3.16}$$

The soft spin Hamiltonian for sublattices B, C, and D are obtained in the same way. The total soft spin Hamiltonian is

$$H^{\text{soft}} = H^{\text{soft}}_A + H^{\text{soft}}_B + H^{\text{soft}}_C + H^{\text{soft}}_D. \tag{3.17}$$

3.3.3 Dimer density

The last piece of our construction is a formula relating the expectation value of electric field operators to the density of dimers on kagome. To start with, we consider an up triangle on kagome, which corresponds to an A site in the honeycomb lattice (Fig. 3.6a). The case for a down triangle or a B site is obtained by the same token.

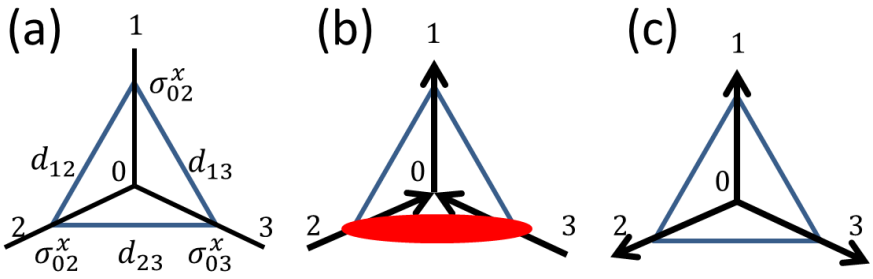

Figure 3.6: (a) An up-triangle on kagome. σ^x_{01}, σ^x_{02}, and σ^x_{03} are electric field operators on the links of the honeycomb lattice. d_{12}, d_{13}, and d_{23} are the dimer density modulation on the links of kagome. (b) A triangle occupied by a dimer. (c) An empty triangle.

The dimer density modulation on kagome link $\langle ij \rangle$, d_{ij}, is defined as the dimer density on the said link minus the average number of dimers per link, 1/4.

We postulate the following ansätz relation between the dimer density modulation and the expectation value of electric field operators on symmetry ground (Fig. 3.6a),

$$d_{23} = u\langle \sigma^x_{01} \rangle + v(\langle \sigma^x_{02} \rangle + \langle \sigma^x_{03} \rangle), \tag{3.18}$$

where u, v are coefficients to be determined. The expressions for d_{12} and d_{13} are obtained by 120° rotations around the center of the triangle.

We consider the case in which one side of the triangle is occupied by a dimer and the corresponding arrow configuration (Fig. 3.6b). On the one hand, the dimer density modulations are given by,

$$d_{12} = -\frac{1}{4}; \quad d_{13} = -\frac{1}{4}; \quad d_{23} = \frac{3}{4}. \tag{3.19}$$

On the other hand, the expectation values of the electric field operators are given by

$$\langle \sigma^x_{01} \rangle = 1; \quad \langle \sigma^x_{02} \rangle = -1; \quad \langle \sigma^x_{03} \rangle = -1. \tag{3.20}$$

The postulated relation Eq. 3.18 is consistent with the above if and only if,

$$u = \frac{1}{4}; \quad v = -\frac{1}{4}. \tag{3.21}$$

Therefore, we obtain the following relation:

$$d_{23} = \frac{1}{4}(\langle\sigma^x_{01}\rangle - \langle\sigma^x_{02}\rangle - \langle\sigma^x_{03}\rangle). \tag{3.22}$$

The self-consistency of Eq. 3.22 can be further examined by considering a triangle with no dimer shown in Fig. 3.6c, where $d_{12} = d_{13} = d_{23} = -1/4$, and $\langle\sigma^x_{01}\rangle = \langle\sigma^x_{02}\rangle = \langle\sigma^x_{03}\rangle = 1$. It can be seen that Eq. 3.22 holds in this special case as well.

3.4 Ground state of kagome cylinders

In Sections 3.2 and 3.3, we have constructed a phenomenological Ising gauge theory and developed necessary techniques to solve it deeply in the deconfined phase. In the ensuing sections, we compare predictions of our model with the DMRG results in various settings.

Most of the recent DMRG studies on $S = 1/2$ kagome Heisenberg antiferromagnet are performed with cylindrical geometry. Periodic boundary conditions are imposed in one direction of the lattice and open boundary condition in the other direction, making the system effectively a cylinder. The circumference of the cylinder is usually much smaller than the length, and we shall assume the length is infinite in the following discussion.

A kagome cylinder can be regarded as a one-dimensional system, and the unit cell is defined as the smallest building block that generates the whole cylinder by translation in the length direction. The DMRG studies have found that the ground state of Eq. 3.1 strongly depends on the number of spins in a unit cell [20]. When there are even number of spins per unit cell (dubbed "even cylinders" in later discussion), the ground state is a uniform spin liquid. When the number is odd ("odd cylinders"), the spin-liquid ground state coexists with a valence-bond density wave pattern, which breaks the spatial symmetries of the cylinder. This behavior is consistent with the Lieb-Schultz-Mattis theorem [36].

Motivated by the DMRG findings, we study our phenomenological model on three families of cylinders in this section. In all of the cases studied, we find good agreement between the phenomenological model and the DMRG.

3.4.1 Even cylinders

To start with, we consider so-called "YC4m" cylinders, where $m \in Z$ and the number $4m$ denotes the circumference of the tube [20]. Note that the number of spins per unit cell is $6m$, which is even. Fig. 3.7a shows a YC8 cylinder. We shall use the YC8 cylinder as an illustrative example in the following discussion, and all the results can be easily generalized to all YC4m cylinders.

The corresponding IGT model is defined on the honeycomb with "armchair" type periodic boundary condition (Fig. 3.7c). Note that the honeycomb cylinder is un-

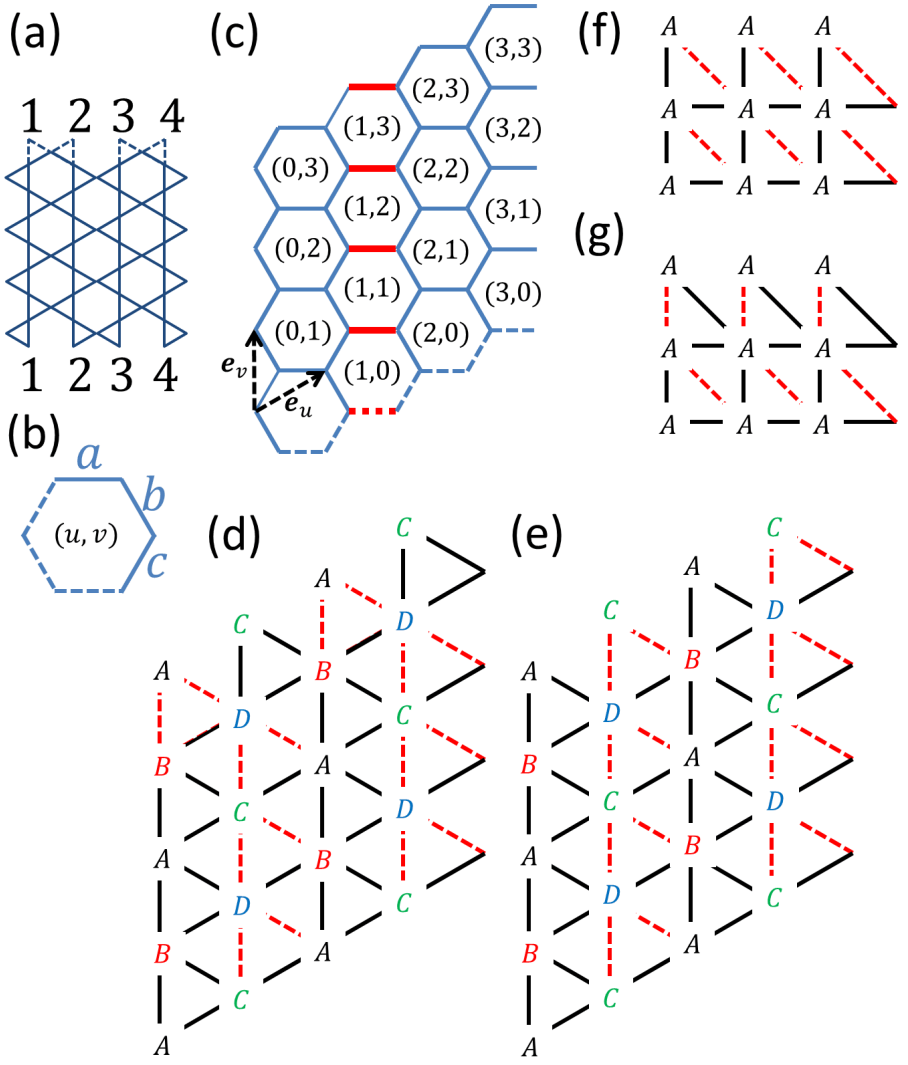

Figure 3.7: (a) The YC8 cylinder. The periodic boundary condition is imposed along the vertical direction. Sites with the same number are identical. (b) The labeling system employed in the main text. (c) The corresponding IGT model on honeycomb. Arrows are the primitive vectors $\mathbf{e}_u$ and $\mathbf{e}_v$ of the dual triangular lattices. The coordinates of the dual triangular sites are shown. (d) The dual model for YC8 cylinder in the even sector. The phase factor $\lambda = 1(-1)$ on black solid (red dashed) links. (e) The same dual model in the odd sector. (f) The exchange interaction between dual spins in A sublattice in the even sector. The interaction is K on black solid links and $-K$ on red dashed links. (g) The exchange interaction between dual spins in A sublattice in the odd sector.

folded in a way different from Fig. 3.7a.

We introduce a labeling system that will be employed in later discussions. The honeycomb plaquettes are generated by primitive vectors $\mathbf{e}_u$ and $\mathbf{e}_v$. The position vector of a honeycomb plaquette (or a dual triangular site) is uniquely expressed as $u\mathbf{e}_u + v\mathbf{e}_v$, and it is labeled as (u, v). Then, the three honeycomb links adjacent to the said plaquette are labeled as (u, v, a), (u, v, b), and (u, v, c) (Fig. 3.7b).

As discussed in Section 2.5, IGT exhibits topological degeneracy when non-contractible loops are present. In cylinder, there is one non-contractible closed path, and therefore there are two topological sectors. We define the electric loop operator,

$$X = \prod_v \sigma^x_{1,v,a}. \tag{3.23}$$

where the product is over the R-legs of the non-contractible closed path highlighted as thick red links in Fig. 3.7c. From our discussion in [somewhere], X is a good quantum number, $[X, H] = 0$. $X = 1$ and -1 in the even and odd topological sector, respectively.

The dual Ising model is defined on triangular lattice with cylindrical geometry (Figs. 3.7d,e). The electric loop operator X gives rise to new constraints on the phase factors $\lambda_{\alpha\beta}$ in addition to Eq. 3.11. Substituting Eq. 3.9 into Eq. 3.23, we rewrite X in terms of dual variables (Fig.3.7b):

$$X = \prod_v \lambda_{(1,v),(1,v+1)} = \pm 1 \tag{3.24}$$

Thus, the electric loop operator X is dual to the total flux of $\lambda_{\alpha\beta}$ around the cylinder

circumference.

In what follows, we treat the even ($X = 1$) and odd ($X = -1$) sectors separately. We consider the even sector at first. A choice of $\lambda_{\alpha\beta}$ satisfying conditions Eq. 3.11 and Eq. 3.24 is shown in Fig. 3.7c. We see that the dual model is decomposed into four independent copies of unfrustrated quantum Ising model, corresponding to four sublattices of the triangular lattice. In the disordered phase of the dual model, or equivalently the deconfined phase of the IGT,

$$\langle \sigma^x_{ij} \rangle = \lambda_{\alpha\beta} \langle \tau^z_\alpha \tau^z_\beta \rangle = \lambda_{\alpha\beta} \langle \tau^z_\alpha \rangle \langle \tau^z_\beta \rangle = 0. \tag{3.25}$$

The second equality follows from the fact that dual spins α and β, being nearest neighbors to each other, must belong to two different sublattices. The third equation follows from the assumption that the dual model is in the disordered phase. Given the modulation of dimer density is proportional to $\langle \sigma^x_{ij} \rangle$, we deduce that the ground state is uniform for YC4m cylinders in the even sector.

We proceed to calculate the ground state energy of the YC4m cylinder in the even sector. The circumference of each sublattice is m. The soft spin model for the A sublattice is given by (Fig. 3.7f)

$$\begin{aligned} H^{\text{soft}}_A = \frac{1}{2} \sum_{(u,v)\in A} \pi^2_{u,v} + \frac{\Delta}{2} \sum_{(u,v)\in A} \phi^2_{u,v} + K \sum_{u,v} (\phi_{u,v}\phi_{u+2,v} \\ + \phi_{u,v}\phi_{u,v+2} - \phi_{u,v}\phi_{u-2,v+2}), \end{aligned} \tag{3.26}$$

Here the periodic boundary condition $\phi_{u,v} = \phi_{u,v+2m}$ is imposed. The above Hamiltonian can be readily diagonalized. The ground state energy per dual site is given

by

$$\epsilon_1(m) = \frac{1}{2m}\sum_{v=0}^{m-1}\int_0^{2\pi}\frac{dk_u}{2\pi}\omega\left(k_u, \frac{2\pi v}{m}\right), \tag{3.27}$$

where

$$\omega = \sqrt{\Delta + 2K[\cos k_u + \cos k_v - \cos(k_u - k_v)]} \tag{3.28}$$

is the dispersion relation of soft spin fluctuations.

The analysis on the dual Ising model in the odd sector can be carried out in the similar manner. A choice of $\lambda_{\alpha\beta}$ is shown in Fig. 3.7e. Similar to the even sector, the dual triangular lattice is decomposed into four independent, identical sublattices. The ground state is uniform in the odd sector as well.

As shown in Fig. 3.7g, the explicit translational invariance of the sublattice Hamiltonian is lost in the circumference direction. However, we can make a gauge transformation $\phi_{u,2m} \rightarrow -\phi_{u,2m}$ to restore the translational invariance. The soft spin model becomes identical to Eq. 3.26. The boundary condition, however, becomes anti-periodic: $\phi_{u,v} = -\phi_{u,v+2m}$. The ground state energy per site is given by

$$\epsilon_{-1}(m) = \frac{1}{2m}\sum_{v=0}^{m-1}\int_0^{2\pi}\frac{dk_u}{2\pi}\omega\left(k_u, \frac{(2v+1)\pi}{m}\right), \tag{3.29}$$

Here ω is the same as Eq. 3.28.

Fig.3.8 shows the ground state energy per dual site as a function of cylinder circumference for generic values of Δ and K, based on numerical evaluation of Eq. 3.27 and Eq. 3.29. We find that the ground state energy in the two sectors becomes degenerate in the thermodynamical limit as expected for IGT. When the circumference

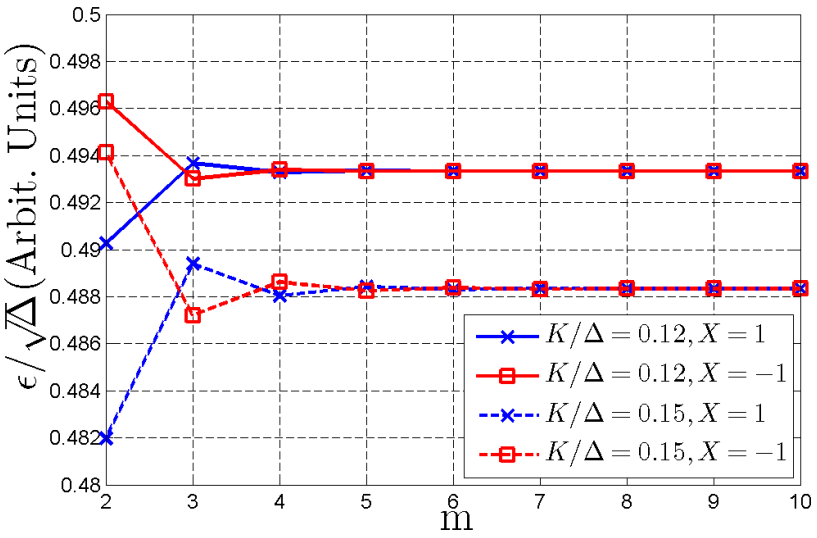

Figure 3.8: Ground state energy per site ϵ of YC4m cylinder in even $X = 1$ (blue crosses) and odd $X = -1$ sectors (red open circles). The solid and dashed lines correspond to $K/\Delta = 0.12$ and $K/\Delta = 0.15$, respectively.

is finite, the energy splitting shows an alternating pattern: the even ground state has lower energy when m is even, and the odd ground state has lower energy otherwise. Such a pattern plays an important role in our discussion on edge spinons in Section 3.6.

To summarize, we have found that the ground state of the YC4m cylinder is a uniform spin liquid. The ground state lies in the even sector $X = 1$ for even m, and the odd sector $X = -1$ for odd m.

3.4.2 Odd cylinders

In this section, we discuss another family of kagome cylinders known as YC4$m+2$, $m \in Z$ [20]. The number of spins per unit cell is $6m + 3$, which is odd. Based on

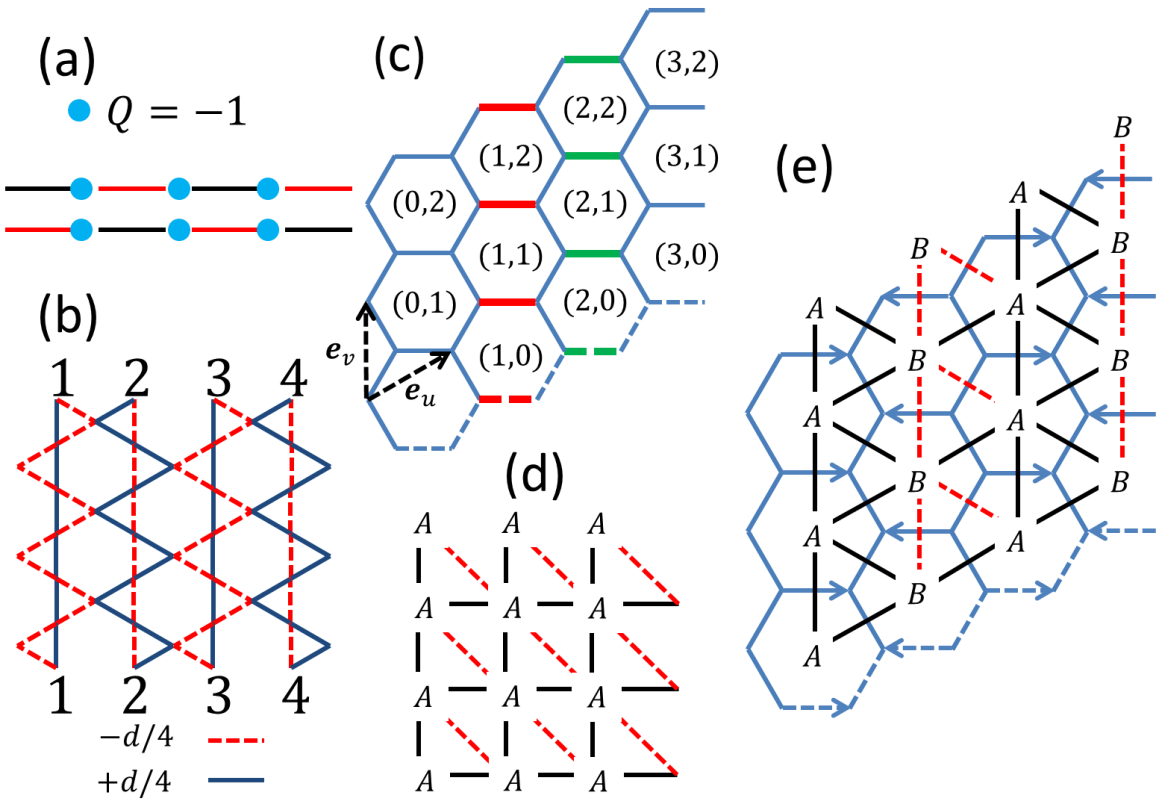

Figure 3.9: (a) An IGT in 1D with static background charge $Q = -1$. The ground states break translational symmetry due to Gauss's law. Electric field $\sigma^x = 1$ on black links and -1 on red links. (b) A YC6 cylinder and the predicted valence-bond density modulation pattern. Lattice sites with the same numeral label are identical. (c) The corresponding IGT. (d) The dual Ising model. A and B are sublattice labels. $\lambda = 1(-1)$ on black solid (red dashed) links. (e) The interaction between A dual spins. The interaction is $K(-K)$ on black solid (red dashed) links.

the Lieb-Schultz-Mattis theorem, we expect that the ground state is either gapless or symmetry-breaking. Indeed, DMRG has identified a symmetry-breaking valence-bond density wave pattern. We will show that our model reproduces this exact pattern in the ground state.

As a concrete example, we consider the YC6 cylinder, a member of the YC$4m+2$ family, in the following discussion. The analysis is carried on along the line of Section

3.4.1. Fig. 3.9b shows the YC6 kagome cylinder, and Fig. 3.9c shows its corresponding honeycomb cylinder on which the IGT is defined.

In the dual honeycomb cylinder, there are 3 A sites and 3 B sites. Therefore, the total charge in the unit cell is -1 from Eq. 3.3. It has significant impact on the ground state of IGT. To see this, we first consider a toy model: a one dimensional IGT with $Q = -1$ background charge per site (Fig. 3.9a). A moment of thought shows that the electric fields must be alternating to fulfill the Gauss's law, and therefore the ground states must break the translational symmetry.

Now we put the above observation on a formal ground. To this end, we define the electric loop operator as,

$$X = \prod_v \sigma^x_{1,v,a}, \tag{3.30}$$

The product is over the R-legs highlighted as the thick red links in Fig. 3.9a. Again, the Hilbert space falls into two topological sectors, $X = 1$ (even) and $X = -1$ (odd).

The two topological sectors are related by translational symmetry. To see this, we consider another electric loop operator shown as the thick green links in Fig. 3.9c, which is:

$$X' = \prod_v \sigma^x_{2,v,a}. \tag{3.31}$$

On the one hand, it can be seen that $X' = -X$ on account of Gauss's law (3.3). On the other hand, the new closed path is related to the old one by a $\mathbf{e}_u$ shift, and we have

$T(\mathbf{e}_u)XT(\mathbf{e}_u)^\dagger = X'$. Here $T(\mathbf{e}_u)$ denotes the associated shift operator. Therefore,

$$T(\mathbf{e}_u)X = -XT(\mathbf{e}_u). \tag{3.32}$$

Eq. 3.32 implies that the two topological sectors are degenerate in energy in the YC6 cylinder, even though the circumference being finite. Note $T(\mathbf{e}_u)$ is a symmetry,

$$[T(\mathbf{e}_u),\, H] = 0. \tag{3.33}$$

Let $|\psi\rangle$ be a common eigenstate of the Hamiltonian H and the electric loop operator X:

$$H|\psi\rangle = \epsilon|\psi\rangle, \quad X|\psi\rangle = x|\psi\rangle. \tag{3.34}$$

Then,

$$\begin{aligned} HT(\mathbf{e}_u)|\psi\rangle &= T(\mathbf{e}_u)H|\psi\rangle = \epsilon T(\mathbf{e}_u)|\psi\rangle, \\ XT(\mathbf{e}_u)|\psi\rangle &= -T(\mathbf{e}_u)X|\psi\rangle = -xT(\mathbf{e}_u)|\psi\rangle. \end{aligned} \tag{3.35}$$

We see $|\psi\rangle$ and $T(\mathbf{e}_u)|\psi\rangle$ are degenerate in energy yet belong to two different topological sectors. Therefore, the energy spectra in the two topological sectors coincide, and the degenerate eigenstates are related by the $\mathbf{e}_u$ translation. Most importantly, in contrast to the YC4m cylinders, the ground states in the two topological sectors of the YC4$m+2$ cylinders are exactly degenerate, and they break the translation symmetry in $\mathbf{e}_u$ direction.

We proceed to discuss the dual soft spin model. We shall consider the even sector only (Fig. 3.9d). The circumference of the dual triangular lattice is $2m+1$, making

it impossible to partition the lattice into four independent sublattices. Consequently, there are only two independent sublattices, labeled as A and B. The Hamiltonians for both sublattices are identical. The soft spin model for the A sublattice is given by (Fig. 3.9e):

$$H_A^{\text{soft}} = \frac{1}{2}\sum_{(u,v)\in A}\pi_{u,v}^2 + \frac{\Delta}{2}\sum_{u,v}\phi_{u,v}^2 + K\sum_{u,v}(\phi_{u,v}\phi_{u+2,v} + \phi_{u,v}\phi_{u,v+2} - \phi_{x,y}\phi_{u-2,v+2}), \tag{3.36}$$

The periodic boundary condition $\phi_{u,0} = \phi_{u,2m+1}$ is imposed.

We have deduced on symmetry ground that the ground state in the even sector must break the translational symmetry. In what follows, we show that the translation symmetry is broken by a dimer-density modulation pattern. To this end, we calculate the expectation value of electric field operator in the ground state. For the (u, v, b) links,

$$\begin{aligned}\langle\sigma_{u,v,b}^x\rangle &= \lambda_{(u,v),(u+1,v)}\langle\tau_{u,v}^z\tau_{u+1,v}^z\rangle \\ &= \lambda_{(u,v),(u+1,v)}\langle\tau_{u,v}^z\rangle\langle\tau_{u+1,v}^z\rangle = 0.\end{aligned} \tag{3.37}$$

The second equality follows from the fact that the dual sites (u, v) and $(u + 1, v)$ belong to different sublattices and therefore are uncorrelated (Fig. 3.9d). The third equality follows from the assumption that the dual model is in the disordered phase. By the same token,

$$\langle\sigma_{u,v,c}^x\rangle = 0. \tag{3.38}$$

The expectation value of $\sigma^x_{u,v,a}$ does not vanish in the ground state.

$$\langle \sigma^x_{u,v,a} \rangle \approx \lambda_{(u,v),(u,v+1)} \langle \phi_{u,v} \phi_{u,v+1} \rangle = \begin{cases} +d & \text{if } u = 0 \bmod 2, \\ -d & \text{if } u = 1 \bmod 2. \end{cases} \tag{3.39}$$

Here $d \neq 0$ in general because the dual sites (u, v) and $(u, v+1)$ belong to the same sublattice (Fig. 3.9d). The plus and minus signs come from the λ phase factor. We have defined $d \equiv \langle \phi_{u,v} \phi_{u,v+1} \rangle$, where d doesn't depend on u, v thanks to the translational invariance of the sublattice Hamiltonian and the fact that the Hamiltonians for A and B sublattices are identical.

Combing Eq. 3.37, Eq. 3.38, and Eq. 3.39, we conclude that the IGT displays an alternating electric-field pattern in the ground state on the YC4$m+2$ cylinders. The pattern in the even sector is shown in Fig. 3.9d as arrows. The pattern in the odd sector is obtained by a $\mathbf{e}_u$ shift, or equivalently by reversing all the arrows.

The electric field operator is tied to dimer density. We can therefore determine the dimer density modulation in the ground state of YC4$m+2$ cylinders by using the results in Section 3.3.3. The dimer modulation pattern is shown in Fig. 3.9b. (The pattern in the other sector is obtained by a shift of $\mathbf{e}_u$.) The blue solid and red dashed links stand for dimer density modulation of $d/4$ and $-d/4$ respectively. In terms of the Heisenberg model, they correspond to stronger and weaker nearest-neighbor spin-spin correlation. The pattern shown in Fig. 3.9e agrees well with the DMRG result.

The value of d can be explicitly calculated by using the soft spin model. We

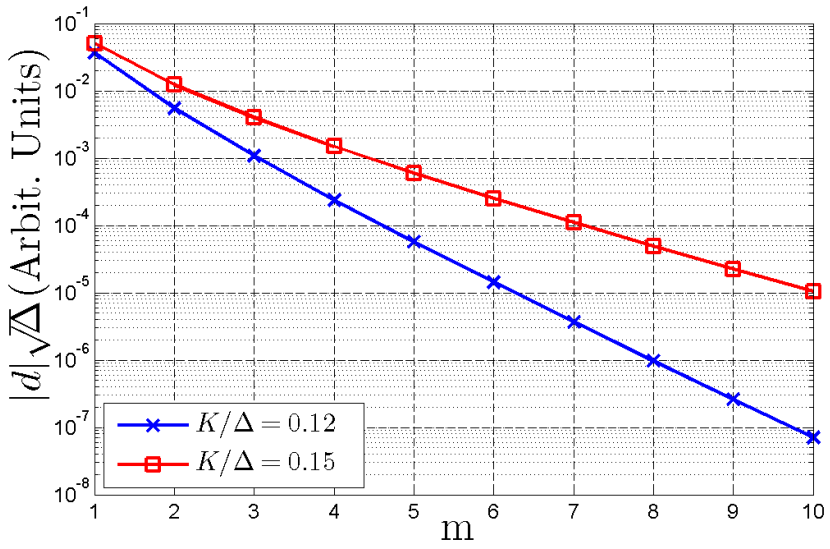

Figure 3.10: Dimer density modulation amplitude $|d|$ in the ground states of YC4m+2 cylinders as a function of the cylinder index m.

obtain,

$$d = \frac{1}{2(2m+1)} \sum_{v=0}^{2m} \int_0^{2\pi} \frac{dk_u}{2\pi} \frac{\cos[2\pi v/(2m+1)]}{\omega[k_u, 2\pi v/(2m+1)]}, \tag{3.40}$$

where

$$\omega = \sqrt{\Delta + 2K[\cos k_u + \cos 2k_v - \cos(k_u + 2k_v)]}. \tag{3.41}$$

Fig. 3.10 shows the absolute value of d as a function of cylinder index m for generic value of model parameters. We can see that $|d|$ decreases almost exponentially as m increases, reflecting the finite correlation length in the ground state.

To sum up, we have found that the ground states of the YC4$m+2$ cylinders are two-fold degenerate. The ground states display a symmetry-breaking valence-bond modulation pattern, which agrees with what found by DMRG.

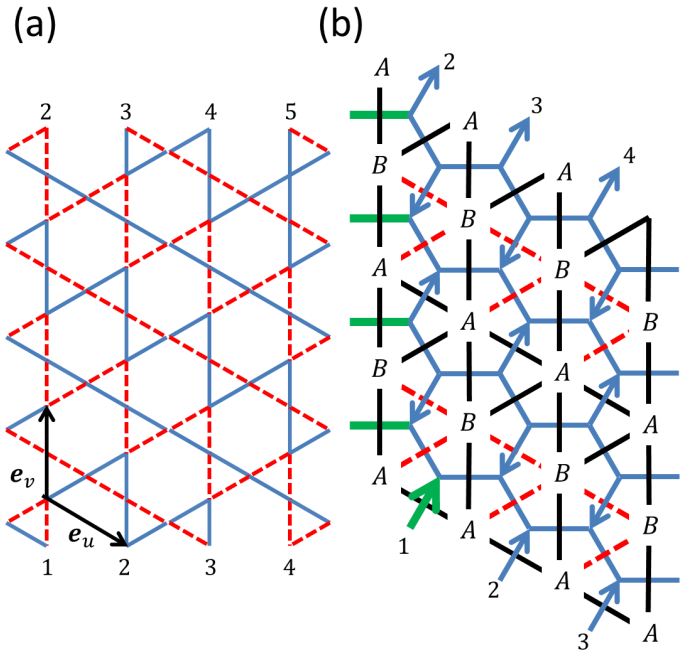

Figure 3.11: (a) Valence-bond modulation pattern on the YC9-2 cylinder calculated from the phenomenological theory. The spin-spin correlation is enhanced on the solid blue links and weakened on the dashed red links, respectively. Sites labeled with the same number are identical. (b) The corresponding gauge theory model and the dual Ising model. Arrows indicate the non-vanishing expectation value of σ^x_{ij} in the ground state. Boundary links labeled with the same number are identical. Thick green links highlight the contour with respect to which the total electric loop operator X is defined. A and B stand for two independent sublattice sites of the dual lattice. The phase factor $\lambda = 1(-1)$ on black solid (red dashed) links. Here the even sector $X = 1$ is shown.

3.4.3 Chiral cylinders

In this section, we briefly discuss one more family of kagome cylinders dubbed as YC$(4m + 1)$-2 [20]. This new family of cylinders lacks for the reflection symmetry along the circumference direction. The DMRG calculation has identified an valence-bond modulation pattern similar to the one found in the YC$4m + 2$ family but with a different orientation. The analysis on YC$(4m + 1)$-2 cylinders can be carried out in

the same manner as in Section 3.4.2, and therefore we simply summarize the result.

Fig. 3.11a shows a YC9-2 cyliner, a member of the YC($4m+1$)-2 family. Note that the periodic boundary condition along the circumference direction of cylinder is accompanied by a shift in the length direction. Fig. 3.11b shows the corresponding gauge theory model and the dual Ising model. The topological sectors are defined with respect to the electric loop operator highlighted as the thick green links. Similar to the YC$4m+2$ cylinders, the energy spectra in both sectors are exactly identical. In particular, the ground states are two-fold degenerate and break the translation symmetry along the $\mathbf{e}_v$ direction. Here the expectation value of σ^x_{ij} in the even-sector ground state is shown as arrows, from which we determine the valence-bond modulation pattern (Fig. 3.11a). The pattern in the other ground state is obtained by a $\mathbf{e}_v$ translation.

Comparing the calculated pattern with the one obtained by DMRG, we find that the two agree qualitatively. However, the pattern predicted by our phenomenological theory is perfectly uniform along the $\mathbf{e}_u$ direction, whereas the DMRG pattern shows another, weaker, modulation along the $\mathbf{e}_u$ direction. This discrepancy may be due to the shorter-range physics that is not included in our theory.

3.5 Singlet-pinning effects

In the previous section, we studied the ground states of kagome cylinders. In this section, we study the response of the spin liquid ground state to an externally-pinned singlet. Specifically, when the Heisenberg exchange interaction J on a link is enhanced by δJ, it is energetically favorable to form a spin singlet on that link (Fig. 3.12a). The pinned singlet freezes the resonating singlets nearby, and a modulation pattern of nearest-neighbor spin-spin correlation $\langle \mathbf{S}_i \cdot \mathbf{S}_j \rangle$ appears in its neighborhood. When $\delta J \ll 1$, the pattern coincides with the dimer-dimer correlation in the unperturbed ground state. The goal of this section is to compute such a modulation pattern by using the phenomenological model and to compare it with the numerical results.

The effects of an enhanced link in the Heisenberg model are effectively described by an dimer-attracting potential in the quantum dimer model, which is amount to introducing favored arrow orientations in the arrow representation (Fig. 3.12b). The Ising gauge theory Hamiltonian is given by

$$H = H_0 - V(\sigma^x_{0,0,a} - \sigma^x_{0,0,b} - \sigma^x_{0,1,c}), \tag{3.42}$$

where H_0 is the unperturbed Hamiltonian and V is the strength of the pinning potential. The above Hamiltonian is readily solved by using the duality mapping and the soft spin approximation.

Fig. 3.12c shows the calculated dimer density modulation pattern on the YC8 cylinder by solving Eq. 3.42 for $\Delta = 1$, $K = 0.15$, and $V = 0.2$. Note that the

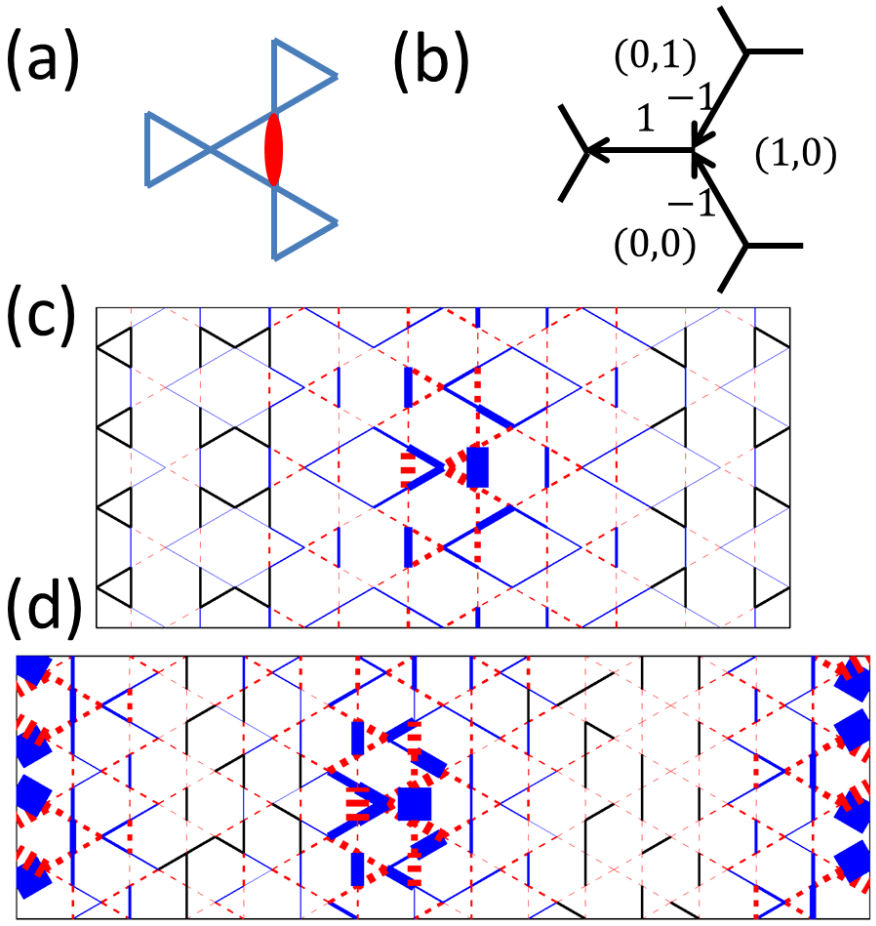

Figure 3.12: (a) A singlet or dimer is pinned on a link with enhanced Heisenberg exchange interaction. (b) A pinned dimer is amount to frozen arrows in the arrow representation. (c) The dimer density modulation pattern on YC8 cylinder calculated from the phenomenological theory. We choose $\Delta = 1$, $K = 0.15$, and $V = 0.2$. The dimer density is increased on blue solid links and decreased on red dashed links. The thickness is proportional to the magnitude of modulation. (d) Nearest-neighbor spin-spin correlations $\langle \mathbf{S}_i \cdot \mathbf{S}_j \rangle$ from DMRG calculation on the Heisenberg model. Reproduced with permission from [34]. The correlation is increased on blue solid links and decreased on red dashed links. The thickness is proportional to the magnitude of modulation. The exchange energy is increased by 10% on the center link, which shows the largest enhancement of correlation.

unperturbed ground state ($V = 0$) of the YC8 cylinder is uniform as discussed in Section.3.4.1. The perturbed Hamiltonian is solved in the even sector, where the ground state of the YC8 cylinder lies (Fig.3.8). The dimer density is increased on the blue solid links and decreased on the red dashed links. The link thickness is proportional to the magnitude of modulation. The link with enhanced exchange interaction has the largest dimer density.

We find qualitative agreement between the phenomenological theory and the DMRG (Fig. 3.12d). In addition, we note the following features of the modulation pattern calculated from the phenomenological theory. Firstly, the spatial modulation quickly decays as the distance to the enhanced link increases, which is another manifestation of the gapped nature of the ground state. Secondly, there are alternatively enhanced and reduced diamond shapes which tile the whole cylinder, highlighted as plus and minus signs in Fig.3.12c. These diamond shapes coincide with the so-called "diamond resonance" observed by DMRG and Lanczos diagonalization studies [37].

3.6 Edge spinons and screening

In previous discussion, we assumed that the kagome cylinders are infinite in the length direction. As we shall see below, open boundaries give rise to a new phenomenon: in certain circumstances, an open boundary can bind a spinon. These edge spinons are detectable in numerical simulation, which could serve as a direct evidence

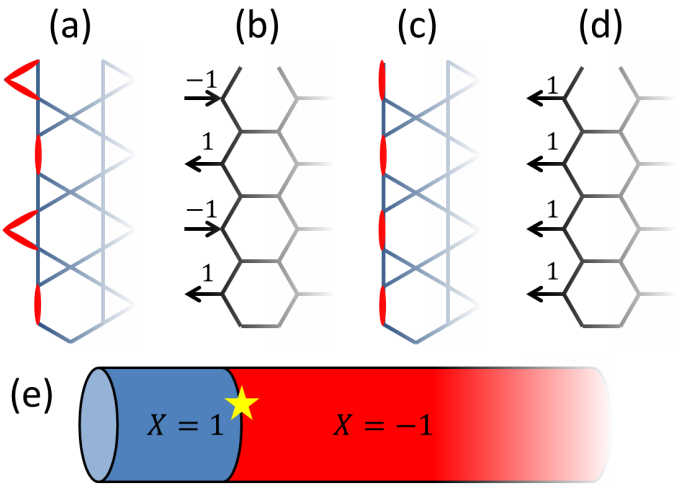

Figure 3.13: (a) The open boundary of YC4m cylinders employed by Yan et al. The singlets are pinned at the boundary. (b) The arrow representation for the frozen dimer covering shown in (a). The numbers ± 1 are the electric fields on the dangling links. (c) Another open boundary condition of YC4m cylinders and the pinned singlets. (d) The arrow representation and the electric fields corresponding to the frozen dimer covering shown in (c). (e) The electric field in the bulk is screened by a spinon.

for fractionalization.

To start with, we consider a particular type of open boundary of YC4m cylinders, which is employed by Yan et al (Fig. 3.13a). The motivation is to make the open boundary compatible with the "diamond resonance" pattern. It is energetically favorable to form singlets on dangling links, and therefore a particular dimer covering is pinned at the boundary, which has been observed in DMRG calculations.

The physical meaning of such an open boundary condition becomes transparent in the IGT description. Converting the frozen dimer covering to arrow representation, we find that the effect of the open boundary is to enforce an alternating electric field pattern at the edge (Fig. 3.13b). The electric loop operator X takes value $(-1)^m$

in the YC4m cylinder. As discussed in Section 3.4.1, the electric loop operator in the ground state of YC4m cylinder is $(-1)^m$. Comparing the value of electric loop operator X enforced by the open boundary condition with the one selected by the bulk energetics, we find that the two match for any m.

However, the agreement can be lost if one chooses other types of open boundary. An example is shown in Fig. 3.13c. Similarly, dimers are pinned at the boundary, and an electric field pattern is enforced at the edge (Fig. 3.13d). The electric loop operator X at the edge is always 1 for any YC4m cylinder. When m is odd, the electric loop operator on the edge and the one in the bulk don't match.

The mismatching is resolved by a spinon screening the bulk electric field in the ground state of YC4m cylinder when m is odd, which is in close analogy to the screening phenomenon in a metal (Fig. 3.13e). Close to the edge, the $X = 1$, and the cylinder segment between the edge and the spinon is in the even sector. Deep into the bulk, the $X = -1$, and the bulk is in the odd sector. Assuming that the distance between the edge and the spinon is x, the total energy of the system is approximately given by:

$$E \approx [e_1(m) - e_{-1}(m)]x + \text{const.} \quad (m\,\text{odd}). \tag{3.43}$$

Here $e_1(m)$ and $e_{-1}(m)$ are energy per unit length in the even and odd sectors of the YC4m cylinder. Note that $e_1 > e_{-1}$ when m is odd. Therefore, the spinon is confined to the edge by a linear potential [38].

Finally, we remark that, as the two topological sectors in YC4$m+2$ cylinders are

exactly degenerate, there are no edge spinons in generic conditions.

3.7 Discussion

We close this chapter by placing our work in the context of previous theoretical efforts. As we have shown in Section 3.2, the hard core constraints of dimers naturally endow the kagome quantum dimer model a Ising gauge theory structure. The emergent $U(1)$ gauge symmetry was first recognized by Rokhsar and Kivelson in quantum dimer model on square lattice [28]. The $U(1)$ gauge symmetry was utilized by Fradkin and Kivelson to formulate an effective field theory for quantum dimer model on square lattice [39, 40].

Moessner *et al* studied the quantum dimer model on triangular lattice [41, 42]. They realized that this model can be mapped to an Ising gauge theory. In their framework, the dimer occupation number on each triangular link is identical to the Ising electric flux on that link. The dimer hard-core constraints are approximately enforced by Gauss's law and the energetics. The effective Ising gauge theory is therefore a theory on triangular lattice with charge $Q = -1$ on every site. The mapping was also used to explain several features of the spin liquid state in J_1-J_2 Heisenberg model on square lattice [35].

Earlier workers on kagome quantum dimer model employed the same mapping [12, 43, 44]. The quantum dimer model was mapped onto an Ising gauge theory on the

same lattice. Despite the superficial differences, our framework and the one employed in earlier works are quite similar. In the previously used framework, visons are defined on both triangular and hexagonal plaquettes of kagome. A vison is associated with quantum tunneling of dimer coverings in a plaquette. However, dimer coverings on a triangular plaquette cannot tunnel as they are eigenstates of the local interactions, and thus it is natural to treat the visons on triangular plaquettes as high energy degrees of freedom and integrate them out. The resulting theory should be the same as ours. Our approach thus provides a more economical representation of the quantum dimer model on kagome.

The similarity between the two frameworks becomes more evident in the dual formulation. The dual Landau-Ginzburg order parameter in [44] has four independent real components ϕ_i, which precisely correspond to the four sublattices in our formulation described in Section 3.3.1.

We also note that a similar work by Ju and Balents, who adapted the earlier framework [45]. They computed the dimer modulations in cylinders with various boundary conditions and obtained results in agreement with ours.

Chapter 4

Quantum spin ice

In the previous chapter, we discussed the spin liquid in kagome Heisenberg antiferromagnet with focus on fractionalization. In this chapter, we discuss another frustrated magnet known as quantum spin ice. We will emphasize the confinement phenomenon in quantum spin ice.

Classical spin ice is a frustrated ferromagnet [46]. In its ground state, magnetization satisfies a zero-divergence constraint leading to an effective cancellation of the internal magnetic field [46]. Spinon excitations violate this constraint and thus behave as mobile magnetic charges [47,48]. When spinons are confined by an external magnetic field, elementary excitations are strings connecting a pair of spinons with opposite magnetic charges [49]. In classical spin ice, spinons and strings are classical objects; their dynamics are entirely due to thermal fluctuations.

In quantum spin ice, spins show substantial quantum fluctuations, which may

produce qualitatively new physics [50–53]. We demonstrate that, in a certain regime of coupling constants, elementary excitations of quantum spin ice are strings with inherent quantum dynamics. The calculated dynamical structure factor $S(\omega, \mathbf{k})$ reveals multiple branches of excitations that correspond, loosely speaking, to strings of different lengths and shapes. As the applied field increases, these branches gradually separate and the lowest one evolves into a magnon. Our results have been previously published in [54].

The current chapter is organized as follows. In Section 4.1, we discuss the spinons and strings in classical spin ice. In Section 4.2, we describe a toy model for strings in quantum spin ice in two dimension. In Section 4.3, we discuss quantum strings in three dimensions and connect it to real quantum spin ice materials. In Section 4.4, we study shape fluctuations of strings and the deconfinement transition of spinons. Finally, we connect these results to the physics of gauge theories in Section 4.5.

4.1 Classical spin ice

The spins in a classical spin ice reside on the sites of pyrochlore lattice, which is a network of corner-sharing tetrahedra (Fig. 4.1a). There are four inequivalent lattice sites, labeled 0 through 3, each forming an FCC lattice. The tetrahedra also fall into two inequivalent types, up and down. Each site is shared by one up tetrahedron and one down tetrahedron. There is 3-fold rotational symmetry with respect to the axis

that passes through the centers of these two tetrahedra.

To facilitate our description of the pyrochlore geometry, we adopt a crystallographic coordinate system (a, b, c) (Fig. 4.1a). The three unit vectors $\mathbf{a}$, $\mathbf{b}$, and $\mathbf{c}$ are aligned with the crystallographic directions [100], [010], and [001] respectively. We set the origin at the center of an arbitrarily chosen up tetrahedron. The four corners are located at $\mathbf{r}_0 = (1,1,1)/8$, $\mathbf{r}_1 = (1,-1,-1)/8$, $\mathbf{r}_2 = (-1,1,-1)/8$, and $\mathbf{r}_3 = (-1,-1,1)/8$. They belong to sublattices 0, 1, 2, and 3, respectively. The cubic lattice constant is set to 1.

We also introduce local xyz frames whose orientation depends on the sublattice, shown in Fig. 4.1a [53]. Then,

$$\begin{aligned}
&\hat{\mathbf{x}}_0 = \frac{1}{\sqrt{6}}(-2,1,1);\ \hat{\mathbf{y}}_0 = \frac{1}{\sqrt{2}}(0,-1,1);\ \hat{\mathbf{z}}_0 = \frac{1}{\sqrt{3}}(1,1,1).\\
&\hat{\mathbf{x}}_1 = \frac{1}{\sqrt{6}}(-2,-1,-1);\ \hat{\mathbf{y}}_1 = \frac{1}{\sqrt{2}}(0,1,-1);\ \hat{\mathbf{z}}_1 = \frac{1}{\sqrt{3}}(1,-1,-1).\\
&\hat{\mathbf{x}}_2 = \frac{1}{\sqrt{6}}(2,1,-1);\ \hat{\mathbf{y}}_2 = \frac{1}{\sqrt{2}}(0,-1,-1);\ \hat{\mathbf{z}}_2 = \frac{1}{\sqrt{3}}(-1,1,-1).\\
&\hat{\mathbf{x}}_3 = \frac{1}{\sqrt{6}}(2,-1,1);\ \hat{\mathbf{y}}_3 = \frac{1}{\sqrt{2}}(0,1,1);\ \hat{\mathbf{z}}_3 = \frac{1}{\sqrt{3}}(-1,-1,1).
\end{aligned} \tag{4.1}$$

Here $\hat{\mathbf{x}}_i$, $\hat{\mathbf{y}}_i$, and $\hat{\mathbf{z}}_i$ form the frame for sublattice i sites. Note the local 3-fold axes are $\hat{\mathbf{z}}_i$.

Because of the strong spin-orbital coupling and the crystal field, spins point to the local 3-fold axes. We can write

$$\mathbf{S}_i = \hat{\mathbf{z}}_i S_i^z. \tag{4.2}$$

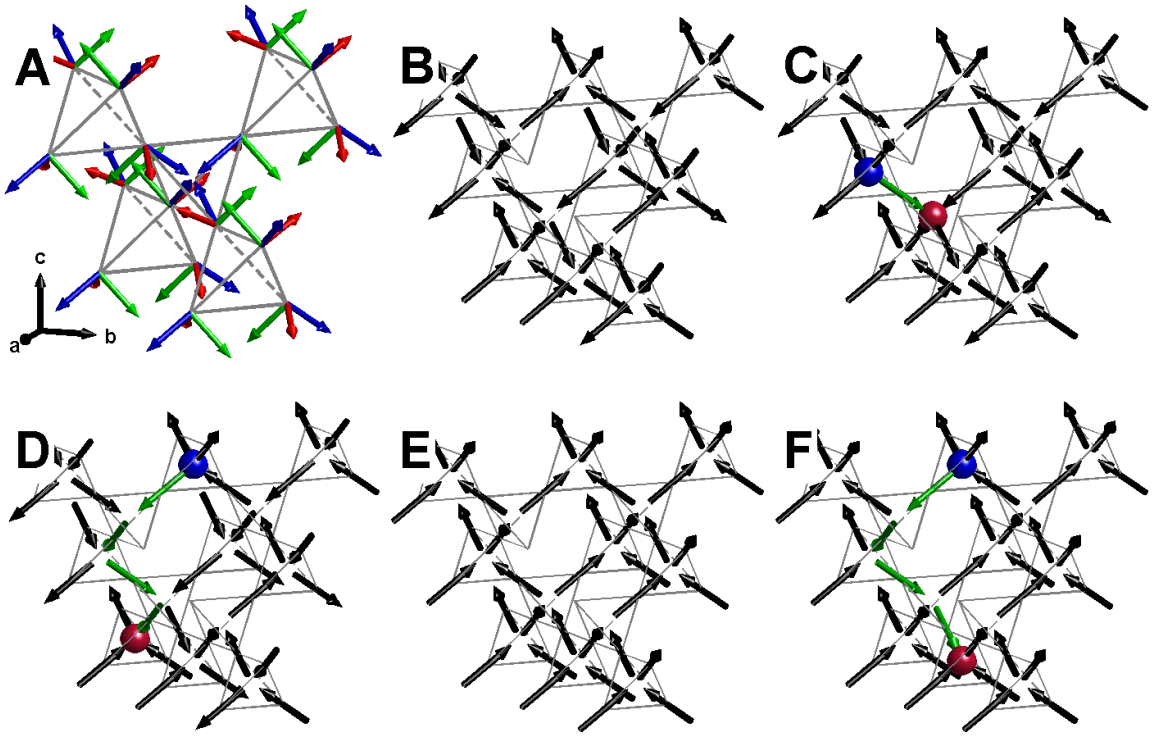

Figure 4.1: (a) The global and local frames in pyrochlore lattice. Red, green, and blue arrows stand for $\hat{\mathbf{a}}_i$, $\hat{\mathbf{b}}_i$, and $\hat{\mathbf{c}}_i$, respectively. (b) An example of the classical spin ice ground state. Note that all tetrahedra obey the $Q = 0$ condition. (c) Flipping a spin (green arrow) creates a pair of spinons with magnetic charge $Q = 1$ (red ball) and $Q = -1$ (blue ball). (d) The spinon pair can be separated far away by flipping a sequence of spins (green arrows). Note all tetrahedra obey $Q = 0$ except for the one hosting spinons. (e) Magnetic field along $\hat{\mathbf{c}}$ direction selects the fully-magnetized state as the ground state. (f) Spinons are bound by a string of flipped spins (green arrows). Now each flipped spin costs Zeeman energy.

$\hat{\mathbf{z}}_i$ is the unit vector that is parallel with the local 3-fold axis. $S_i^z = \pm 1/2$ denotes the two possible orientations of $\mathbf{S}_i$.

Neighboring magnetic moments are coupled by ferromagnetic exchange interaction. The Hamiltonian is written as,

$$H_{\mathrm{CSI}} = -\mathcal{J}\sum_{\langle ij\rangle}\mathbf{S}_i\cdot\mathbf{S}_j = -\mathcal{J}\sum_{\langle ij\rangle}(\hat{\mathbf{z}}_i\cdot\hat{\mathbf{z}}_j)S_i^zS_j^z = J\sum_{\langle ij\rangle}S_i^zS_j^z. \tag{4.3}$$

Here $\mathcal{J} > 0$ is the ferromagnetic coupling constant between magnetic moments. $J = \mathcal{J}/3$. We have used the fact that $\hat{\mathbf{z}}_i\cdot\hat{\mathbf{z}}_j = -1/3$ for adjacent spins. The model therefore effectively becomes an antiferromagnetic Ising model on pyrochlore lattice, which was first studied by P. W. Anderson in the context of cation ordering in ferrites [55].

As the Hamiltonian Eq. 4.3 is quadratic in S^z variables, we can complete the square,

$$H_{\mathrm{CSI}} = \frac{J}{2}\sum_{\alpha}Q_\alpha^2 + \text{const.} \tag{4.4}$$

The summation is over all the tetrahedra α in pyrochlore lattice. Q_α is defined as the sum of S^z on tetrahedron α,

$$Q_\alpha = -\epsilon_\alpha\sum_{i\in\alpha}S_i^z, \tag{4.5}$$

where the summation is over all the sites belong to tetrahedron α, and $\epsilon_\alpha = 1$ for up tetrahedra and -1 for down tetrahedra. $Q_\alpha = 0, \pm 1, \pm 2$.

The physical meaning of Q_α becomes transparent in terms of the spin magnetic moments $\mathbf{S}_i$. Recall that, in magnetostatics, the effective magnetic charge density is

the source of the magnetic H-field,

$$\nabla \cdot \mathbf{H} = \rho_M \equiv -\nabla \cdot \mathbf{M}, \tag{4.6}$$

where ρ_M is the effective magnetic charge density and $\mathbf{M}$ the magnetization field. The total magnetic charge enclosed inside a closed surface is given by,

$$-\int \mathbf{M} \cdot \hat{\mathbf{n}}\, d\sigma, \tag{4.7}$$

where $\hat{\mathbf{n}}$ is the unit normal vector. In pyrochlore lattice, the total magnetic charge enclosed inside the tetrahedron α is given by

$$-\sum_{i\in\alpha}(\hat{\mathbf{z}}_i S_i^z)\cdot\hat{\mathbf{n}}_i = -\epsilon_\alpha \sum_{i\in\alpha} S_i^z = Q_\alpha. \tag{4.8}$$

Here $\mathbf{n}_i$ are vectors pointing out from the center of the tetrahedron α, which is the lattice analog of the normal vector. We see that Q_α is simply the magnetic charge enclosed in α.

To find the ground state, we minimize the energy of the Eq.4.4 by setting,

$$Q_\alpha = 0, \quad \forall\alpha, \tag{4.9}$$

which means there is no magnetic charge in the ground state. For a single tetrahedron, the above condition selects the so-called "two-in-two-out" states, in which two moments point into the tetrahedron and two point out (Fig. 4.1b). Such a condition is analogous to the Bernal-Fowler rule governing proton states in water ice [56]. The magnet itself is a spin analog to the water ice crystal, hence the name spin ice.

Similar to the Kagome Ising antiferromagnet, Eq. 4.9 does not fix a unique ground state. To count the number of ground states, we perform a similar estimate. Eq. 4.9 selects 6 out of 16 states in a single tetrahedron, and the total number of spin states is 2^N, N being the number of sites. Thus,

$$\Omega \approx \left(\frac{6}{16}\right)^{N_{\text{tetra}}} 2^N = \left(\frac{3}{8}\right)^{N/2} 2^N = 1.225^N. \tag{4.10}$$

In terms of residual entropy,

$$S_0/(Nk_B) = \ln(\Omega) \approx 0.2027 \tag{4.11}$$

Here $N_{\text{tetra}} = N/2$ is the number of tetrahedra in pyrochlore lattice. The above result was originally due to Linus Pauling [56]. The numerical linked-cluster approximation gives $S_0/(Nk_B) \approx 0.2041$ [13]. We see that the zero temperature entropy is extensive.

Fluctuations in the degenerate ground states gives rise to interesting spin correlations at zero temperature [57]. To this end, we coarse grain the microscopic magnet moment to a magnetization field $\mathbf{M}(\mathbf{x})$. $\mathbf{M}$ is defined as

$$\mathbf{M}(\mathbf{x}) = \frac{1}{|V|} \sum_{i \in V(\mathbf{x})} \mathbf{S}_i. \tag{4.12}$$

Here $V(\mathbf{x})$ is a macroscopic region centered at point $\mathbf{x}$, and $|V|$ stands for its volume. The charge-free condition Eq. 4.9 is carried over to the magnetization field,

$$\rho_M = -\nabla \cdot \mathbf{M} = 0. \tag{4.13}$$

Therefore, the fluctuation of magnetization must be transverse. The entropy S is a

functional of $\mathbf{M}$, and, to the leading order, we have the following expansion,

$$S[\mathbf{M}] = S_0 - \frac{\kappa}{2}\int d^3x\, \mathbf{M}^2. \tag{4.14}$$

Here $\kappa > 0$ is a constant. Therefore, the correlation function at zero temperature is given by

$$\begin{aligned}\langle M^a(\mathbf{k})M^b(-\mathbf{k})\rangle_{T=0} &= \frac{\int \mathcal{D}\mathbf{M}\,\delta(\nabla\cdot\mathbf{M})M^a(\mathbf{k})M^b(-\mathbf{k})e^{S[\mathbf{M}]}}{\int \mathcal{D}\mathbf{M}\,\delta(\nabla\cdot\mathbf{M})e^{S[\mathbf{M}]}} \\ &= \frac{1}{\kappa}(\delta^{ab} - \frac{k^a k^b}{k^2}).\end{aligned} \tag{4.15}$$

Therefore, it shows a transverse correlation. The singularity at $k \to 0$ depends on the direction at which the singular point is approached. Such singular correlation has been observed in neutron scattering experiments [58, 59].

4.1.1 Spinons in classical spin ice

We are also interested in the excited states of classical spin ice. To this end, we return to the microscopic Hamiltonian 4.4. The ground state obeys the charge-free condition 4.9. To create an excitation, we flip a single spin S_i^z, whereby the two tetrahedra that share the said spin acquire magnetic charge $Q = \pm 1$ (Fig. 4.1c). In other words, each tetrahedron contains a spinon with unit magnetic charge, and a spinon costs energy $J/2$. These spinons can be separated far from each other by flipping successive spins at no additional energy cost. The spinons are therefore free

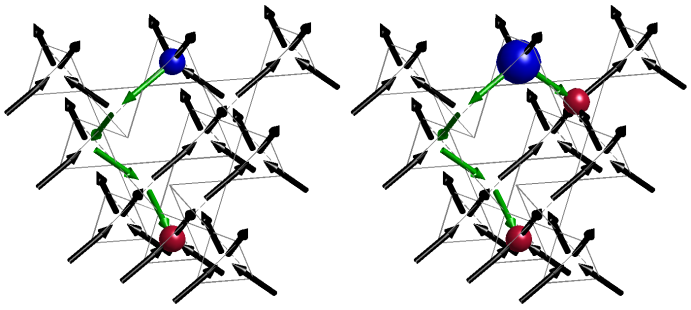

Figure 4.2: If the $Q = -1$ spinon (blue ball, left panel) makes a U-turn, it creates a $Q = -2$ spinon (blue ball, right panel) and two $Q = 1$ spinons (red ball, right panel), which costs additional energy J. Such a state has much higher energy comparing to the state with only one pair of $Q = \pm 1$ spinons and therefore can be safely ignored in the first approximation. As the string can only propagate upward, each string segment takes two possible orientations.

(Fig. 4.1d). This demonstrates that spin-flips are not elementary excitation as a spin-flip fractionalizes into a pair of spinons [47, 48].

In literature, these spinons are called "magnetic monopoles" for their close resemblance to Dirac monopoles [48]. However, an important distinction must be drawn: the spinons in classical spin ice are sources of magnetic H-field, whereas the Dirac monopoles are sources of magnetic B-field.

4.1.2 Strings in classical spin ice

Now we apply a weak magnetic field in the [001] direction. The Zeeman coupling is given by,

$$-\mathcal{B}\sum_i \hat{\mathbf{c}}\cdot\hat{\mathbf{z}}_i S_i^z = -B\sum_i \eta_i S_i^z. \tag{4.16}$$

Here $B = \mathcal{B}/\sqrt{3}$ is the Zeeman field for the effective spins. $\eta_i = 1$ in sublatttices 0 and 3, $\eta_i = -1$ in sublattices 1 and 2. The Hamiltonian is then written as,

$$H_{\text{field}} = \frac{J}{2}\sum_{\alpha} Q_{\alpha}^2 - B\sum_i \eta_i S_i^z. \tag{4.17}$$

We assume $B \ll J$. Note that we have ignored the coupling between the magnetic field and the S^x and S^y components as the Lande g-tensor is usually dominated by the longitudal component, $\mathbf{g} \sim \hat{\mathbf{z}}_i\hat{\mathbf{z}}_i$ in classical spin ice materials.

The ground state of Eq.4.17 is now unique; $S_i^z = 1$ on sublattices 0 and 3, and $S_i^z = -1$ on sublattices 1 and 2. In other words, the system is fully-magnetized in the sense that all spins have the positive projection along the field (Fig. 4.1e). To create excited states, we flip one spin S_i^z, thereby creating two spinons. To separate the two spinons, we need to successively flip a string of spins. Each flipped spin now costs Zeeman energy B. Therefore, the spinons are confined by a linear potential (Fig. 4.1f). The string of flipped spins are known as the Dirac string in the literature [49].

When an external magnetic field is present, the elementary excitations are strings. We consider thermal fluctuations of strings. A string can only grow in the [001] direction, and each string segment takes two possible orientations (Fig.4.2). Therefore, a string of length L has 2^L possible states, all with the same energy $J + BL$. The free energy associated with a string is,

$$F(L) = U - TS = J + BL - k_B T L \ln 2 = J + (B - k_B T \ln 2)L. \tag{4.18}$$

We see that the entropy reduces the effective string tension. In particular, when

$T > T_c = B/(k_B \ln 2)$, the tension becomes negative. It signals the instability of the fully magnetized ground state and the liberation of spinons. This transition is a classical analog of the confinement transition in gauge theory, known as Kasteleyn transition in literature [49, 60, 61].

4.2 Quantum string dynamics in 2D

In Section 4.1, we reviewed the basics of classical spin ice where the spins fluctuates through thermally assisted tunneling. In quantum spin ice, spins undergo significant quantum fluctuations. A quantum spin ice can be modeled as,

$$H_{\mathrm{QSI}} = H_{\mathrm{CSI}} + H'. \tag{4.19}$$

Here H_{CSI} is the classical spin ice Hamiltonian Eq.4.3, and H' are exchange interactions between spins that do not commute with H_{CSI}. The classical part H_{CSI} provides the extensively degenerate ground state manifold as we discussed in previous sections. H' assists the system tunnel from one state of this manifold to another, thereby generating quantum dynamics. In particular, elementary excitations such as spinons and strings now exhibit quantum motion [62].

In this section, we study the quantum dynamics of strings using a two-dimensional toy model of quantum spin ice known as square quantum spin ice [63]. The spins are defined on a checkerboard lattice, a two-dimensional analog of pyrochlore lattice (Fig. 4.3a). The crossed plaquettes are planar analogs of tetrahedra. The checker-

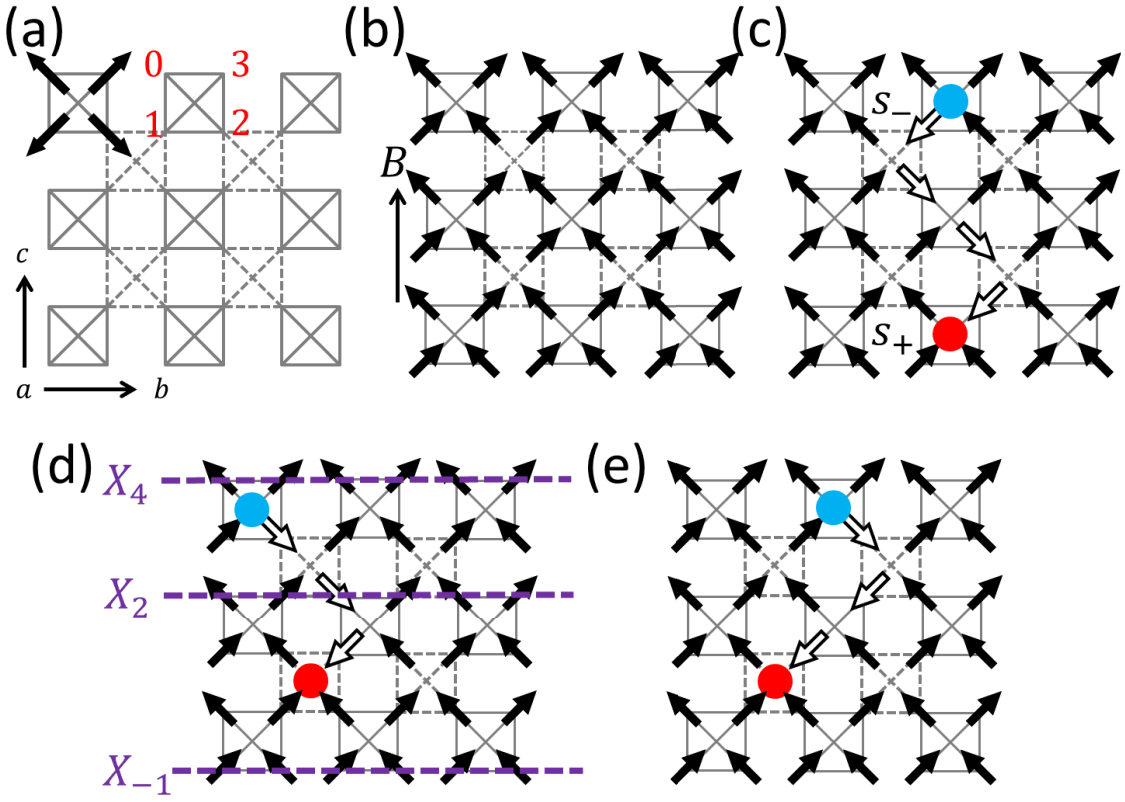

Figure 4.3: (a) The checkerboard lattice. 0. 1, 2, and 3 denote the four inequivalent lattice sites. Solid lines and dashed lines highlight two symmetrically inequivalent crossed-plaquettes, A and B. Arrows denote the local $\hat{\mathbf{z}}_i$ directions. The orientation of the global frame *abc* is shown. (b) The fully-magnetized state when the field is applied in the *c* direction. Arrows denote the spin orientations. (c) A string of flipped spins (open arrows) binding a $Q = +1$ spinon (red circle) and a $Q = -1$ one (blue circle). (d,e) Definition of X_c operators. The operator X_2 changes the orientation of the string segment with $c = 2$ from $\mathbf{l}$ to $\mathbf{r}$ in state (d) and results in a new state (e). The operators $X_{-1,4}$ fall outside the range of the string and act trivially on (d).

board lattice has four inequivalent sites, labeled 0 through 3, each forming a square lattice. There are also two inequivalent crossed-plaquettes, dubbed A and B in later discussion. Each site is then shared by an A plaquette and a B plaquette. We establish a coordinate system (a, b, c), where b and c are along the crystallographic [01] and [10] direction, and a is perpendicular to the paper.

The point of departure is the classical spin ice on this lattice, whose Hamiltonian is given by,

$$H_0 = J \sum_{\langle ij \rangle} S_i^z S_j^z = \frac{J}{2} \sum_{\alpha} Q_\alpha^2 + \text{const.} \tag{4.20}$$

Here the first summation is over all nearest neighbors. The second summation is over the crossed plaquettes α. $J > 0$ is the exchange coupling constant. $S_i^z = \mathbf{S}_i \cdot \hat{\mathbf{z}}_i$ is the z component of the spin at site i. Here $\hat{\mathbf{z}}_i$ is the local z axis (Fig. 4.3a). They are defined as,

$$\hat{\mathbf{z}}_0 = \frac{1}{\sqrt{2}}(0, 1, 1),\ \hat{\mathbf{z}}_1 = \frac{1}{\sqrt{2}}(0, -1, -1),\ \hat{\mathbf{z}}_2 = \frac{1}{\sqrt{2}}(0, 1, -1),\ \hat{\mathbf{z}}_3 = \frac{1}{\sqrt{2}}(0, -1, 1).$$

The magnetic charge enclosed in plaquette α, similar to the pyrochlore spin ice, is defined as,

$$Q_\alpha = -\epsilon_\alpha \sum_{i \in \alpha} S_i^z, \tag{4.21}$$

where $\epsilon_\alpha = 1$ for A plaquettes and -1 for B plaquettes.

Next we apply a weak magnetic field in the ac plane (Fig. 4.3b). In the local

frames, the perturbation reads

$$H_1 = -\sum_i (hS_i^x + B\eta_i S_i^z). \tag{4.22}$$

Here we chose the local y-axes to be orthogonal to the field and introduced $\eta_i \equiv \hat{\mathbf{c}} \cdot \hat{\mathbf{z}}_i = (-1)^{c_i}/\sqrt{2}$. In other words, $\eta_i = 1$ for 0 and 3 sublattices and -1 for 1 and 2 sublattices. The Zeeman term has two effects. Its longitudinal component B breaks the degeneracy of ice states and favors a fully magnetized state. The transverse component h induces quantum fluctuations of spins. We treat B and h as independent parameters in the toy model.

Flipping a single spin in the fully magnetized state creates two spinons with $Q = \pm 1$, which can be pulled further apart (Fig. 4.3c). The process creates a string of spins aligned against the field and connecting the spinons, the energy of a string with n segments is $J + Bn/\sqrt{2}$. For weak fields $B \ll J$, the Hilbert space thus separates into near-degenerate subspaces with a fixed number of strings. The transverse part of the Zeeman term mixes states in the same subspace through quantum tunneling, inducing quantum motion of strings. We use degenerate perturbation theory in the subspace with a single string to construct an effective theory of its quantum dynamics.

The first step is to label the shapes of a string. The shape of a string is specified by the orientation of its segment. Each segment can take two possible orientations. Therefore, the shape of a string can be described as a sequence,

$$\mathbf{s}_1, \mathbf{s}_2 \ldots \mathbf{s}_n,$$

or $\{\mathbf{s}_i\}$ for short, which take on the values $\mathbf{r} \equiv (0,1,1)/2$ and $\mathbf{l} \equiv (0,-1,1)/2$ in the *abc*-frame. The string thus propagates upwards from the $Q=+1$ spinon at $\mathbf{s}_+$ to the $Q=-1$ spinon at $\mathbf{s}_-$. The location of the ends of the string are related to each other. Specifically,

$$\mathbf{s}_- - \mathbf{s}_+ = \sum_{i=1}^{n} \mathbf{s}_i, \tag{4.23}$$

we only need to specify the location of one end of the string. In short, the state of a string is fully specified by its shape and location of one end, $|\mathbf{s}_+, \{\mathbf{s}\}\rangle$.

We then introduce a hybrid basis with fixed shape $\{\mathbf{s}_i\}$, c-coordinate of the spinon c_+, and the b-component of the total momentum k_b:

$$|k_b, c_+, \{\mathbf{s}_i\}\rangle = \sum_{b_+} e^{ik_b(b_+ + b_-)/2} |b_+, c_+, \{\mathbf{s}_i\}\rangle. \tag{4.24}$$

Here $(b_+ + b_-)/2$ is the b coordinate of the center of mass.

To the first order in h, the motion of a string involves removing or adding a segment at one of the ends, with an effective Hamiltonian

$$\begin{aligned} H_{\text{eff}}|c_+, \{\mathbf{s}_1 \dots \mathbf{s}_n\}\rangle &= (J + \frac{nB}{\sqrt{2}})|c_+, \{\mathbf{s}_1 \dots \mathbf{s}_n\}\rangle \\ &- \frac{h}{2} e^{ik_b b_n/2} |c_+, \{\mathbf{s}_1 \dots \mathbf{s}_{n-1}\}\rangle - \frac{h}{2} \sum_{\mathbf{s}_{n+1}} e^{-ik_b b_{n+1}/2} |c_+, \{\mathbf{s}_1 \dots \mathbf{s}_{n+1}\}\rangle \\ &- \frac{h}{2} e^{-ik_b b_1/2} |c_+ + 1, \{\mathbf{s}_2 \dots \mathbf{s}_n\}\rangle - \frac{h}{2} \sum_{\mathbf{s}_0} e^{ik_b b_0/2} |c_+ - 1, \{\mathbf{s}_0 \dots \mathbf{s}_n\}\rangle. \end{aligned} \tag{4.25}$$

Here b_i stands for the b-component of the vector $\mathbf{s}_i$. We have omitted the momentum index to simplify the notation. Though it looks complicated, each term in the above Hamiltonian has a clear meaning: the first term on the right hand side is the potential

energy of the string; the second and third terms remove or add a segment at the $Q = -1$ end of the string; the fourth and the fifth terms remove or add a segment to the $Q = 1$ end of the string.

When $k_b = 0$, diagonalization of H_{eff} is simplified by the presence of multiple reflection symmetries. Define the parity operator X_c that switches between the $\mathbf{l}$ and $\mathbf{r}$ orientations of the segment with coordinate c and keeps all other segment variables $\mathbf{s}_i$ intact (Fig. 4.3d,e), e.g.

$$X_c|c_+, \ldots \mathbf{s}_{c-c_+}, \mathbf{l} \ldots\rangle = |c_+, \ldots \mathbf{s}_{c-c_+}, \mathbf{r} \ldots\rangle. \tag{4.26}$$

When X_c falls outside the range of the string, $c_+ < c < c_-$, it acts on the vacuum state, which is symmetric, so we set $X_c|c_+, \{\mathbf{s}\}\rangle = +|c_+, \{\mathbf{s}\}\rangle$ in this case. It can be seen that $X_c^2 = 1$ and $[X_c, X_{c'}] = 0$.

Although X_c does not preserve the coordinate of the other end of the string $\mathbf{s}_-$, at $k_b = 0$ its horizontal displacement makes no difference. Therefore, $[X_c, H_{\text{eff}}] = 0$ when $k_b = 0$. Thus, all $k_b = 0$ eigenstates of H_{eff} can be classified by their parities under $\{X_c\}$ and H_{eff} becomes block-diagonal.

4.2.1 All-even sector

The most important states have all even parities, $X_c = +1$. An all-even state of a string of length n and longitudinal momentum k_c is

$$|k_c, n\rangle = 2^{-n/2} \sum_{c_+} \sum_{\mathbf{s_1} \ldots \mathbf{s_n}} e^{ik_c(c_+ + c_-)/2} |c_+, \{\mathbf{s}_1 \ldots \mathbf{s}_n\}\rangle. \tag{4.27}$$

Therefore, the even parity state $|k_c, n\rangle$ is the equal-amplitude superposition of all string shapes with a given length n.

For them, the Hamiltonian (Eq.4.25) simplifies,

$$H_{\text{eff}}|n\rangle = \left(J + \frac{nB}{\sqrt{2}}\right)|n\rangle - \sqrt{2}h\cos\frac{k_c}{2}(|n+1\rangle + |n-1\rangle). \tag{4.28}$$

The above is equivalent to the problem of a particle on a one-dimensional lattice subject to a constant force $-B/\sqrt{2}$ and a hard wall at $n = 0$, which can be diagonalized numerically and solved analytically in certain limits.

When $B \ll h$, we use the continuum approximation to find the spectrum. The Schrödinger equation becomes

$$H_{\text{eff}}\psi(n) = (J + n\frac{B}{\sqrt{2}} - 2t)\psi(n) - t\frac{d^2\psi}{dn^2} = E\psi(n), \quad \psi(0) = 0. \tag{4.29}$$

where $t = |\sqrt{2}h\cos(k_c/2)|$. The solution of the Schrödinger equation gives

$$E_j(k_c) = J - 2\sqrt{2}\left|h\cos\frac{k_c}{2}\right| - \lambda_j\left|\frac{B^2 h}{\sqrt{2}}\cos\frac{k_c}{2}\right|^{1/3}. \tag{4.30}$$

Here λ_j are roots of the Airy function, $\lambda_1 = -2.33811$, $\lambda_2 = -4.08795$, etc. The character length scale of the string is $\xi = 4h/B$.

When $B \gg h$, the lowest eigenstate is a single misaligned spin with the dispersion

$$E_1(k_c) = J + \frac{B}{\sqrt{2}} - \frac{\sqrt{2}h^2}{B}(1 + \cos k_c). \tag{4.31}$$

4.2.2 Dynamical structure factor

Strings can be directly observed in neutron scattering experiments. A scattered neutron flips a spin in the fully-polarized background, creating a string of length 1.

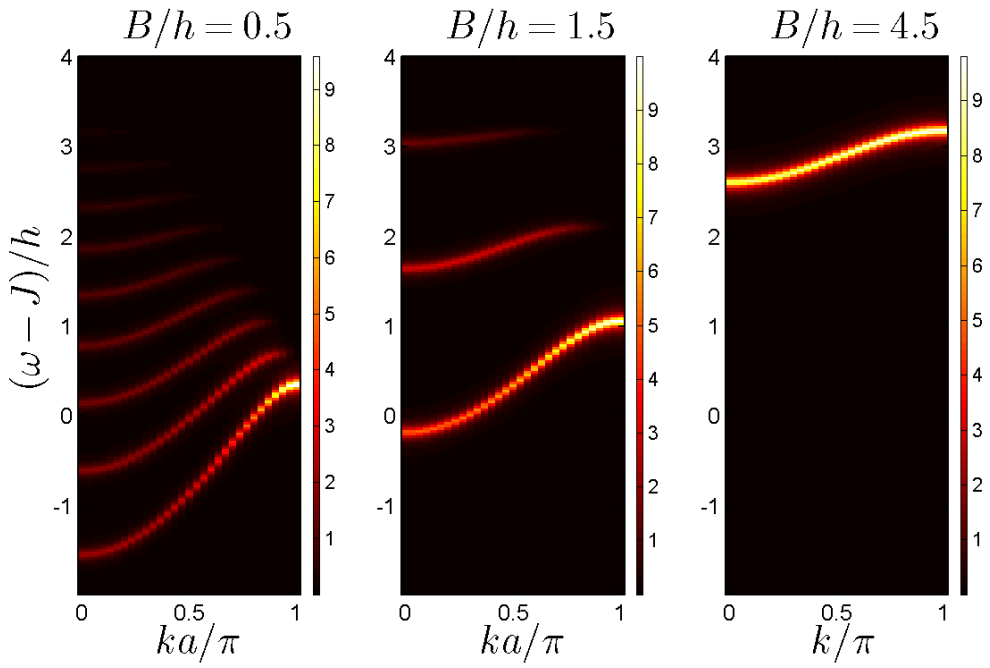

Figure 4.4: Dynamical structure factor $-\mathrm{Im}S^{aa}(\mathbf{k},\omega)$ for $\mathbf{k} \parallel \mathbf{B}$. The magnetic field is along [01] direction.

The intensity of scattering is controlled by the overlap between a length-1 string and a string eigenstate of H_{eff}.

In this section, we calculate the dynamical structure factors $S^{\alpha\alpha}(\mathbf{k},\omega)$, $\alpha = a,\ b,\ c$. The imaginary part of the dynamical structure factor is given by Kubo formula,

$$-\mathrm{Im}S^{\alpha\alpha}(\mathbf{k},\omega)/\pi = \sum_j |f_j^\alpha(\mathbf{k})|^2 \delta(\omega - E_j + E_G). \tag{4.32}$$

The summation is over all excited states j with excitation energy $E_j - E_G$. The scattering amplitude $f_j^\alpha(\mathbf{k})$ is given by

$$f_j^\alpha(\mathbf{k}) = \sum_{\mathbf{R}} e^{i\mathbf{k}\cdot\mathbf{R}} \langle j|S_{\mathbf{R}}^\alpha|G\rangle \tag{4.33}$$

Here $|G\rangle$ is the ground state. $\mathbf{R}$ is the spatial position of operator $S_{\mathbf{R}}^\alpha$.

For the sake of simplicity, we consider S^{aa} only. At the leading order in h/J, the ground state is the fully-polarized state. The effect of $S^c_{\mathbf{R}}$ on the ground state is to flip the spin at $\mathbf{R}$ or equivalently to create a string of length 1. Therefore,

$$\sum_{\mathbf{R}} S^a_{\mathbf{R}} e^{i\mathbf{k}\cdot\mathbf{R}}|G\rangle = \frac{1}{\sqrt{2}}(e^{i\mathbf{k}\cdot\mathbf{l}/2}|\mathbf{k},\mathbf{l}\rangle + e^{i\mathbf{k}\cdot\mathbf{r}/2}|\mathbf{k},\mathbf{r}\rangle) \equiv |\mathbf{k},\psi\rangle, \tag{4.34}$$

up to a normalization constant. Here $|\mathbf{k},\mathbf{l}/\mathbf{r}\rangle$ is the length 1 string state with total momentum $\mathbf{k}$ and bond orientation $\mathbf{l}/\mathbf{r}$. The low energy scattering is dominated by the scattering processes between the ground state and single string states. Hence, we only need to sum over all single-string states instead of the whole Hilbert space. The scattering amplitude is determined by the overlap between $|\mathbf{k},\psi\rangle$ and the single-string eigenstate $|\mathbf{k},j\rangle$ of H_{eff}:

$$f_j(\mathbf{k}) = \langle \mathbf{k},j|\mathbf{k},\psi\rangle. \tag{4.35}$$

When $k_b = 0$, the calculation is greatly simplified thanks to the parity symmetry. The initial state $|\mathbf{k},\psi\rangle$ becomes

$$|\mathbf{k},\psi\rangle = \frac{1}{\sqrt{2}}(|\mathbf{k},\mathbf{l}\rangle + |\mathbf{k},\mathbf{r}\rangle) = |k_c, n=1\rangle_{\text{even}}, \tag{4.36}$$

which is an all-even state. Therefore, only even-parity states $|k_c,n\rangle$ are needed to calculate $S^{aa}(k_b = 0,\omega)$.

Fig. 4.4 shows the dynamical structure factor $-\text{Im}S^{aa}(\omega,\mathbf{k})$ at several values of B/h for $k_b = 0$. For $B \ll h$, the spectrum consists of overlapping bands, whereas for $B \gg h$ the bands separate and the spectrum becomes dominated by the shortest string consisting of a single flipped spin, in essence a magnon.

4.3 Quantum string dynamics in 3D

In this section, we discuss the quantum strings in pyrochlore quantum spin ice. Pyrochlore quantum spin ice has the identical lattice geometry as the classical spin ice. We follow the convention established in Section 4.1. The general exchange Hamiltonian that consistent with lattice symmetries can be written in the local xyz frames as [64],

$$H = \sum_{\langle ij \rangle} J_{zz} S_i^z S_j^z - J_{z\pm}[S_i^z(\zeta_{ij} S_j^+ + \zeta_{ij}^* S_j^-) + (i \leftrightarrow j)]$$
$$- J_\pm (S_i^+ S_j^- + h.c.) - J_{\pm\pm}(\zeta_{ij}^* S_i^+ S_j^+ + h.c.) \tag{4.37}$$

Here $\zeta_{ij} = \zeta_{ji}$ are phase factors with i and j labeling spin sublattices 0 to 3. Specifically, $\zeta_{01} = \zeta_{23} = -1$, $\zeta_{02} = \zeta_{13} = \exp(i\pi/3)$, $\zeta_{03} = \zeta_{12} = \exp(-i\pi/3)$, and $\zeta_{ii} = 0$. The J_{zz} term describes classical spin ice, whereas the three remaining terms create quantum fluctuations. The value of the four parameters, J_{zz}, $J_\pm$, $J_{z\pm}$, and $J_{\pm\pm}$ depend on the materials. Note that the first term proportional to J_{zz} is the classical spin ice Hamiltonian, and the rest bring quantum fluctuations to the system.

A magnetic field applied in the [001] direction adds the Zeeman term

$$H' = -B \sum_i \alpha_i S_i^x + \beta_i S_i^y + \gamma_i S_i^z \tag{4.38}$$

with the cosines

$$\alpha_{0,3} = -\alpha_{1,2} = \frac{g_{xy}}{g_z\sqrt{6}},\ \beta_{0,3} = -\beta_{1,2} = \frac{g_{xy}}{g_z\sqrt{2}},\ \gamma_{0,3} = -\gamma_{1,2} = \frac{1}{\sqrt{3}}. \tag{4.39}$$

where g_{xy} and g_z are the principal components of the Landë g-tensor.

We assume that the J_{zz} term dominates and treat the rest of the terms as perturbations. The Zeeman term $-B\gamma_i S_i^z$ favors the fully-magnetized state. Similar to the two-dimensional toy model, excitations are open strings connecting a pair of spinons with $Q = \pm 1$.

The state of a string $|\mathbf{s}_+, \{\mathbf{s}_i\}\rangle$ is again parametrized by the location of its $Q = +1$ end $\mathbf{s}_+$ and by its shape $\{\mathbf{s}_1, \mathbf{s}_2 \ldots \mathbf{s}_n\}$. String segments $\mathbf{s}_i$ have four possible orientations: $\mathbf{b}_0 = (1,1,1)/4$, $\mathbf{b}_1 = (-1,1,1)/4$, $\mathbf{b}_2 = (1,-1,1)/4$, and $\mathbf{b}_3 = (-1,-1,1)/4$. A segment with orientation $\mathbf{b}_0$ or $\mathbf{b}_3$ must be followed by a segment with orientation $\mathbf{b}_1$ or $\mathbf{b}_2$, and vice versa.

The effective Hamiltonian in the subspace of a single string is

$$H_{\text{eff}} = -\sqrt{3}J_{z\pm}K_1 - J_{\pm}K_2 - 2J_{\pm\pm}K_3 + V \tag{4.40}$$

Kinetic terms K_1 and K_2 describe first and second-neghbor hopping of the string ends, whereas K_3 describes the hopping of a string of length 1. $V = J + nB/\sqrt{3}$ for a string of length n. The explicit form of K_i is given in Appendix A.

The above effective Hamiltonian cannot be solved analytically and we seek numerical solution instead. Here we directly evaluate the dynamical structure factor. Specifically, we consider the special case in which the momentum transfer is parallel with the field direction, $\mathbf{k} \parallel \mathbf{B}$. The relevant dynamical structure factor in neutron scattering experiments is the combination $I(\mathbf{k}, \omega) = -(\text{Im}S^{aa} + \text{Im}S^{bb})/\pi$, which is computed from the Kubo formula Eq. 4.32 and Eq. 4.33. The details of the calculation

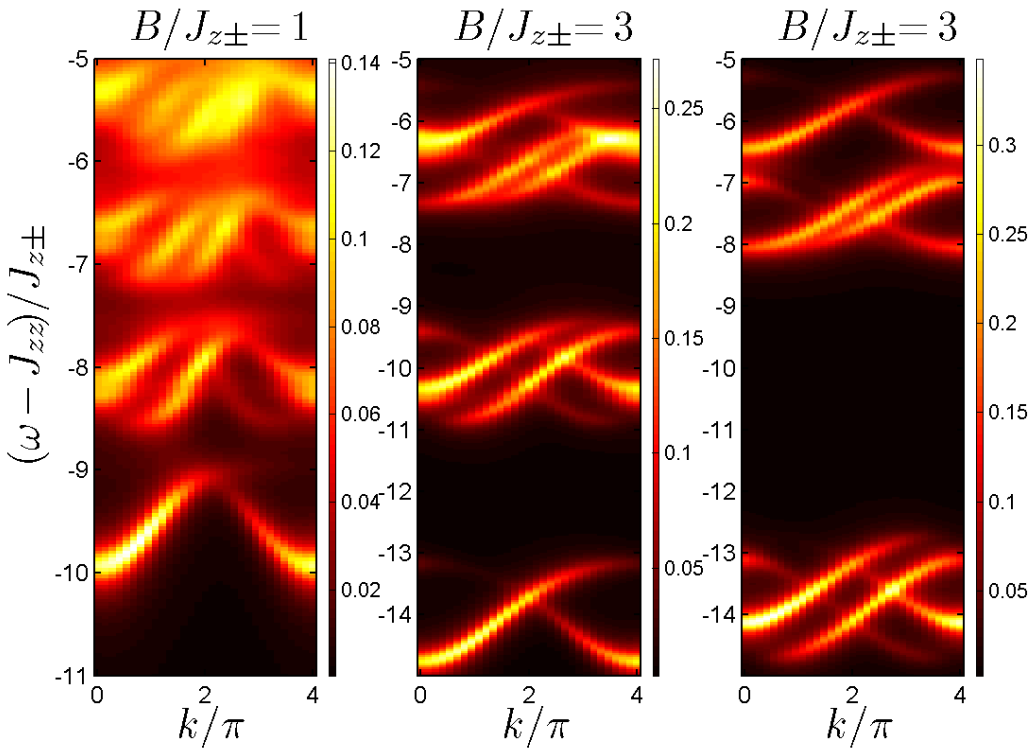

Figure 4.5: Neutron scattering spectrum $I(\mathbf{k}, \omega)$ for $\mathbf{k} \parallel \mathbf{B}$. The field is applied in the [001] direction.

are avaiable in Appendix A.

Fig. 4.5 shows the neutron scattering spectrum $I(k_b = 0, k_c, \omega)$ calculated with the aid of Lanczos diagonalization. We set $J_\pm = J_{\pm\pm} = 0.36 J_{z\pm}$, and $g_{xy}/g_z = 2.4$ as in the pyrochlore quantum spin ice material $Yb_2Ti_2O_7$ [53]. The spectral features resemble those of 2D strings. The branches gradually separate as the string tension increases with B.

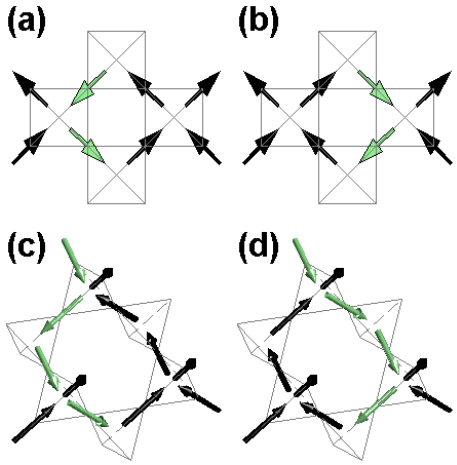

Figure 4.6: Loop-flipping processes in (a,b) checkerboard lattice $|\mathbf{lr}\rangle \leftrightarrow |\mathbf{rl}\rangle$ and (c,d) pyrochlore lattice $|\mathbf{b}_2\mathbf{b}_3\mathbf{b}_1\rangle \leftrightarrow |\mathbf{b}_1\mathbf{b}_3\mathbf{b}_2\rangle$.

4.4 String shape fluctuations

So far, our discussion on string dynamics is limited to the leading order perturbation theory. As we proceed to higher orders, new physics sets in. At the leading order, strings can grow and retract. At higher-orders in these couplings, the string's shape can change as well. The process involves the simultaneous reversal of spins around a closed loop (minimal length 4 in square spin ice and 6 in pyrochlore spin ice), as shown in Fig. 4.6 [65].

In this section, we investigate the effects of these shape fluctuations. We first examine the square quantum spin ice. To this end, we fix the both ends of the string to single out the shape fluctuation. The shape of a string is labeled by the sequence $\mathbf{s}_1, \mathbf{s}_2, \cdots \mathbf{s}_n$. We then represent the string shapes by a chain of pseudo $S = 1/2$ spins τ_i, $i = 1, 2, \cdots n$. $\mathbf{l}$ and $\mathbf{r}$ are represented as $\tau^z = \pm 1/2$.

Equipped with the above pseudo-spin representation, the shape fluctuations are described by a one-dimensional $S = 1/2$ XY model [66]. In square quantum spin ice, a state $|\ldots \mathbf{lr} \ldots\rangle$ turns into $|\ldots \mathbf{rl} \ldots\rangle$ and vice versa. In terms of pseudo-spins, a state $|\ldots \uparrow\downarrow \ldots\rangle$ turns into $|\ldots \downarrow\uparrow \ldots\rangle$ and vice versa, which is exactly identical to the action of a pseudo-spin exchange operator for nearest-neighbor spins $\tau_i^+\tau_{i+1}^- + \tau_i^-\tau_{i+1}^+$. The effective Hamiltonian for shape fluctuations is given by

$$H_{\text{fluc}} = V_{\text{2D}} \sum_{i=1}^{n-1} (\tau_i^+\tau_{i+1}^- + \text{H.c.}), \tag{4.41}$$

where $V_{\text{2D}} = \mathcal{O}(h^4/J^3)$. The above model is analytically solved by mapping it onto a chain of free fermions. The ground state energy of the above spin chain is given by $-2|V_{\text{2D}}|/\pi$. Therefore, shape fluctuations reduce tension of the string to $B/\sqrt{2} - 2|V_{\text{2D}}|/\pi$. When the applied field is below the critical strength $B_c = 2\sqrt{2}|V_{\text{2D}}|/\pi$, the energy cost for string excitations is negative and the fully-polarized state becomes unstable.

A similar transition occurs in the pyrochlore quantum spin ice. Similarly, the shapes of string with both ends fixed can be mapped onto a chain of pseudo $S = 1/2$ spins. The effective Hamiltonian for the shape fluctuations are mapped onto a one-dimensional XY model with only second-neighbor interactions:

$$H_{\text{fluc}} = V_{\text{3D}} \sum_{i=1}^{n-1} (\tau_{2i-1}^+\tau_{2i+1}^- + \tau_{2i}^+\tau_{2i+2}^- + \text{H.c.}). \tag{4.42}$$

The string tension is reduced by $2|V_{3D}|/\pi$. When B is below the critical value $B_c = 2\sqrt{3}|V_{\text{3D}}|/\pi$, the polarized state becomes unstable.

The fate of the ground state below B_c depends on the dimensionality of the model. On the one hand, the zero field ground state of the pyrochlore quantum spin ice in the perturbative regime $J_{z\pm,\pm,\pm\pm} \ll J_{zz}$ is a $U(1)$ spin liquid with free spinons [62]. Therefore, the transition at B_c could be associated with deconfinement of spinons. On the other hand, given that the compact quantum electrodynamics is always confined in two dimension [67], the $B = 0$ ground state of the square quantum spin ice is likely another confined phase separated from the fully-polarized state by the transition at B_c.

4.5 Discussion

We connect the results presented in the previous and the current chapters to lattice gauge theory. As we argued in Chapter 1, a frustrated magnet can be modeled by a lattice gauge theory. As we have seen in Chapter 2, a lattice gauge theory in general possesses two distinct phases, a weakly-coupled phase with free charges, and a strongly-coupled phase with confined charges. When charges are confined, elementary excitations are electric strings.

The physics we discussed in the last two chapters are manifestations of the above gauge theory physics. In kagome Heisenberg antiferromagnet, the spinons are charge excitations in an Ising gauge theory. The weakly-coupled phase of the Ising gauge theory describes the resonating-valence-bond state of the magnet, whereas the strongly-

coupled phase corresponds to a valence bond solid. Likewise, the quantum spin ice is described by a compact QED. The spinons are charge excitations in the compact QED. The external magnetic field drives the system into the confined phase, and the electric strings become elementary excitations.

Appendix A

Details of calculations in pyrochlore spin ice

A.1 The explicit form of K_i

We introduce the momentum basis for strings in pyrochlore quantum spin ice:

$$|\mathbf{k}, \{\mathbf{s}_i\}\rangle = \sum_{\mathbf{s}_+} e^{i\mathbf{k}\cdot(\mathbf{s}_+ + \mathbf{s}_-)/2} |\mathbf{s}_+, \{\mathbf{s}_i\}\rangle. \tag{A.1}$$

Here $\mathbf{s}_+$ and $\mathbf{s}_i$ have been defined in the main text. For a string with momentum $\mathbf{k}$,

$$\begin{aligned} K_1|\{\mathbf{s}_1 \dots \mathbf{s}_n\}\rangle &= \gamma^*(\mathbf{s}_{n-1}, \mathbf{s}_n) e^{i\mathbf{k}\cdot\mathbf{s}_n/2} |\{\mathbf{s}_1 \dots \mathbf{s}_{n-1}\}\rangle \\ &+ \sum_{\mathbf{s}_{n+1}} \gamma(\mathbf{s}_n, \mathbf{s}_{n+1}) e^{-i\mathbf{k}\cdot\mathbf{s}_{n+1}/2} |\{\mathbf{s}_1 \dots \mathbf{s}_{n+1}\}\rangle \\ &+ \gamma^*(\mathbf{s}_2, \mathbf{s}_1) e^{-i\mathbf{k}\cdot\mathbf{s}_1/2} |\{\mathbf{s}_2 \dots \mathbf{s}_n\}\rangle \\ &+ \sum_{\mathbf{s}_0} \gamma(\mathbf{s}_1, \mathbf{s}_0) e^{i\mathbf{k}\cdot\mathbf{s}_0/2} |\{\mathbf{s}_0 \dots \mathbf{s}_n\}\rangle. \end{aligned} \tag{A.2}$$

$$\begin{aligned} K_2|\{\mathbf{s}_1 \dots \mathbf{s}_n\}\rangle &= e^{i\mathbf{k}\cdot(\mathbf{s}_{n-1}+\mathbf{s}_n)/2} |\{\mathbf{s}_1 \dots \mathbf{s}_{n-2}\}\rangle \\ &+ e^{-i\mathbf{k}\cdot(\bar{\mathbf{s}}_n - \mathbf{s}_n)} |\{\mathbf{s}_1 \dots \bar{\mathbf{s}}_n\}\rangle \\ &+ \sum_{\mathbf{s}_{n+1}, \mathbf{s}_{n+2}} e^{-i\mathbf{k}\cdot(\mathbf{s}_{n+1}+\mathbf{s}_{n+2})/2} |\{\mathbf{s}_1 \dots \mathbf{s}_{n+2}\}\rangle \\ &+ e^{-i\mathbf{k}\cdot(\mathbf{s}_1+\mathbf{s}_2)/2} |\{\mathbf{s}_3 \dots \mathbf{s}_n\}\rangle \\ &+ e^{i\mathbf{k}\cdot(\bar{\mathbf{s}}_1 - \mathbf{s}_1)} |\{\bar{\mathbf{s}}_1 \dots \mathbf{s}_n\}\rangle \\ &+ \sum_{\mathbf{s}_{-1}, \mathbf{s}_0} e^{i\mathbf{k}\cdot(\mathbf{s}_{-1}+\mathbf{s}_0)/2} |\{\mathbf{s}_{-1} \dots \mathbf{s}_n\}\rangle \end{aligned} \tag{A.3}$$

$$\begin{aligned} K_3|\mathbf{b}_{0,3}\rangle &= \sum_{i=1,2} \zeta^*_{[0,3]i} \cos\left(\mathbf{k}\cdot\frac{\mathbf{b}_{0,3}+\mathbf{b}_i}{2}\right)|\mathbf{b}_i\rangle; \quad K_3|\mathbf{b}_{1,2}\rangle \\ &= \sum_{i=0,3} \zeta_{[1,2]i} \cos\left(\mathbf{k}\cdot\frac{\mathbf{b}_{1,2}+\mathbf{b}_i}{2}\right)|\mathbf{b}_i\rangle. \end{aligned} \tag{A.4}$$

We have omitted momentum index $\mathbf{k}$ for clarity. Here $\gamma(\mathbf{b}_i, \mathbf{b}_j) \equiv \gamma_{ij}$ is a 4×4 anti-Hermitian matrix with nonzero elements $\gamma_{01} = i - re^{-i\pi/3}$, $\gamma_{02} = e^{i5\pi/6} - re^{-i\pi/3}$, $\gamma_{13} = e^{i\pi/6} + re^{i\pi/3}$, $\gamma_{23} = i + re^{i\pi/3}$; and $r = g_{xy}B/(3\sqrt{2}g_z J_{z\pm})$. The short-hand notation $\bar{\mathbf{s}}_i$ means exchanging $\mathbf{b}_0 \leftrightarrow \mathbf{b}_3$ and $\mathbf{b}_1 \leftrightarrow \mathbf{b}_2$.

A.2 Evaluation of scattering amplitude

To evaluate the amplitude $f_j(\mathbf{k})$, we note,

$$\begin{aligned}|\mathbf{k},\psi_a\rangle &\equiv \sum_{\mathbf{R}} e^{i\mathbf{k}\cdot\mathbf{R}} S^a |G\rangle \\ &= \frac{1}{2}(e^{i\mathbf{k}\cdot\mathbf{R}_0}|\mathbf{k},\mathbf{b}_0\rangle + e^{i\mathbf{k}\cdot\mathbf{R}_1}|\mathbf{k},\mathbf{b}_1\rangle - e^{i\mathbf{k}\cdot\mathbf{R}_2}|\mathbf{k},\mathbf{b}_2\rangle - e^{i\mathbf{k}\cdot\mathbf{R}_3}|\mathbf{k},\mathbf{b}_3\rangle) \qquad \text{(A.5a)}\\ |\mathbf{k},\psi_b\rangle &\equiv \sum_{\mathbf{R}} e^{i\mathbf{k}\cdot\mathbf{R}} S^b |G\rangle \\ &= \frac{1}{2}(e^{i(\mathbf{k}\cdot\mathbf{R}_0+\pi/3)}|\mathbf{k},\mathbf{b}_0\rangle - e^{i(\mathbf{k}\cdot\mathbf{R}_1-\pi/3)}|\mathbf{k},\mathbf{b}_1\rangle \\ &\quad + e^{i(\mathbf{k}\cdot\mathbf{R}_2-\pi/3)}|\mathbf{k},\mathbf{b}_2\rangle - e^{i(\mathbf{k}\cdot\mathbf{R}_3+\pi/3)}|\mathbf{k},\mathbf{b}_3\rangle) \qquad \text{(A.5b)}\end{aligned}$$

Here $|\mathbf{k},\mathbf{b}_i\rangle$ stands for the length-1 string with segment orientation $\mathbf{b}_i$ and total momentum $\mathbf{k}$. $\mathbf{R}_i$ are spatial coordinates of the four inequivalent sites in pyrochlore lattice. The phase factors are due to the mismatch between the local spin frames (x,y,z) and global spin frame (a,b,c). The Kubo formula can then be rewritten as

$$-\frac{1}{\pi}\mathrm{Im}S^{\alpha\alpha}(\mathbf{k},\omega) = -\frac{1}{\pi}\mathrm{Im}\langle\mathbf{k},\psi_\alpha|\frac{1}{\omega+i0^+-H_{\text{eff}}}|\mathbf{k},\psi_\alpha\rangle \qquad \text{(A.6)}$$

where H_{eff} is the effective Hamiltonian for a single string in pyrochlore quantum spin ice and $|\psi^a\rangle$ and $|\psi^b\rangle$ are for S^{aa} and S^{bb} respectively.

Bibliography

[1] Lucretius, *The Nature of Things*. Penguin Classics, 2007.

[2] A. P. Ramirez, "Strongly geometrically frustrated magnets," *Annu. Rev. Mater. Sci.*, vol. 24, pp. 453–480, 1994.

[3] L. Balents, "Spin liquids in frustrated magnets," *Nature*, vol. 464, pp. 199–208, 2010.

[4] J. T. Chalker, "Geometrically frustrated antiferromagnets: statistical mechanics and dynamics," in *Introduction to Frustrated Magnetism*, C. Lacroix, P. Mendels, and F. Mila, Eds. Springer, 2011.

[5] I. Syôzi, "Statistics of kagomé lattice," *Prog. Theor. Phys.*, vol. 6, 1951.

[6] K. Kanô and S. Naya, "Antiferromagnetism. The kagomé Ising net," *Prog. Theor. Phys.*, vol. 10, pp. 158–172, 1953.

[7] R. M. White, *Quantum Theory of Magnetism*, 3rd ed. Springer, 2006.

[8] J. Kogut, "An introduction to lattice gauge theory and spin systems," *Rev. Mod. Phys.*, vol. 51, pp. 659–713, 1979.

[9] R. Savit, "Duality in field theory and statistical systems," *Rev. Mod. Phys.*, vol. 52, pp. 453–487, 1980.

[10] A. Kitaev, "Anyons in an exactly solved model and beyond," *Ann. Phys. (N. Y.)*, vol. 321, pp. 2–111, 2006.

[11] P. S. Alexandroff, *Combinatorial Topology.* Dover Publications, 2011.

[12] S. Sachdev, "Kagome- and triangular-lattice Heisenberg antiferromagnets: Ordering from quantum fluctuations and quantum-disordered ground states with unconfined bosonic spinons," *Phys. Rev. B*, vol. 45, p. 12377, 1992.

[13] R. R. P. Singh and D. A. Huse, "Ground state of the spin-1/2 kagome-lattice Heisenberg antiferromagnet," *Phys. Rev. B*, vol. 76, p. 180407, 2007.

[14] G. Evenbly and G. Vidal, "Frustrated antiferromagnets with entanglement renormalization: Ground state of the spin-1/2 Heisenberg model on a kagome lattice," *Phys. Rev. Lett.*, vol. 104, p. 187203, 2010.

[15] Y. Ran, M. Hermele, P. A. Lee, and X.-G. Wen, "Projected-wave-function study of the spin-1/2 Heisenberg model on the kagome lattice," *Phys. Rev. Lett.*, vol. 98, p. 117205, 2007.

[16] L. Messio, B. Bernu, and C. Lhuillier, "Kagome antiferromagnet: A chiral topological spin liquid?" *Phys. Rev. Lett.*, vol. 108, p. 207204, 2012.

[17] M. B. Hastings, "Dirac structure, rvb, and goldstone modes in the kagome antiferromagnet," *Phys. Rev. B*, vol. 63, p. 014413, 2000.

[18] Y. Iqbal, F. Becca, S. Sorella, and D. Poilblanc, "Gapless spin-liquid phase in the kagome spin-1/2 Heisenberg antiferromagnet," *Phys. Rev. B*, vol. 87, p. 060405, 2013.

[19] S. Capponi, V. R. Chandra, A. Auerbach, and M. Weinstein, "$p6$ chiral resonating valence bonds in the kagome antiferromagnet," *Phys. Rev. B*, vol. 87, p. 161118, 2013.

[20] S. Yan, D. A. Huse, and S. R. White, "Spin-liquid ground state of the $S = 1/2$ kagome Heisenberg antiferromagnet," *Science*, vol. 332, pp. 1173–1176, 2011.

[21] S. Depenbrock, I. P. McCulloch, and U. Schollwöck, "Nature of the spin-liquid ground state of the $S = 1/2$ Heisenberg model on the kagome lattice," *Phys. Rev. Lett.*, vol. 109, p. 067201, 2012.

[22] H.-C. Jiang, Z. Wang, and L. Balents, "Identifying topological order by entanglement entropy," *Nature Physics*, vol. 8, pp. 902–905, 2012.

[23] P. W. Anderson, "Resonating valence bonds: A new kind of insulator?" *Mater. Res. Bull.*, vol. 8, p. 153160, 1973.

[24] Y. Wan and O. Tchernyshyov, "Phenomenological Z_2 lattice gauge theory of the spin-liquid state of the kagome Heisenberg antiferromagnet," *Phys. Rev. B*, vol. 87, p. 104408, 2013.

[25] C. K. Majumdar and D. K. Ghosh, "On next-nearest-neighbor interaction in linear chain. I," *J. Math. Phys.*, vol. 10, p. 1388, 1969.

[26] T. Nakamura and K. Kubo, "Elementary excitations in the Δ chain," *Phys. Rev. B*, vol. 53, pp. 6393–6400, 1996.

[27] D. Sen, B. S. Shastry, R. E. Walstedt, and R. Cava, "Quantum solitons in the sawtooth lattice," *Phys. Rev. B*, vol. 53, pp. 6401–6405, 1996.

[28] D. S. Rokhsar and S. A. Kivelson, "Superconductivity and the quantum hard-core dimer gas," *Phys. Rev. Lett.*, vol. 61, pp. 2376–2379, 1988.

[29] M. E. Fisher, "Statistical mechanics of dimers on a plane lattice," *Phys. Rev.*, vol. 124, pp. 1664–1672, 1961.

[30] M. E. Fisher and J. Stephenson, "Statistical mechanics of dimers on a plane lattice. II. Dimer correlations and monomers," *Phys. Rev.*, vol. 132, pp. 1411–1431, 1963.

[31] G. Misguich, D. Serban, and V. Pasquier, "Quantum dimer model on the kagome lattice: Solvable dimer-liquid and Ising gauge theory," *Phys. Rev. Lett.*, vol. 89, p. 137202, 2002.

[32] C. Zeng and V. Elser, "Quantum dimer calculations on the spin-1/2 kagome Heisenberg antiferromagnet," *Phys. Rev. B*, vol. 51, pp. 8318–8324, 1995.

[33] V. Elser and C. Zeng, "Kagome spin-1/2 antiferromagnets in the hyperbolic plane," *Phys. Rev. B*, vol. 48, pp. 13 647–13 653, 1993.

[34] S. R. White, unpublished.

[35] H.-C. Jiang, H. Yao, and L. Balents, "Spin liquid ground state of the spin-1/2 square J_1-J_2 Heisenberg model," *Phys. Rev. B*, vol. 86, p. 024424, 2012.

[36] E. Lieb, T. Schultz, and D. Mattis, "Two soluble models of an antiferromagnetic chain," *Ann. Phys. (N. Y.)*, vol. 16, pp. 407–466, 1961.

[37] A. Läuchli, unpublished.

[38] H.-C. Jiang and L. Balents, unpublished.

[39] E. Fradkin, "The spectrum of short-ranged resonating valence-bond theories," in *Field Theories in Condensed Matter Physics: A Workshop*, Z. Tesanović, Ed. Addison-Wesley, 1990.

[40] E. Fradkin and S. Kivelson, "Short range resonating valence bond theories and superconductivity," *Mod. Phys. Lett. B*, vol. 04, p. 225, 1990.

[41] R. Moessner and S. L. Sondhi, "Resonating valence bond phase in the triangular lattice quantum dimer model," *Phys. Rev. Lett.*, vol. 86, pp. 1881–1884, 2001.

[42] R. Moessner, S. L. Sondhi, and E. Fradkin, "Short-ranged resonating valence bond physics, quantum dimer models, and Ising gauge theories," *Phys. Rev. B*, vol. 65, p. 024504, 2001.

[43] P. Nikolic and T. Senthil, "Physics of low-energy singlet states of the kagome lattice quantum Heisenberg antiferromagnet," *Phys. Rev. B*, vol. 68, p. 214415, 2003.

[44] Y. Huh, M. Punk, and S. Sachdev, "Vison states and confinement transitions of Z_2 spin liquids on the kagome lattice," *Phys. Rev. B*, vol. 84, p. 094419, 2011.

[45] H. Ju and L. Balents, "Finite-size effects in the Z_2 spin liquid on the kagome lattice," *Phys. Rev. B*, vol. 87, p. 195109, 2013.

[46] M. Gingras, "Spin ice," in *Introduction to Frustrated Magnetism*, C. Lacroix, P. Mendels, and F. Mila, Eds. Springer, 2011.

[47] I. A. Ryzhkin, "Magnetic relaxation in rare-earth oxide pyrochlores," *J. Exp. Theor. Phys.*, vol. 101, p. 481, 2005.

[48] C. Castelnovo, R. Moessner, and S. L. Sondhi, "Magnetic monopoles in spin ice," *Nature*, vol. 451, pp. 42–45, 2007.

[49] D. J. P. Morris, D. A. Tennant, S. A. Grigera, B. Klemke, C. Castelnovo, R. Moessner, C. Czternasty, M. Meissner, K. C. Rule, J.-U. Hoffmann, K. Kiefer,

S. Gerischer, D. Slobinsky, and R. S. Perry, "Dirac strings and magnetic monopoles in the spin ice $Dy_2Ti_2O_7$," *Science*, vol. 326, p. 411, 2009.

[50] H. R. Molavian, M. J. P. Gingras, and B. Canals, "Dynamically induced frustration as a route to a quantum spin ice state in $Tb_2Ti_2O_7$ via virtual crystal field excitations and quantum many-body effects," *Phys. Rev. Lett.*, vol. 98, p. 157204, 2007.

[51] J. D. Thompson, P. A. McClarty, and M. J. P. Gingras, "Local susceptibility of the $Yb_2Ti_2O_7$: Rare-earth pyrochlore computed from a hamiltonian with anisotropic exchange," *J. Phys.: Condens. Matter*, vol. 23, p. 164219, 2011.

[52] J. D. Thompson, P. A. McClarty, H. M. Rønnow, L. P. Regnault, A. Sorge, and M. J. P. Gingras, "Rods of neutron scattering intensity in $Yb_2Ti_2O_7$: Compelling evidence for significant anisotropic exchange in a magnetic pyrochlore oxide," *Phys. Rev. Lett.*, vol. 106, p. 187202, 2011.

[53] K. A. Ross, L. Savary, B. D. Gaulin, and L. Balents, "Quantum excitations in quantum spin ice," *Phys. Rev. X*, vol. 1, p. 021002, 2011.

[54] Y. Wan and O. Tchernyshyov, "Quantum strings in quantum spin ice," *Phys. Rev. Lett.*, vol. 108, p. 247210, 2012.

[55] P. W. Anderson, "Ordering and antiferromagnetism in ferrites," *Phys. Rev.*, vol. 102, pp. 1008–1013, 1956.

[56] L. Pauling, "The structure and entropy of ice and of other crystals with some randomness of atomic arrangement," *J. Am. Chem. Soc.*, vol. 57, pp. 2680–2684, 1935.

[57] C. L. Henley, "Power-law spin correlations in pyrochlore antiferromagnets," *Phys. Rev. B*, vol. 71, p. 014424, 2005.

[58] M. J. Harris, S. T. Bramwell, D. F. McMorrow, T. Zeiske, and K. W. Godfrey, "Geometrical frustration in the ferromagnetic pyrochlore $Ho_2Ti_2O_7$," *Phys. Rev. Lett.*, vol. 79, pp. 2554–2557, 1997.

[59] T. Fennell, P. P. Deen, A. R. Wildes, K. Schmalzl, D. Prabhakaran, A. T. Boothroyd, R. J. Aldus, D. F. McMorrow, and S. T. Bramwell, "Magnetic coulomb phase in the spin ice $Ho_2Ti_2O_7$," *Science*, vol. 326, pp. 415–417, 2009.

[60] L. D. C. Jaubert, J. T. Chalker, P. C. W. Holdsworth, and R. Moessner, "Three-dimensional kasteleyn transition: Spin ice in a [100] field," *Phys. Rev. Lett.*, vol. 100, p. 067207, 2008.

[61] S. Powell and J. T. Chalker, "Classical to quantum mappings for geometrically frustrated systems: Spin-ice in a [100] field," *Phys. Rev. B*, vol. 78, p. 024422, 2008.

[62] M. Hermele, M. P. A. Fisher, and L. Balents, "Pyrochlore photons: The u(1) spin

liquid in a s=1/2 three-dimensional frustrated magnet," *Phys. Rev. B*, vol. 69, p. 064404, 2004.

[63] E. H. Lieb, "Residual entropy of square ice," *Phys. Rev.*, vol. 162, p. 162, 1967.

[64] S. H. Curnoe, "Quantum spin configurations in $Tb_2Ti_2O_7$," *Phys. Rev. B*, vol. 75, p. 212404, 2007.

[65] G. T. Barkema and M. E. J. Newman, "Monte carlo simulation of ice models," *Phys. Rev. E*, vol. 57, p. 1155, 1998.

[66] J. B. Kogut, D. K. Sinclair, R. B. Pearson, J. L. Richardson, and J. Shigemitsu, "Fluctuating string of lattice gauge theory: The heavy-quark potential, the restoration of rotational symmetry, and roughening," *Phys. Rev. D*, vol. 23, p. 2945, 1981.

[67] A. Polyakov, "Quark confinement and topology of gauge theories," *Nucl. Phys. B*, vol. 120, p. 429, 1977.

Vita

Yuan Wan received an M. Sc. in physics from Nanjing University, People's Republic of China, in 2009. He joined the physics PhD program at the Johns Hopkins University in the same year. The focus of his research is the theory of frustrated magnets.

Yuan Wan was an Owen Scholar in the Krieger School of Arts and Sciences from 2009 to 2012. He was awarded the William Gardner fellowship by the Department of Physics and Astronomy at the Johns Hopkins University in 2010, and the Graduate Fellowship by the Kavli Institute for Theoretical Physics at University of California, Santa Barbara in 2013.

Starting in August 2014, Yuan Wan will join the Perimeter Institute for Theoretical Physics, Ontario, as a postdoctoral fellow.